University of Alberta Library
0 1620 2982306 7

Digitized by the Internet Archive
in 2026 with funding from
University of Alberta Library

https://archive.org/details/0162029823067

University of Alberta

Surface Chemical Reactivity and Metal Adsorptive Properties of Natural Microbial Mats, Iron Oxides, and Infaunal Mucus Secretions

by

Stefan Victor Lalonde

A thesis submitted to the Faculty of Graduate Studies and Research
in partial fulfillment of the requirements for the degree of

Doctor of Philosophy

Department of Earth and Atmospheric Sciences

Edmonton, Alberta
Spring 2011

UNIVERSITY LIBRARY

Abstract

Chemical adsorption reactions occurring at the solid-water interface play an important role in mineral nucleation, elemental mobility, and the geochemistry of natural waters in general. Chemical equilibrium surface complexation modeling (SCM) of adsorption reactions has been widely applied in recent years to better understand these roles. However, many important sorbents remain unevaluated for surface chemical reactivity, or have only been evaluated under artificial conditions such in laboratory microbial culture. This thesis expands current knowledge regarding the elemental adsorptive properties of organic matter (OM) and iron oxide sorbents in three independent but complimentary studies. In chapters 2 and 3, concentrated bacterial and algal biomass harvested directly from natural hydrothermal springs provide the first available data for the abundance and nature of microbial reactive functional groups in natural settings. Both studies demonstrate that natural microbial biomass is generally comparable with laboratory culture in terms of in overall surface reactivity. Metal desorption experiments and surface complexation modeling provide insight into *in-situ* adsorption reactions occurring from hydrothermal spring waters onto microbial mat and iron oxide substrates. Significant variation in adsorbed metal loads argues against a universal surface complexation model for bacteria, and points to a strong role for silica in natural iron oxide surface chemistry. Complimentary studies detailed in Appendices 1 and 2 further examine the relation of this finding to the iron oxide rock record.

Bioturbating animals may have a profound effect on the sediment-water interface. Mucus is secreted by a variety of infaunal animals but its geochemical properties are poorly understood. Chapter 4 details experiments where Terebellid polychaete burrow mucus was characterized by FTIR spectroscopy, acid-base titrations and cadmium adsorption experiments to understand the reactive site density and aqueous metal affinity of natural animal mucus. The data reveal that Terebellid mucus shows strong compositional similarity with mucus from distantly related organisms, and possesses proton-reactive surface site densities and cadmium stability constants that are relatively high, most likely stemming from mucin's extended conformation and abundance of chalcophilic thiol organic functional groups. These results provide insight into the nature and geochemical reactivity of animal mucus as it pertains to elemental mobility across the sediment-water interface.

Table of Contents

Chapter 1: Introduction **1**

1.1 Geochemically-reactive surfaces in nature 1

1.2 Equilibrium modeling of surface chemical reactions 3

1.3 Surface complexation modeling of the microbial surface 6

1.4 Natural iron oxides and implications for ocean chemistry during the deposition of Precambrian iron formations 8

1.5 References 10

Chapter 2: Surface chemical reactivity and metal adsorptive properties of natural cyanobacterial mats from an alkaline hydrothermal spring, Yellowstone National Park **16**

2.1 Introduction 16

2.2 Methods 18

2.2.1 Site description and sample collection 18

2.2.2 Sample Preparation and Acid-Base Titration 18

2.2.3 Discrete ligand modeling 20

2.2.4 Light Microscopy 21

2.3 Results 22

2.3.1 Site and sample descriptions 22

2.3.2 Acid-base Titrations 24

2.3.3 Discrete functional group distributions 24

2.3.3.1 Acid-washed samples 25

2.3.3.2 Electrolyte-washed samples 26

2.3.4 Acid-leachable metal concentrations 27

2.4 Discussion 29

2.4.1 Identification of mat ligands 29

2.4.2 Balance between available ligands and sequestered metals 31

2.4.3 Trends in metal sequestration 33
2.5 Conclusion 36
2.6 References 51

Chapter 3: Chemical Reactivity of Microbe and Mineral Surfaces in Hydrous Ferric Oxide Depositing Hydrothermal Springs **55**

3.1 Introduction 55
3.2 Methods 16
3.2.1 Aqueous Sample Collection 61
3.2.2 Solid Sample Collection 61
3.2.3 Acid-base titration 62
3.2.4 Discrete Site Modelling 63
3.3 Results 66
3.3.1 Stream Geochemistry 66
3.3.2 Bulk composition of HFOs 66
3.3.3 Surface elemental concentrations 67
3.3.4 Substrate surface charge 68
3.3.5 Discrete Site Modeling 69
3.4 Discussion 72
3.4.1 HFO surface reactivity 72
3.4.2 Microbial surface reactivity 73
3.4.3 Surface complexation modeling 75
3.5 Conclusion 81
3.6 References 94

Chapter 4: Investigating the Geochemical Impact of Burrowing Animals: Proton and Cadmium Adsorption onto the Mucus Lining of Terebellid Polychaete Worms **100**

4.1 Introduction 100
4.2 Methods 103
4.2.1 Mucus Procurement 103

4.2.2 Mucus compositional analysis 104
4.2.3 Acid-base titration and Cd adsorption 105
4.3 Results and Discussion 107
4.3.1 Composition of Mucous Lining 107
4.3.2 Proton Adsorption and Discrete Ligand Modeling 108
4.3.3 Cadmium adsorption 111
4.4 Conclusion 116
4.5 References 128

Chapter 5: Summary 134

5.1 Surface chemical reactivity of natural microbial biomass 134
5.2 Surface chemical reactivity of Terebellid worm mucus 138
5.3 Natural iron oxides and implications for ocean chemistry during the deposition of Precambrian iron formations 141
5.4 References 143

Appendix 1: Was There Really an Archean Phosphate Crisis? 146

Brevia 146
Methods 149
References 153

Appendix 2: Oceanic Nickel Depletion and a Methanogen Famine before the Great Oxidation Event 154

Preamble 154
Letter 155
Methods 161
Supplementary material 175

List of Tables

2-1	Modeled functional group concentrations and acidity constants for cyanobacterial mat samples from Mound spring	49
2-2	Geochemical data from Mound spring stream waters and sample leach experiments	50
3-1	Geochemical data for Norris Geyser basin stream waters	91
3-2	Geochemical data from sample leach experiments	92
3-3	Modeled functional group concentrations and acidity constants for samples from Norris Geyser basin	93
4-1	Terebellid mucus compositional data	125
4-2	Modeled mucus functional group concentrations and acidity constants	126
4-3	Surface complexation modeling of Cd adsorption by mucus	127

List of Figures

1-1	HFO surface site speciation as a function of pH	14
1-2	Charge excess, functional group pK_a distribution, and surface site speciation in a simulated microbial titration	15
2-1	Overview of sampling locations in Sentinel Meadows, YNP	38
2-2	LM images of cyanobacterial streamers and spires	40
2-3	LM images of cyanobacterial mats	41
2-4	LM images of mat mineral grains	42
2-5	Excess charge data and model fits from acid-base titration	43
2-6	Modeled functional group distributions for acid-washed samples	44
2-7	Modeled functional group distributions for rinsed samples	45
2-8	Elemental distribution coefficients between stream and biomass	46
2-9	Correlation between total metal and ligand concentrations	47
2-10	Metal solubility and organic complexation controls over distribution coefficients	48
3-1	Overview of Sampling locations in Norris Geyser Basin, YNP	82
3-2	SEM images of mat microorganisms	83
3-3	Elemental concentration factors for HFO substrates	84
3-4	Elemental concentration factors for substrates in Beowulf spring	85
3-5	Excess charge data and model fits from acid-base titration	86
3-6	Modeled functional group distributions for HFO samples	87
3-7	Modeled functional group distributions for mat samples	88
3-8	Titration reversibility	89
3-9	Modeled and measured surface ion concentrations	90
4-1	Photographs of worm incubation and mucus procurement	117
4-2	Terebellid mucus FTIR spectra	118
4-3	Titration excess charge and model fits	116
4-4	Comparison of mucus total ligand density with other sorbents	121
4-5	Aqueous Cd speciation for experimental conditions	122

4-6 Cadmium adsorption data, surface complexation modeling and speciation 123

Appendix 1 Figure 1
Phosphate and silica co-precipitation with ferrihydrite 151

Appendix 2 Figure 1
Ni/Fe molar ratios in IF through time 165

Appendix 2 Figure 2
Ni partitioning during iron-silica co-precipitation 166

Appendix 2 Figure 3
Extrapolation of dissolved marine Ni through time 167

CHAPTER 1

Introduction

1.1 Geochemically-reactive surfaces in nature

The solid-water interface serves as the locus for many geologically important chemical reactions. Reactions involving hydrolysis, complexation, precipitation, dissolution, polymerization, and oxidation-reduction may all be profoundly affected in terms of the reaction kinetics and free energy change when localized at the solid-water interface. Chemically adsorbent materials play critical roles in the elemental composition of natural soils and waters, influencing processes ranging from chemical weathering and corrosion to the development of geochemical stratification in soils and natural waters.

Naturally important sorbents typically possess large surface areas, and as a consequence of the inverse relationship between surface area and volume, they are generally small. This is exemplified by hydrous ferric oxide (HFO), which under natural conditions readily forms nanoscale particles possessing specific surface areas upwards of 600 m^2 per gram (Roden et al., 2003); this is broadly equivalent to the surface area of a baseball infield. It is believed that iron oxides provide one of the most important reactive mineral surfaces found in nature (Cornell and Schwertmann, 2003), and accordingly, the surface chemistry of iron oxides has long been studied in relation to the adsorption of contaminants in natural waters. Indeed, Dzombak and Morel (1990) focused solely on iron oxides in their 393-page book "Surface Complexation Modeling – Hydrous Ferric Oxide". A seminal publication and a culmination of decades of work in the field of aquatic interfacial chemistry, it detailed a coherent thermodynamic framework explicitly and successfully described adsorption reactions between physically distinct HFO surface reactive sites and dissolved anionic forms of arsenic, boron, chromium, phosphorus, molybdenum, selenium, silicon, tungsten, and vanadium, among others; adsorption of a similarly diverse set of dissolved cations was

equally treated. The surface complexation model (SCM) approach they employed uses experimentally- and/or theoretically-derived thermodynamic parameters describing chemical equilibrium reactions of surface species to account for adsorption behavior for nearly any geochemical condition, in a manner akin to aqueous chemical equilibrium modeling (see section 1.2, as well as Davies and Kent (1990) for a more thorough introduction to SCM). The surface complexation modeling approach exemplified by Dzombak and Morel (1990) is incredibly powerful, directly applicable for ion adsorption in any low-temperature system where water is stable, to all hydrous oxide minerals, and subject only to the availability of thermodynamic parameters pertinent to the surface reactions of interest.

Organic matter (OM) is also generally known as an important sorbent in natural environments. Recalcitrant organic matter degradation products (i.e., humic and fulvic acids) are naturally ubiquitous and possess high concentrations of reactive surface sites that are known to strongly complex many reactive elements in natural waters. Accordingly, significant efforts have been made to quantify their reactivity and develop predictive adsorption models within a surface complexation framework comparable with the treatment of mineral surfaces (e.g., Tipping, 1998). Owing to their ubiquity and small size, microbial cells also expose significant amounts of chemically-reactive organic surface ligands to natural waters, and in recent years have been the subject of increasing attention as their geochemical importance has become better understood (see section 1.3). Despite significant progress towards understanding the surface complexation behavior of microbial cell surfaces and other geochemically-relevant OM sorbents, critical surface complexation parameters describing OM surface reactivity, such as reactive site concentrations and acidity constants, have only been determined using laboratory analogs, or for some forms of OM, have remained entirely unexplored.

The work presented in this thesis expands current knowledge on the complexation of dissolved ions by OM in two significant ways. First, the issue of the applicability of microbial surface chemical parameters determined from

laboratory cultures towards natural microbial biomass is addressed in chapters 2 and 3, where the first surface chemical parameters describing natural microbial biomass are reported. Second, animal mucus, a novel but widely occurring form of natural OM, is evaluated in chapter 4 for comparison in terms of surface reactivity with other geochemically important OM sorbents. These studies are unified by the application of discrete-site surface complexation modeling to place quantitative constraints on proton and metal adsorption by these materials in a chemical equilibrium framework.

1.2 Equilibrium modeling of surface chemical reactions

Chemical reactions occurring at the solid-water interface can be considered analogous to the formation of soluble complexes by the fact that both can be defined by as equilibrium processes according to the law of mass action. For the an aqueous reaction aA + bB ⇔ cC + dD, the equilibrium constant K_{eq} is described by:

$$K_{eq} = \frac{[C]^c[D]^d}{[A]^a[B]^b} \qquad (1)$$

In the case of surface reactions, exposed reactive sites dominate adsorption behavior such that the bulk material may be omitted from consideration. For example, deprotonation of a surface hydroxyl group may be written as

$$>XOH \Leftrightarrow >XO^- + H^+ \qquad (2)$$

where >X represents a hydroxyl-bearing surface. Such surfaces are ubiquitous in nature, and are represented by the common hydrous oxides of elements such as iron, silicon, aluminum, titanium and manganese. Commonality in chemical behavior and coordination environment leads to the classification of surface reactive sites according to the "functional group"; for example, despite an incredible diversity of natural organic compounds, simple functional groups of hydroxyl, carboxyl, phosphoryl, amino, sulfyhydryl (thiol), and phenol constitute

the vast majority of proton-reactive surface sites on natural organic matter (see section 1.3).

Surface chemical complexation differs fundamentally from aqueous complexation by the accumulation of electrostatic charge at the solid-water interface. This arises as the result of pH-dependant surface protonation/deprotonation reactions such as equation (2). While some minerals (e.g., clays) possess permanent structural charge as the result of lattice defects, hydrous oxide minerals develop a positive surface charge at low pH as surface sites are neutralized or rendered positively charged with the surface adsorption of protons. Conversely, at high pH, progressive deprotonation reactions ultimately expose negatively charged oxygen ligands. For example, surface sites of hydrous ferric oxide (HFO) determine HFO surface charge through the following deprotonation reactions:

$$>FeOH_2^+ \leftrightarrow >FeOH + H^+ \quad pK_a = 7.29 \qquad (3)$$

$$>FeOH \leftrightarrow >FeO^- + H^+ \quad pK_a = 8.93 \qquad (4)$$

where >FeOH denotes iron hydroxyl functional groups (negative log acidity constants (pK_a) from Dzombak and Morel, 1990). At pH values below 7.29, hydroxyl surface sites (>FeOH) will protonate to form positively charged $>FeOH_2^+$, and at pH values above 8.93, deprotonate to form negatively charged $>FeO^-$. In between, the iron hydroxyl is amphoteric, capable of acting as either an acid or a base. The interdependence between HFO surface site speciation, surface charge, and pH is illustrated in Figure 1-1, where it can be seen that at pH ~8, surface sites of opposite charge are present in equal amounts; this is the point of zero charge (PZC) of HFO. At pH values below this, surfaces will have a net positive charge, and above, a net negative charge. Such pH-dependent charging behavior is readily quantified in terms of proton-reactive functional groups by acid-base titration (for example see Figure 1-2), and can even be observed directly by migration of particles in a strong electromagnetic field (e.g., Bayer and Sloyer, 1990). Equilibrium modeling of surface chemical reactions, so-called surface

complexation modeling (SCM), accounts for free energy changes associated with the movement of ions through electrostatic gradients by separating the total free energy of a reaction (ΔG°_{tot}) into an intrinsic (e.g., chemical) term (ΔG°_{int}), analogous the traditional ΔG° of reaction, and a columbic term (ΔG°_{coul}), representing free energy change owing to electrostatic effects:

$$\Delta G^\circ_{tot} = \Delta G^\circ_{int} + \Delta G^\circ_{coul} \qquad (5)$$

$$\Delta G^\circ_{coul} = \Delta Z F \Psi \qquad (6)$$

where Ψ is the surface potential in volts, F is Faraday's constant, and ΔZ is the change in surface species charge owing to the adsorption reaction. Coupling between surface potential (in volts) and free surface charges (in coulombs or moles) resulting from proton exchange is complex and many different treatments exist (e.g., constant capacitance, Guoy-Chapman, and triple layer models); it suffices here to note that the electrical capacitance of different materials conveys different rates of electrostatic charging with progressive proton exchange. For all materials at their respective PZC, the columbic term drops to zero, and this is manifested as a point of zero salt effect in adsorption experiments performed at multiple ionic strengths. While surface electrostatic effects have long been known to be important for mineral surfaces, many organic materials demonstrate adsorption behavior with little or no ionic strength dependence, indicating that the columbic term is minimal (e.g., Borrok et al., 2005). In such cases, surface complexation modeling efforts may be reduced to the intrinsic term only and become directly analogous to equilibrium models of aqueous complexation. Such a non-electrostatic approach to modeling adsorption to heterogenous organic matter has proven highly successful (e.g., Borrok et al., 2005) and is applied throughout this thesis. However, it should be noted that the relative applicability of electrostatic and non-electrostatic surface complexation models to organic matter remains an area of active research.

1.3 Surface complexation modeling of the microbial surface

Adsorption reactions occurring at the microbial cell surface began receiving significant attention after initial reports by Beveridge and co-workers, who identified organic compounds that might be responsible for the strong metal complexation behaviour they observed for microbial cell walls (e.g., Beveridge and Murray, 1980; Beveridge and Fyfe, 1985). Early studies demonstrated pH-dependent surface charging behavior that was akin to mineral surfaces (Bayer and Sloyer, 1990; Plette et al., 1995). A significant milestone was achieved when Fein et al. (1997) first treated organic functional groups on the microbial cell surface as discrete reactive sites within a formal surface complexation model. Discrete surface functional group acidity constants and concentrations (e.g., site density) on the microbial surface became critical parameters, however the extent to which these varied across the microbial biosphere was wholly unknown.

Acid-base titration can be used to place quantitative constraints on these parameters, and at present, a diverse collection of microbial biomass samples have been examined by acid-base titration in this context (Daughney et al., 2001; Phoenix et al., 2002; Ngwenya et al., 2003; Borrok et al., 2004; Fein et al., 2004; Haas, 2004; Borrok and Fein, 2005, among others). Three significant results have emerged that appear to apply generally across the microbial biosphere: (1) only a small number of different organic functional group types (specifically, carboxyl, phosphoryl, amino, thiol, and hydroxyl) account for most proton and metal adsorption reactions, (2) they appear limited in cumulative surface concentration to within one order of magnitude of 1 mmol per dry gram of microbial biomass, and (3) experimental metal adsorption data for microbial biomass is well described by surface complexation models invoking only these sites (e.g., Fowle and Fein, 1999). Spectroscopic data (e.g., Boyanov et al., 2003; Jiang et al., 2004) and the existence of strong linear free energy relationships in metal stability constants between the above surface functional groups indicated for microbial biomass and their aqueous analogs (Fein et al., 2001) provide strong support for their role as the primary reactive ligands at the microbial surface.

Despite recent advancements, the issue of variability in critical surface parameters across the microbial biosphere remains debated. It has been advocated on the basis of cadmium adsorption isotherms that microbes display "universal" adsorption behavior (Yee et al., 2001; Borrok et al., 2004), where a single set of surface chemical parameters might be employed for modeling all microbial metal adsorption reactions. This is in apparent contradiction with independent work indicating a statistically significant role for laboratory culture growth conditions on microbial surface functional group concentrations, acidity constants, and cadmium stability constants (Daughney et al., 2001; Haas, 2004; Lalonde et al., 2008a; Lalonde et al., 2008b). Crucially, the possibility of such sensitivity begs the question of the applicability of surface chemical parameters derived from laboratory microbial batch cultures to microbes as they occur naturally. In chapters 2 and 3, the issue of variability in surface chemical parameters across the microbial biosphere, and the applicability of culture-derived parameters to natural microbial biomass, is addressed directly in the first available reports of surface chemical parameters characterizing natural microbial populations.

Microbial biomass constitutes only one category of naturally-abundant organic matter whose surface chemical reactivity is poorly constrained. A enormous diversity of animals produce mucus secretions that serve to enhance motility, prevent desiccation, and in the case of bioturbating animals, to physically support burrow walls. However, the surface chemical reactivity of animal mucus has remained wholly unexplored to date. As described in chapter 4, Terebellid worms were incubated for the collection and examination of the mucus-lined tubes it produces. Considering that Terebellid worms have been reported to reach population densities of over 7,000 individuals per m^2 (Ropert and Dauvin, 2000; Callaway, 2006), ion adsorption by their mucus, and that of other mucus-secreting infauna in general, may play an important role in elemental mobility across the sediment-water interface. The data presented in Chapter 4 support this assertion, indicating that natural animal mucus possesses organic surface functional groups that are unusually abundant and metal reactive relative to natural microbial biomass and other organic matter.

1.4 Natural iron oxides and implications for ocean chemistry during the deposition of Precambrian iron formations

Iron is Earth's most abundant element, and fifth most abundant in the Earth's crust. As a transition element, iron participates in a variety of oxidation and reduction (redox) reactions, and in sedimentary deposits it is found predominately in the form of oxide minerals such as hematite (Fe_2O_3) and magnetite (Fe_3O_4). These crystalline iron oxides are typically the diagenetic products of amorphous mineral precursors; Fe(II) and Fe(III) react with water to form iron hydroxide ions and readily precipitate as hydrous iron oxide minerals. Importantly, hydrous iron oxide minerals form chemical sediments and cements under a variety of aqueous conditions and geological settings, ranging from rapid precipitation upon mixing of Fe-rich hydrothermal fluids with marine and fresh waters, to the slow formation of concretions and cements at redox boundaries in soil and sediment. The ubiquity of iron oxides in near-surface environments, and the fact that their composition is intimately linked to the chemistry of the waters from which they precipitate, make them especially promising as records of the geochemical and redox history of Earth surface environments.

In chapter 3, natural hydrous iron oxides from three hydrothermal springs in the Norris Geyser basin (YNP) are evaluated alongside microbial substrates for surface chemical reactivity in terms of surface functional group concentrations and acidity constants. Drawing from the large body of available literature and equilibrium surface stability constants describing ion adsorption to the hydrous iron oxide surface, surface chemical controls over trace element partitioning between spring waters and natural iron oxides are evaluated through a surface complexation model. A strong role for the presence of dissolved silica in the surface functional group composition and reactivity of hydrous iron oxides is indicated; this result is not surprising considering the strong affinity that exists between dissolved silica and the hydrous iron oxide surface (e.g., Davies et al., 2002). This result is highly novel, however, in that it represents the first natural modern example where such co-precipitation has been documented. Furthermore, these findings have significant implications for the use of sedimentary iron oxide

minerals as trace element paleo-proxies for ancient oceans where silica was abundant, an issue discussed at length in Chapter 5. Direct applications of these findings to the ancient sedimentary iron oxide record are detailed in two supplemental but complimentary studies included as Appendix 1 and 2, where the Precambrian iron formations are explored as proxies for the history of dissolved marine phosphorus and nickel in deep geological time.

1.5 References

Bayer ME and Sloyer Jr. JL (1990) The electrophoretic mobility of gram-negative and gram-positive bacteria: an electrokinetic analysis. *Journal of General Microbiology* 136, 867-874.

Beveridge TJ and Fyfe WS (1985) Metal fixation by bacterial cell walls. *Canadian Journal of Earth Science* 22, 1893-1898.

Beveridge TJ and Murray RG (1980) Sites of metal deposition in the cell wall of *Bacillus subtilis*. *Journal of Bacteriology* 141, 876-887.

Borrok D and Fein JB (2005) The impact of ionic strength on the adsorption of protons, Pb, Cd, and Sr onto the surfaces of Gram negative bacteria: testing non-electrostatic, diffuse, and triple-layer models. *Journal of Colloid and Interface Science* 286, 110-126.

Borrok D, Kulpa CF, and Fein JB (2004) Proton and Cd adsorption onto natural bacterial consortia: testing universal sorption behavior. *Geochimica et Cosmochimica Acta* 68, 3231-3238.

Boyanov MI, Kelly SD, Kemner KM, Bunker BA, Fein JB, and Fowle DA (2003) Adsorption of cadmium to *B. subtilis* bacterial cell walls - a pH-dependent XAFS spectroscopy study. *Geochimica et Cosmochimica Acta* 67, 3299-3311.

Callaway R. (2006) Tube worms promote community change. Marine Ecology Progress Series, v. 308, p. 49-60.

Cornell RM and Schwertmann U (2003) *The Iron Oxides: Structure, Properties, Reactions, Occurrences and Uses*. Wiley-VCH, Weinheim, Germany.

Daughney CJ, Fowle DA, and Fortin DF (2001) The effect of growth phase on proton and metal adsorption by *Bacillus subtilis*. *Geochimica et Cosmochimica Acta* 65,1025-1035.

Davies, CC, Chen H-W, and Edwards, M (2002) Modeling silica sorption to iron hydroxide. *Environmental Science and Technology* 36, 582-587.

Davis JA and Kent DB (1990) Surface complexation modeling in aqueous geochemistry. In *Reviews in Mineralogy Vol 23: Interface Geochemistry*. Hochella, M.F. and White, A.F. (eds). Washington, DC, USA: Mineralogical Society of America, pp. 177-248.

Fein JB, Daughney CJ, Yee N, and Davis TA (1997) A chemical equilibrium model for metal adsorption onto bacterial surfaces. *Geochimica et Cosmochimica Acta* 61, 3319-3328.

Fein JB, Martin AM, and Wightman PG (2001) Metal adsorption onto bacterial surfaces: Development of a predictive approach. *Geochimica et Cosmochimica Acta*, 65, 4267-4273.

Fein JB, Boily JF, and Yee, N (2004) Potentiometric titrations of *Bacillus subtilis* cells to low pH and a comparison of modeling approaches. *Geochimica et Cosmochimica Acta* 69, 1123-1132.

Haas, JR (2004) Effects of cultivation conditions on acid-base titration properties of *Shewanella putrefaciens*. *Chemical Geology* 209, 67-81.

Jiang W, Saxena A, Song B, Ward BB, Beveridge TJ, and Myneni SCB (2004) Elucidation of functional groups on Gram-positive and Gram-negative bacterial surfaces using infrared spectroscopy. *Langmuir* 20, 11433-11442.

Konhauser KO (2007) Introduction to Geomicrobiology. Oxford, UK: Blackwell publishing.

Lalonde SV, Smith DS, Owttrim GW, and Konhauser KO (2008a) Acid-base properties of cyanobacterial surfaces I: influences of growth phase and nitrogen metabolism on cell surface reactivity. *Geochimica et Cosmochimica Acta* 72, 1257-1268.

Lalonde SV, Smith DS, Owttrim GW, and Konhauser KO. (2008b) Acid-base properties of cyanobacterial surfaces II: silica as a chemical stressor influencing cell surface reactivity. *Geochimica et Cosmochimica Acta* 722, 1269-1280.

Ngwenya BT, Sutherland IW, and Kennedy L (2003) Comparison of the acid-base behavior and metal adsorption characteristics of a gram-negative bacterium with other strains. *Applied Geochemistry* 18, 527-538.

Phoenix VR, Martinez RE, Konhauser KO and Ferris FG (2002) Characterization and implications of the cell surface reactivity of the cyanobacteria *Calothrix* sp. *Applied and Environmental Microbiology* 68, 4827-4834.

Plette CC, Van Riemsdijk WH, Benedetti MF, and Van der Wal A (1995) pH dependent charging behavior of isolated cell walls of a Gram-positive soil bacterium. *Journal of Colloid and Interface Science* 173, 354–363.

Roden, EE (2003) Fe(III) oxide reactivity toward biological versus chemical reduction. *Environmental Science and Technology* **37**, 1319-1324.

Ropert, M. and Dauvin, J.C., 2000. Renewal and accumulation of a Lanice conchilega (Pallas) population in the baie des Veys, western Bay of Seine. Oceanologica Acta, v. 23, p. 529-546.

Tipping E (1998) Humic Ion-binding Model VI: An improved description of the interactions of protons and metal ions with humic substances. *Aquatic Geochemistry* 4, 3-48.

Yee N and Fein JB (2001) Cd adsorption onto bacterial surfaces: a universal adsorption edge? *Geochimica et Cosmochimica Acta* 65, 2037–2042.

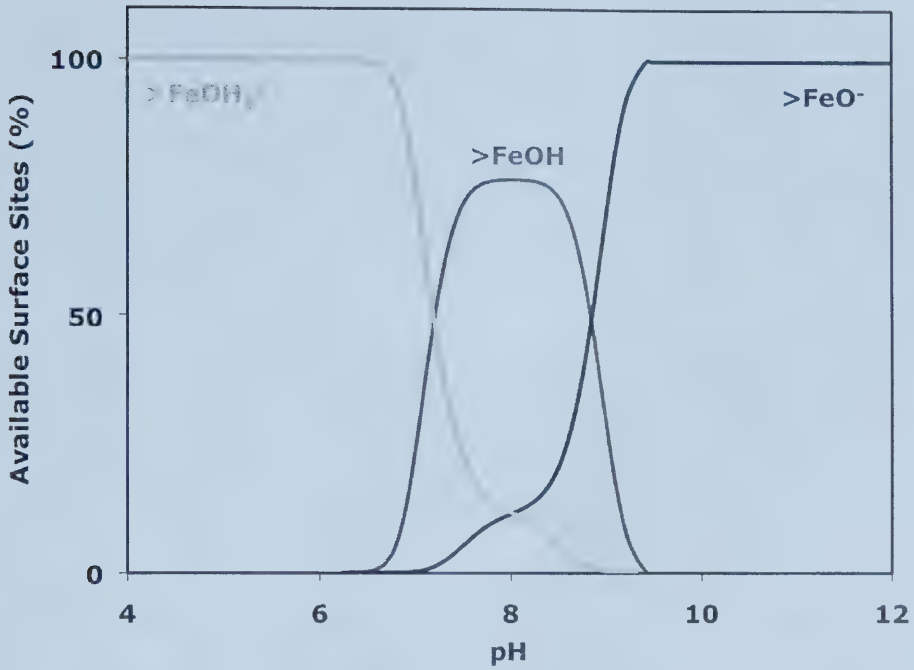

Figure 1-1. HFO surface site speciation as a function of pH. Computed using surface acidity constants from Dzombak and Morel (1990).

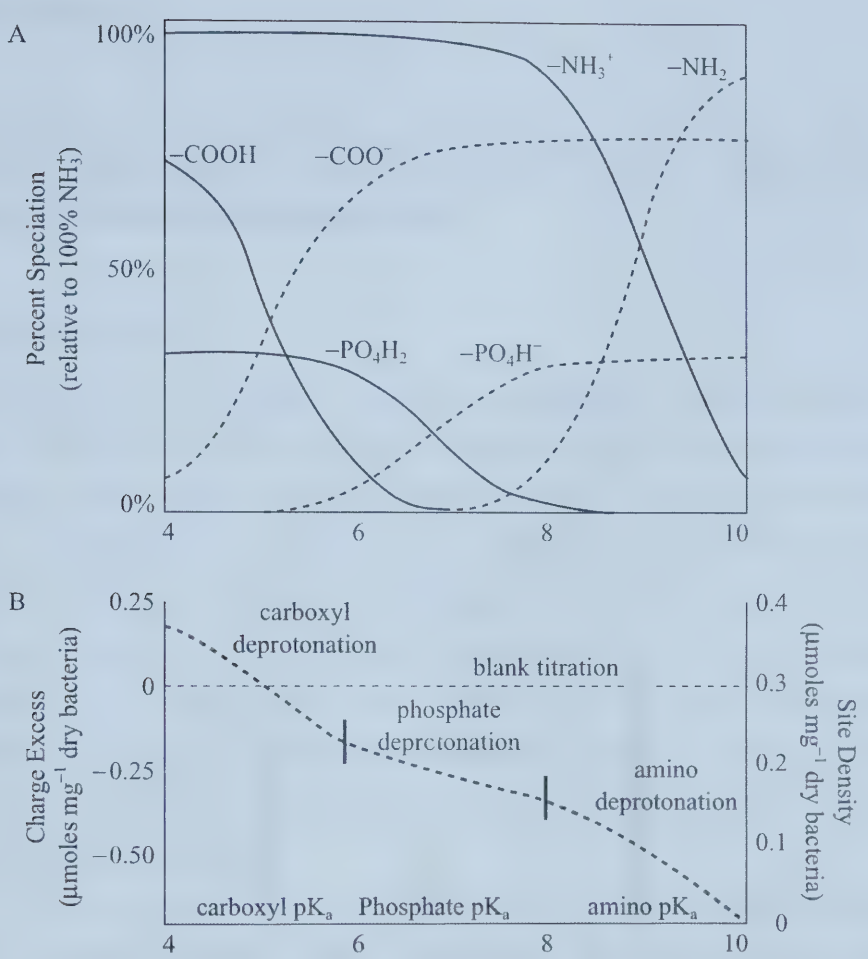

Figure 1-2. (A) Modeled surface functional group speciation and (B) distribution of functional group concentrations in acidity constant space (grey bars, with pK_a = - log K_a) for simulated titration data of microbial surface charge excess (curved dashed line in B). Labeled directly on (B) are pH ranges for near complete (95%) proton exchange by surface functional groups; note that acidity constants expressed as pK_a correspond to the pH value where a given functional group is present equally in protonated and deprotonated forms. X-axis represents pH in (A) and both pH (for charge excess) and pK_a (for site density) in (B). Adapted from Konhauser (2007).

CHAPTER 2

Surface chemical reactivity and metal adsorptive properties of natural cyanobacterial mats from an alkaline hydrothermal spring, Yellowstone National Park[1]

2.1 Introduction

Microbes are found in nearly every aqueous environment on Earth, where their highly reactive surfaces effectively adsorb metals to such an extent that they exert significant control over elemental cycling on a variety of scales (see Konhauser, 2006). The adsorption of metals by microbial biomass has been well studied in a laboratory context, and predictive surface complexation models can now accurately account for microbial sorptive phenomena under a wide range of physicochemical conditions (e.g., Fowle and Fein, 1999; Borrok and Fein, 2005). However, the application of surface complexation modeling (SCM) to natural microbial assemblages, in order to better understand their propensity to sequester metals, is complicated by several factors.

First, the determination of microbial surface chemical parameters, such as discrete surface functional group concentrations and their respective acidity constants, is required to enable SCM, yet is difficult to achieve for environmental samples. There exists no practical protocol for the culture-independent isolation of microbial biomass from most water-rock and soil systems, and indeed, surface chemical parameters have yet to be reported for natural microbial biomass. Second, mats contain a variety of microorganisms that are in different growth stages, and they produce extracellular organic materials (e.g., capsules, sheaths, S-layers) that each have their own unique chemical compositions. Third, the ability to identify and quantify metals adsorbed to microbial surfaces may be complicated by the presence of a variety of metal-bearing detrital and authigenic mineral phases that are inseparable from the microbial biomass. For instance, microbes that

[1]A version of this chapter has been published. Lalonde SV, Amskold L, Warren LA, and Konhauser KO. *Chemical Geology* **243**, 36-52 (2007).

assemble as biofilm communities in the form of laminated mats and other macroscopic structures have been observed to trap detrital material and precipitate authigenic minerals to the point where they become fully mineralized (e.g., Konhauser et al., 1999). The extent to which organic surface adsorption reactions drive metal sequestration in such complex natural systems is unknown.

In order to better understand microbial metal sequestration processes as they occur in a natural context, we evaluated surface chemical parameters and acid-leachable metal contents of cyanobacterial mats collected from an alkaline hydrothermal spring system in Yellowstone National Park. Samples representing diverse mat morphologies (streamers, vertical spires, horizontally laminated mats) were collected from the hydrothermal system within a very small spatial area (<2.5 m^2) and evaluated for diversity in their respective surface chemical properties and ability to sequester metals. Although we selected cyanobacterial mats that appeared to be wholly unmineralized, light microscopy revealed that all samples contained some mineral phases. Potentiometric titrations were performed on samples in two ways: (1) after washing in titration electrolyte that was approximately at spring pH and ionic strength, in order to best approximate the acid-base behavior of samples as they existed in-situ, and (2) after acid-washing, in order to remove minerals to the greatest possible extent, and thus reveal the inherent surface chemical properties of the organic components. This preliminary work is intended to serve as a starting point for better understanding the relative importance of the diverse chemical and physical processes that lead to metal sequestration in natural microbial assemblages.

2.2 Methods

2.2.1 Site description and sample collection

Water and microbial mat samples were collected in July 2005 from a ~2.5 m^2 area approximately 8 m downstream from the vent of Mound Spring, an alkaline geothermal feature located in the Sentinel Meadows area of lower Geyser Basin, Yellowstone National Park (Figure 2-1A). Spring temperature and pH were measured at the location of mat sampling using a Fisher digital thermometer, Beckman pH meter, and an Orion Ross electrode that was calibrated with commercial buffers heated to spring temperature and selected to bracket stream pH as closely as possible (i.e., buffers of pH 7 and 10). Source waters were collected in sterile 25 ml syringes, filtered through 0.45 mm in-line nylon syringe filters, acidified on-site by TraceMetal grade HNO_3, and cold-stored until analysis for dissolved and colloidal metals (described below). Additional spring water samples were collected for analysis by ion chromatography, but were not acidified. Total alkalinity was determined on-site by titrations with phenolphthalein and bromcresol green indicators, modified for the addition of reagents directly into a syringe containing the sample. Samples of microbial mat (0.55 - 3.37 g wet weight) were collected with sterile, stainless steel scalpels, placed in sterile 50 ml conical polypropylene centrifuge tubes, stored in spring water and ice-cooled during transport to the University of Alberta. All samples were stored in the dark at 4° C until examination, and all titration and acid-wash experiments were completed within 4 days of sampling.

2.2.2 Sample Preparation and Acid-Base Titration

All glassware and plasticware were acid-washed in ~30% v/v concentrated HCl for at least 2 h and soaked in deionized water for 12 h prior to use. Microbial mat samples were divided by weight into two groups for separate preparation and titration. One half of sample material was prepared by four alternating rinse (10 sec agitation and 10 minute soak) and harvest (centrifugation for 10 min at 10,000 g) cycles, using for each rinse ~35 ml 0.01 M KNO_3 titration electrolyte that had been adjusted to spring pH (9.2) with 0.01 M NaOH in order to minimize the

chemical disturbance of mat samples. These samples, prepared in and titrated from electrolyte adjusted to spring pH and ionic strength, are intended to best reflect the acid-base properties of the mats as they were found in-situ (i.e., retaining surface complexes and accessory minerals), and are, thus, referred to herein as "electrolyte-washed samples". The second half was similarly prepared, however the 0.01 M KNO_3 titration electrolyte was first adjusted to pH 3 with TraceMetal HNO_3 in order to serve as an acid-wash, replacing surface complexed cations with protons, and dissolving any solid phase calcite. This acid-wash procedure is intended to reveal the proton-binding behavior of the organic components comprising the biomass surface in a manner analogous to previous bacterial acid-base titrations (e.g., Fein et al., 2005 and references therein), and, thus, these samples are herein referred to as "acid-washed". The rinsing solutions, 0.45 μm filtered final titration suspensions, and samples of stream water were subsequently analyzed for selected aqueous species (Al, As, Ba, Be, Ca, Cs, Fe, Ge, Li, Mg, Mn, Ni, Rb, Sb, Sr, Ti, Zn) using a Quadrupole ICP-MS (Perkin Elmer Elan 6000, University of Alberta). Method detection limits were below 5 ppb for all elements, with relative standard deviations of less than 1.5% based on repeat standard analyses. Ion chromatography (Dionex 600) was performed on spring water samples in the Natural Resources Analytical Laboratory, University of Alberta, where detection limits were below 0.05 mM for the elements reported here (Cl^-, F^-, and SO_4^-).

For each titration, prepared sample (0.01 to 0.05 g dry weight) was suspended in ~50 ml of fresh titration electrolyte in a 125 ml titration flask, and fitted with a Ross-type pH electrode (Mandel Scientific, Guelph, Ontario), thermocouple, magnetic stir bar, titrant dispenser, and N_2 purge line. Titrations were performed alkalimetrically to pH 11 with 0.01 M NaOH (Fisher Certified 0.01 M NaOH solution) and acidimetrically to pH 3 with 0.01 M HNO_3 prepared from TraceMetal grade HNO_3 and standardized against 0.01 M NaOH. A QC-Titrate autotitrator (Mandel Scientific) interfaced to a personal computer was set to variably dispense titrant for increments of 0.1 pH units with electrode stability criteria of <0.5 mV/sec between additions. Equilibration time between additions

averaged about 40 seconds, and each titration was completed in approximately 60 minutes. Suspensions were purged with N_2 gas for 30 min prior to, and throughout, the titrations. Electrode calibrations using commercial buffers of pH 3.0, 4.0, 7.0, 10.0, and 12.0 were performed between every set of titration replicates (3-5) representing a single sample, and all pH measurements were automatically temperature-corrected. After the titrations, samples were filtered through pre-weighed 0.45 μm glass-fiber filters (GF/C #42, Whatman Inc, Florham park, NJ) and weighed after 7 days of air-drying. It should be noted that some cells may have lysed during storage, preparation, and titration, and that the heterogeneous nature of the mat biomass made it difficult to determine by light microscopy whether lysis occurred. As a proxy for cell integrity, pigment autofluorescence was examined for selected samples immediately pre- and post-titration, and no change in the frequency or intensity of cell autofluorescence was observed.

2.2.3 Discrete ligand modeling

Discrete ligand concentrations were fit to the titration data using a non-electrostatic linear-programming pK_a spectrum approach described in detail by Smith and Kramer (1999) and previously applied in a variety of potentiometric titration studies of natural organic matter and microbial biomass (Brassard et al., 1990; Smith et al., 1999; Cox et al., 1999; Martinez and Ferris, 2001; Martinez et al., 2002; Phoenix et al., 2002; Fein et al., 2005). Fitting was performed using the software package Matlab (Mathworks, Natick, MA) with computer code kindly provided by D. Scott Smith (Wilfred Laurier University). Replicate blank titrations indicated negligible experimental error in system charge balance between pH ~3.5 and pH~10.3, and data in the 4 to 10 pH range was used for modeling of ligand concentrations over a pK_a range of 3 to 11 in 0.2 pH unit increments. Excess in the charge balance of the system results from the speciation of surface-associated proton-exchanging ligands and the influence of any proton-exchanging ligands in solution. Although the latter is generally assumed to be limited for titrations of vigorously washed biomass grown under laboratory conditions, this is likely not the case for the environmental samples titrated in this experiment (discussed

below). Charge arising by proton-exchange with ligands is related to charge arising during titration by the following charge balance:

$$\sum_{j=1}^{n}[L_j^-] - [ANC] = C_{b_i} - C_{a_i} + [H^+]_i - [OH^-]_i \qquad (1)$$

where, for the i^{th} addition of titrant, C_b and C_a are the concentrations of base and acid, respectively, $[H^+]$ and $[OH^-]$ are measured by the pH electrode, $[L_j^-]$ is the concentration of deprotonated ligands for the j^{th} monoprotic ligand of n possible pK_a values set by the pK_a spectrum, and the acid neutralizing capacity (ANC) functions as a constant offset in charge excess. The ligand concentrations and ANC that provide the best fit to the measured charge excess (right hand side of equation (1)) is determined iteratively by minimizing the absolute error between measured and fitted charge excess (left hand side of equation (1)). The number of distinct-pK_a ligands that are required to describe the data is minimized as the linear-programming approach emphasizes zero as a possible solution. For each sample, between 3 and 5 replicate titrations were performed, and each titration was modeled independently.

2.2.4 Light Microscopy

Small amounts of wet, refrigerated sample were dissected by sterile stainless steel scalpel, fixed to glass slides with several drops of low-fluorescence water-based fixative, air-dried for 15 min, and immediately examined. Photomicrographs were obtained using a Quorum Technologies 16 bit color QICAM and Zeiss Axioskop mot 2 microscope operating in dark-field, differential interference contrast (DIC) bright-field, and phase contrast modes. Fluorescence images employed an excitation range of 530-585 nm. Samples were refrigerated before and after preparation, and all microscopy was performed within 7 days of sampling.

2.3 Results

2.3.1 Site and sample descriptions

At the time of collection in July 2005, Mound Spring had a source water temperature of 49°C, declining to 46°C over the ~8 m separating the source and 2.5 m^2 sampling area (Fig. 2-1B), and a pH of 9.2 at both source and sampling area. Four distinct cyanobacterial mat structures surrounding a pooled section of stream were investigated (Fig. 2-1C): submerged, "vertical spires" of biomass occupying calm waters of the pool (Fig. 2-1D), "streamers" found under flowing water at a pool outlet (Fig. 2-1E), and thick laminated structures forming on the pool walls, designated herein as "yellow mats" (Fig. 2-1E) and "white mats" (Fig. 2-1C). For both laminated mat samples, the surface was removed to a depth of ~5 mm for separate analysis (Fig. 2-1F).

Light microscopy showed that the vertical spires were dominated by long (>200 mm) filamentous *Phormidium*-like cyanobacteria that showed both random (Fig. 2-2A) and aligned orientation (Fig. 2-2B). Smaller rod-shaped cells were also ubiquitous in all samples, although their numbers appeared to be much lower and varied among samples. Almost all cells autofluoresced, indicating that the majority of cells in these mat structures were phototrophic (e.g., Fig. 2-2C). In the case of the streamer samples, autofluorescence micrographs indicated that the cell population consisted largely of filamentous, photosynthetic bacteria that were found almost equally in straight and an unusual, coiled form (Fig. 2-2C). Micrographs at high magnification indicate by cell size, as well as by apparent uncoiling phenomena, that the two forms represent different possible morphologies of a single cyanobacterial filament (images not shown). All of the biomass samples were encased to some extent in a matrix of extracellular polymeric substance (EPS); the abundant EPS enclosing the streamer structures was readily apparent in dark-field micrographs (Fig. 2-2D). The upper 5 mm of both laminated mats (yellow and white) were largely comprised of EPS (Fig. 2-3A) and filamentous bacteria lacking any alignment (Fig. 2-3B). Sections lower in the laminated mats (2 – 5 cm) displayed alternating regions of more or less dense EPS (Fig. 2-3C), the former being occupied by nearly equal densities of filamentous and

rod-shaped photosynthetic bacteria, and the latter containing almost exclusively rod-shaped bacteria, not all of which displayed autofluorescence (Fig. 2-3D). These rod-shaped non-phototrophic cells were found exclusively at lower depths in the laminated mats, and were visibly motile in wet-mount slide preparations.

Collectively, the micrographs indicate that despite their spatial proximity in the stream, the four mat morphologies differ in the relative abundances of cell types, the alignment of filamentous bacteria (directional, coiled, or random), and in the nature or density of their EPS matrix. Vertical spire and streamer mat morphologies appeared to be dominated almost exclusively by photosynthetic bacteria of filamentous or rod shape, while laminated mat morphologies additionally contained non-photosynthetic, motile, rod-shaped bacteria at depth that may be heterotrophic. The consistency in cell size and cylindrical morphology of filamentous bacteria among samples suggests that similar bacteria contribute to all four mat morphologies, although it is impossible to confirm without further ecological study (that is beyond the focus of this work). This is also true for the photosynthetic bacteria of rod shape. In turn, the various mat morphologies would appear to arise largely as a function of differential EPS production and the varying relative abundances of the bacteria described above.

Interestingly, the diverse mat morphologies also differed with respect to their visible mineral content. In the upper 5 mm of the laminated mat samples, mineral grains were abundant and typically greater than 20 mm in their longest dimension (Fig. 2-4A), while in the lower sections, grains were distinctly smaller (typically less than 5 mm in longest dimension), with sizes ranging down to the limits of equipment resolution. By comparison, streamer and vertical spire structures not only possessed fewer grains, but they were also less than 5 mm in longest dimension (Fig. 2-4B). Analysis of the mineral grains under crossed-polars revealed the presence of calcite. Furthermore, acid washing for 30 minutes at pH 3 showed that a significant proportion of those grains dissolved, as would be expected from calcium carbonate dissolution. However, some mineral grains remained, suggesting either that those grains were highly crystalline, or not carbonate in composition.

2.3.2 Acid-base Titrations

In a natural mat, metals will be sequestered by a variety of submerged substrates, including the microbial biomass as well as any authigenic and detrital minerals that it hosts. To better understand the relative roles of these individual components, we have attempted to ascertain the acid-base behavior of samples containing both organic and mineral components, and the acid-base behavior of samples that we have acid-washed with the goal of removing mineral components. In order to achieve this, we have prepared the mat samples in two distinct ways. First, "electrolyte-washed" biomass was prepared by rinsing in titration electrolyte adjusted to stream pH (9.2), and then titrated down to pH 3 to approximate the excess charge behavior of the mat sample as it was found in-situ, i.e. with mineral components intact. Second, mat material was first acid-washed for 30 min in 0.001 M HNO_3 to strip off adsorbed metals, dissolve carbonate minerals, and protonate surface ligands. Samples were then similarly rinsed with titration electrolyte, and titrated from pH 3 to 11 to evaluate proton sorption by native organic surface components.

Excess charge plots of both "acid-washed" and "electrolyte-washed" mat preparations reveal that important changes in titration charging behavior are incurred by the acid-washing procedure (Fig. 2-5). Most notably, all suspensions of electrolyte-washed mat (top lines in Fig 5A-5F) exchanged more protons over the titration range than did their acid-washed counterparts. All samples also displayed an accumulation of excess charge at both extremes of the titration range (i.e., around pH 4 and 10). Although excess charge plots generated from titration data are ill-suited for quantitative comparisons between samples, they do provide a visual assessment of proton sorption over the titration range, and thus are presented here for qualitative purposes.

2.3.3 Discrete functional group distributions

The excess charge data are more readily interpreted after being fitted with a distribution of discrete functional groups, in terms of functional group

concentrations and acidity constants (henceforth presented as pK_a, the negative log of the acidity constant; Fig. 2-6). This permits the concentrations of functional groups accounting for excess charge behavior to be compared between samples or preparations. Additionally, their pK_a values can aid in the identification of reactive mat components, and the reported data as a whole can be related to past and future studies invoking a surface complexation model to explain charging behavior. Although a non-electrostatic model was employed here for the modeling of discrete functional groups, the results are likely comparable with other studies that employ electrostatic models, as surface capacitance values assumed for previous bacterial titration studies are sufficiently high (8.0 F/m^2) as to be approximately equivalent to the non-electrostatic model (see Borrok et al. (2004) and references therein). Furthermore, in a recent comparison of discrete site modeling approaches, it was determined that for the Gram-negative surface of two *Pseudomonas* species, surface electric field effects were negligible for proton adsorption, and a non-electrostatic model adequately described proton adsorption over a wide ionic strength range (0.001 to 0.6 M) (Borrok and Fein, 2005).

2.3.3.1 Acid-washed samples

The pK_a spectra of acid-washed samples, assumed here to represent proton-active components of the native (organic) mat surface, reveal both conserved chemical features and diversity between samples. Samples of the spire-type mat indicated a pK_a distribution of ligands that span the 5 to 10 range (Fig. 2-6A), while the ligand pK_a distribution of streamer samples was dominated by low to neutral pK_a values (Fig. 2-6B). The upper 5 mm of both the laminated yellow and white mats (Fig. 2-6C and 6D) showed reasonably comparable ligand densities near pK_a 6 and 9, while lower sections of the mats indicate the presence of ligands closer to pK_a 10 (Fig. 2-6E and 6F). In general, both upper and lower samples of laminated mat showed a paucity of ligands with pK_a values below 5.5, and significant cluster of ligands between $pK_a \sim 5.5\text{-}7.5$.

For purposes of comparison, ligands were grouped into 3 pK_a classes (4-6, 6-8, and 8-10) (Table 2-1). The results indicate that the different mat structures

vary with respect to total ligand concentration, as well as in the relative importance of individual ligand classes; however, the average standard error in most pair-wise comparisons of total ligand concentration was sufficiently high (55%) as to exclude appreciable confidence. Total ligand concentrations in the acid-washed preparations varied from 2.84 ± 0.41 mmol g^{-1} for the spire-type mat to 0.98 ± 0.28 mmol g^{-1} for the lower mat section, similar in range to some previously reported values obtained for acid-washed suspensions of cultured Gram-negative (0.80 – 1.77 mmol g^{-1}; Plette, et al., 1995; Sokolov et al., 2001; Phoenix et al., 2002) and Gram-positive bacteria (0.22 – 2.29 mmol g^{-1}; Fein et al., 1997; Cox et al., 1999; Yee at al., 2004; He and Tebo, 1998). However, the lack of sites with pK_a <4 for the laminated mat samples differs from cultured representatives. These sites, often designated as carboxyl by their low pK_a values, have been implicated as primary sites for the adsorption of cations by bacteria (e.g., Beveridge et al., 1980). Their absence may explained by a retention of cations throughout the acid-wash and titration procedures, rather than an actual absence of carboxylic functional groups on the biomass surface, although additional (e.g., spectroscopic) evidence is required for any further inference.

2.3.3.2 Electrolyte-washed samples

The most significant observation of this study is that the electrolyte-washed samples contain significantly higher ligand concentrations than the acid-washed samples, with a single ligand typically dominating the pK_a spectra around 7 (Fig. 2-7, Table 2-1). In some instances, ligands with pK_a values near 4 and/or 10 were present, however they contributed no more than 48% of ligands for any electrolyte-washed sample, and on average constituted only 23% of the total ligands. The influence of an abundant ligand with pK_a ~7 is evident in the plots of excess charge, where protons are strongly consumed in the pH 6-8 range (recall Fig. 2-5).

Unlike the acid-washed samples, some of the electrolyte-washed samples are statistically different in terms of total ligand concentration (Table 2-1). Total ligand concentrations were lowest for the spires and streamers, but higher for the upper laminated mat sections, and highest for the bottom laminated mat sections.

2.3.4 Acid-leachable metal concentrations

Metal partitioning between the cyanobacterial mats and the spring waters was evaluated in terms of acid-leachable metal concentrations, which were obtained by analyzing the supernatant of each acid-wash solution for dissolved metals, and then normalizing the metal concentrations to the dry weight of acid-washed biomass. It should be noted that the metal concentrations reported here depend, to some degree, on the conditions of the acid-washing process and the presence of inorganic mat components; it is possible that the acid-wash procedure employed here failed to desorb some surface-complexed metals, and at the same time, released other metals by the dissolution of mineral components in the mat.

The concentrations of acid-leachable metals, in terms of mmol/Kg, are tabulated in Table 2-1. The ability of the mats to concentrate individual metals from the spring water may be better assessed by comparing the concentration of metals that were desorbed from the mats by acid-washing with their respective concentration in spring waters using the distribution coefficient, K_d (Fig. 2-8):

$$K_d = \frac{[\text{mat}]\ (\mu\text{mol Kg}^{-1})}{[\text{spring}]\ (\mu\text{mol L}^{-1})} \qquad (2)$$

In the log K_d plot presented in Figure 2-8, the metals are ordered by increasing aqueous concentration in spring water, and a range of distribution coefficients are apparent. Lower and upper values indicate that the concentration of metals leached from the mat ranged from 0.36 (Cs, Al) to almost 21 000 times higher (Mg) than the overlying water concentration. Distribution coefficients generally increased with decreasing spring water concentration, such that elements found at very low aqueous concentrations showed greater partitioning to the mats than did those elements found in the greatest aqueous concentration, although important exceptions are apparent (Ca, Zn). Another interesting observation is the degree of variation in elemental partitioning among samples. Some elements, such as Li, Ca, Ge, Sb, and Ti, were concentrated to similar extents by all mat samples, while others, such as Al, Rb, Cs, Be, Fe, and Mg, varied among samples in their concentration factors by up to two orders of magnitude. It further appears that the

upper mat samples concentrated metals to the lowest extent, and streamer samples to the highest extent, yet once again, caution must be exercised as exceptions to this generalization are numerous.

2.4 Discussion

2.4.1 Identification of mat ligands

A variety of organic ligands have been invoked as chemical moieties that contribute to the chemical reactivity of the microbial surface. Their putative assignment to ligand clusters modeled from acid-base titration data is based on spectroscopic data (e.g., infrared (Jiang et al., 2004) and x-ray adsorption (Boyanov et al., 2002; Kelly et al., 2002) spectroscopy) and comparisons with model organic acids in terms of acid-base behavior (e.g., Fein et al., 1997). Cox et al. (2001) used organic acid pK_a values from Martell and Smith (1989) to outline an approximate ligand classification scheme as follows: (1) carboxyl functional groups possess pK_a values in the range of 2 - 6, phosphoryl functional groups in the range of 6 - 7, amino functional groups in the range 9 - 11, and hydroxyl functional groups in the range 8 – 13.

In this study, the ligands determined for acid-washed samples might include representatives from all of the above categories. The ligand classification scheme employed in Table 2-1, where ligands are grouped into pK_a ranges of 4 – 6, 6 – 8, and 8-10, approximately correspond to the scheme of Cox et al., where the three classes represent carboxyl, phosphoryl, and hydroxyl/amino functional groups respectively. As spectroscopic evidence is required to confirm these identities, as well as distinguish between hydroxyl and amino functional groups whose pK_a values may overlap, these assignments should be regarded as strictly operational.

For the electrolyte-washed samples, we believe that the dominant ligand at pK_a ~7 does not represent an organic functional group because of its loss upon acid-washing. Instead, we consider this behaviour to be consistent with mat-associated carbonate minerals and/or dissolved inorganic carbon (mostly as bicarbonate, HCO_3^-) that are at least partially dissolved or removed from the biomass by acid-washing, but are not removed by the rinsing procedure of electrolyte-washed samples. Indeed, as discussed above, calcite grains were observed within the EPS matrix of all samples, and their presence indicates local conditions of calcite supersaturation consistent with the microscopic observations

indicating variably sized and located Ca-carbonate grains. A pK_a value of ~7 is in itself suggestive that the dissolution of calcite and/or production of H_2CO_3 from HCO_3^- is responsible for the dominant ligand, as the maximum buffer capacity for a closed system in equilibrium with calcite is around pH 7 (Langmuir, 1997). It is critical to note that the ligand concentrations of electrolyte-washed samples represent the combined contribution from both carbonate mineral grains and any mat-hosted aqueous carbonate species retained through the rinsing procedure, with the former dissolving to yield the latter over the course of titration. In other words, the ligand concentrations of electrolyte-washed samples are presumed to correspond to the total (aqueous + solid-phase) carbonate content of the mat.

For the electrolyte-washed samples, total ligand concentrations were lowest for the spires and streamers, higher for the upper laminated mat sections, and highest for the bottom laminated mat sections. This order is in general agreement with microscopy suggesting an abundance of calcite grains in thick laminated mat samples, with fewer grains contained in the spire and streamer structures. Such an observation is not unexpected given that the thick mat layers serve as diffusive barriers that prevent the rapid loss of soluble ions (e.g., HCO_3^-). This, in turn, maintains appropriate saturation states facilitating crystal growth. Conversely, soluble ions may be rapidly lost by diffusion and advection from the relatively thin spires and streamer structures.

Implicit in the above trends is the fact that the carbonate grains are authigenic in origin. Although we cannot be absolutely confident that some of the grains are not detrital, it is well known that cyanobacteria facilitate carbonate precipitation by the adsorption of Ca^{2+} cations to their cell surfaces and their metabolic production of HCO_3^- (Thompson and Ferris, 1992; Merz-Preiß, 2000). It is interesting to note that differences in organic surface functional group chemistry are small (total ligand concentrations ranging from 0.98 ± 0.28 to 2.84 ± 0.41 mmol g^{-1}) relative to differences attributable to carbonate mineral content (i.e., electrolyte-washed total ligand concentrations ranging from 6.12 ± 1.39 to 19.23 ± 3.14 mmol g^{-1}), suggesting that organic surface functional group chemistry was not a major determinant of the mat's aqueous or mineral carbonate content.

2.4.2 Balance between available ligands and sequestered metals

As discussed above, acid-leachable metal concentrations in the microbial mats ranged from 0.36 to 21 000 times their respective stream water concentrations, and most metals were concentrated by a factor of 10 to 1000. This is not surprising for an alkaline spring system (pH 9.2 in this case), where most anionic functional groups (e.g., carboxyl and phosphoryl) attributable to the biomass should be in a deprotonated state and thus available as anionic sites for metal cation adsorption. However, mat-associated metal concentrations were approximately 3 orders of magnitude less than the number of available ligands determined for either acid-washed and electrolyte-washed samples. In other words, by a large majority, proton-reactive ligands available within the microbial mats were unoccupied by metals. This fact, although counter-intuitive, is readily explained by the low concentrations of metals in the stream waters (see Table 2-1); at the stream pH of 9.2, the solubility of many of the metals examined in this study were very low. It is also worth noting that in this system, the microbial sequestration of metals is unlikely to affect aqueous metal concentrations, as the continuous supply of stream water approximates a flow-through system rather than a batch system, and the surfaces of interest should reach a steady-state equilibrium barring any chemical or biological change in the system. The end result is a system where metal adsorption is governed by equilibrium between metals in stream water and available ligands, the former of which is low, and the latter is high, as the result of elevated pH.

Nonetheless, it appears that there exist some relationships between biomass ligand availability and acid-leachable metal content (Fig. 2-9). As discussed above, and as readily apparent in Figure 2-9, the electrolyte-washed samples have higher ligand concentrations that we consider, on the basis of their pK_a values and effective removal by acid washing, to represent aqueous bicarbonate and/or mat-hosted carbonate mineral species. The total metal concentrations leached from the laminated mat samples (both upper and lower sections) correlated strongly with electrolyte-washed ligand concentrations (upper trend line), and to a lesser degree, with acid-washed ligand concentrations (lower trend line). In apparent discrepancy, the smaller mat structures (i.e., spires and streamers, individually labeled in Fig. 2-

9) had much lower electrolyte-washed ligand concentrations, yet still possessed concentrations of metals that were comparable to the laminated mats. This discrepancy might be best explained by their response to the rinsing procedure; although electrolyte-washed samples were not exposed to low pH conditions, they were thoroughly rinsed in titration electrolyte. It is possible that the aqueous carbonate content of the smaller mat structures was removed to some extent during rinsing, as a consequence of their large surface area to volume ratios; the thicker laminated mat samples are likely to have better retained their aqueous carbonate contents during the rinse procedure simply because of their thickness. As a result, the spire and streamer structures provided low ligand concentrations during titration of electrolyte-washed samples, yet acid-washes of similar samples yielded metal concentrations that are comparable to the laminated structures. The relative roles in metal retention of mat-associated aqueous carbonate complexes and solid-phase carbonate minerals deserves further study; the apparent correlation between electrolyte-washed ligand concentrations and acid-leached metal concentrations does not distinguish metal carbonate minerals as the primary source of metals relative to aqueous metal carbonate complexes, and as discussed above, it is likely that the electrolyte-washed ligand concentrations represent the sum of both. In a retrospective and cautionary note, critical sample selection and careful preparatory techniques (i.e., sectioning mat biomass into parts of equal dimensions) may help avoid similar difficulties in the future study of metal sequestration by microbial mat structures.

In the case of the laminated mat samples, the apparent correlation of acid-leachable metal concentrations with both acid-washed and electrolyte-washed ligand concentrations is interesting, but unfortunately it provides little information regarding any definitive means of metal sequestration in these mats, whether by authigenic mineral precipitation, detrital entrapment, or surface adsorption. The correlations do indicate, however, that within a single hydrothermal system, and even over an area as small as the one detailed herein, variability in the chemical reactivity or metabolic activity of microbial mats may be sufficiently high as to be reflected in the concentrations of metals the mats sequester.

2.4.3 Trends in metal sequestration

Our work shows that various elements are concentrated to different extents by the microbial mats. Metals of low K_d values (0.5 – 1), such as Al, As, Cs, Li, Rb, and Ti, are only slightly concentrated by the mats, in an apparently non-specific manner; this is consistent with laboratory experiments demonstrating general non-specificity during metal sorption by bacterial surfaces (e.g., Fein et al., 2001). However, those metals most concentrated by the mats (with K_d values > 2), such as Ca, Fe, Mn, Sr, Zn, Ba, and Mg, are preferentially sequestered in a manner that is inconsistent with non-specific adsorption to organic mat components. Importantly, these metals are primarily divalent cations with relatively low anhydrous metal carbonate solubility products (K_{sp}),:

$$MeCO_{3(s)} \leftrightarrow Me^{2+} + CO_3^{2-}, \qquad K_{sp} = [Me^{2+}][CO_3^{2-}] \qquad (3)$$

In other words, saturation for their respective metal carbonates may be achieved at low $[Me^{2+}]$ and $[CO_3^{2-}]$ values, and thus, these divalent metals are readily sequestered by co-precipitation with, or sorption to, calcium carbonate. Indeed, when their metal carbonate solubility products (K_{sp} values from the WATEQ4F database, Ball and Nordstrom (1991)) are plotted against their respective biomass distribution coefficients, it becomes evident that their mat distribution coefficients increase as a function of increasing solubility, with the exception of Ca and Zn (Figure 2-10). At first glance, this might indicate that these metals were sequestered in their metal carbonate form, and that the extent to which they were dissolved by the acid-leaching procedure depended on their respective mineral solubilites.

Stability constants for aqueous metal complexation by oxalate are also presented in Figure 2-10, because it has been previously demonstrated that the adsorption of metals to bacterial surfaces are correlated to some extent with their degree of aqueous complexation by simple carboxylic acids such as oxalate (Fein et al., 2001). This apparent correlation is not surprising given the chemical homology between carboxylic acids on the bacterial surface and those of simple organic acids such as oxalate; in fact, the same principal of chemical homology explains why metal distribution coefficients in Figure 2-10 correlate with both

calcium carbonate solubility and oxalate complex stability. The stability constants of aqueous oxalate ($CH_3O_2^-$) and carbonate (CO_3^{2-}) metal complexes are known to correlate with each other as the result of their similarity in size, geometry, electron configurations and other bonding properties (Langmuir, 1997).

The elements Ca and Zn, found at higher concentrations in the stream waters than the other carbonate-forming elements, poorly adhere to the above stability constant relationships. Zachara et al. (1991) previously investigated the sorption of divalent metals to calcite surfaces, and found that Zn deviates from other metals in the relationship between its calcite surface stability constant and its ionic radius relative to Ca, implying that additional factors related to the Zn atom's electronic structure may additionally influence its sorption to calcite. However, in a plot similar to Figure 2-10, they find that the sorption of Zn is equally related to its metal carbonate solubility product. According to the observed trends, Zn should have been found at higher surface concentration to correlate with its oxalate stability constant, and at lower surface concentrations to correlate with its metal carbonate solubility product. It is possible that this represents competition between organic and carbonate ligands for available Zn, however given the limited data, unknown factors may be equally responsible.

With respect to both apparent correlations, calcium was consistently found at low concentrations. This trend may represent either incomplete dissolution of calcium carbonate grains or a failure for calcium to desorb from organic components during acid-washing. In the case of the former, time-lapsed dissolution experiments (unpublished) indicated that the larger grains (as shown in Fig. 2-4A) were not completely removed within the 30 min acid-leach procedure. At the same time, the latter hypothesis may be equally valid, as carboxylic functional groups that were conspicuously absent from the acid-washed pK_a spectra may have been 'masked' by cation occupancy even after the acid-washing procedure, as discussed above.

While interesting, the simultaneous correlation of metal distribution coefficients with metal carbonate K_{sp} values and metal-oxalate stability constants complicates any efforts to determine which metals may have been adsorbed to

biomass vs. those that may have been hosted in carbonate minerals and subsequently released during acid-leaching. Overall, these results highlight the fact that metal distribution coefficients reflecting metal sequestration by natural microbial biomass may be highly ordered according to the thermodynamic properties of individual metals (e.g., ionic radius, ionic potential, electron configurations), yet vague in relation to actual sequestrative processes because of chemical homology between organic and mineral components in a natural microbial community.

It is clear that despite the analysis presented above, authigenic mineral precipitation, detrital entrapment, and surface adsorption all remain viable as mechanisms that may have lead to metal sequestration by the microbial mats. It is possible, if not probable, that all three processes occur simultaneously in this complex microbial community. At the very least, the results presented herein emphasize some of the difficulties inherent to the mechanistic understanding of metal sequestration in natural microbial systems. Perhaps more importantly, this study highlights the need for an encompassing view of metal sequestration by natural microbial assemblages that includes, but also looks beyond, organic surface complexation reactions. At least in this case, the partitioning of metals into a heterogeneous assemblage of cells, EPS, and diverse minerals must be considered in light of the fact that, despite their close proximity within in a single hydrothermal spring, such microbial communities may be highly varied with respect to their mineral content, organic surface reactivity, metabolic activity, and physical factors such as mat structure (e.g., streamer vs. spire vs. laminated mat) and permeability. It is clear from this preliminary work that future studies aiming to evaluate the microbial sequestration of metals may benefit from the use of natural samples for which laboratory analogues are poor or wholly unavailable.

2.5 Conclusion

Natural microbial mats grow under environmental conditions that are difficult, if not impossible to replicate, and the study of such systems may reveal complex geochemical processes that are not easily reproduced in a laboratory setting. Metal sequestration by microbial biomass is one such process, where simple laboratory analogues have been well characterized, but their relevance towards natural systems has remained untested. In order to better understand microbial metal sequestration as it occurs in natural settings, cyanobacterial mats of diverse morphology were collected from a small area within a single alkaline hydrothermal spring, Yellowstone National Park, and critically assessed for their ability to sequester metals from solution. Metal distribution coefficients indicate that some metals are non-specifically adsorbed, while other metals, primarily divalent cations characterized by low metal carbonate solubility products, were more strongly sequestered. While the latter might indicate sequestration by authigenic precipitation or detrital entrapment of carbonate mineral phases, a critical evaluation of pertinent thermodynamic parameters fails to distinguish whether these metals were sourced from mineral or organic mat components. Microscopy and acid-base titrations of electrolyte-washed samples demonstrate that the mats differ in their carbonate mineral content, and titrations of acid-washed samples imply that there exists some of degree of variation between mats in the surface functional group chemistry of their organic components, despite the close proximity of mats within the hydrothermal feature. Total metal concentrations in the biomass correlated with both carbonate (electrolyte-washed) ligand concentrations and native organic (acid-washed) ligand concentrations, again failing to distinguish the exact mechanisms responsible for metal sequestration within the diverse mat structures. These results demonstrate that over small spatial areas, the extent of metal sequestration by diverse cyanobacterial mats may vary significantly, and that such variations may arise from the combined influences of metabolic activity, mineral phase entrapment and/or authigenic precipitation, and by the differences in surface functional group chemistry and physical organization of organic mat components. This study, being one of the first to evaluate metal

sequestration by natural biomass in a framework relevant to surface adsorption models, highlights important considerations in the extrapolation of microbe-metal interaction from simple laboratory experiments to complex and heterogeneous environmental samples.

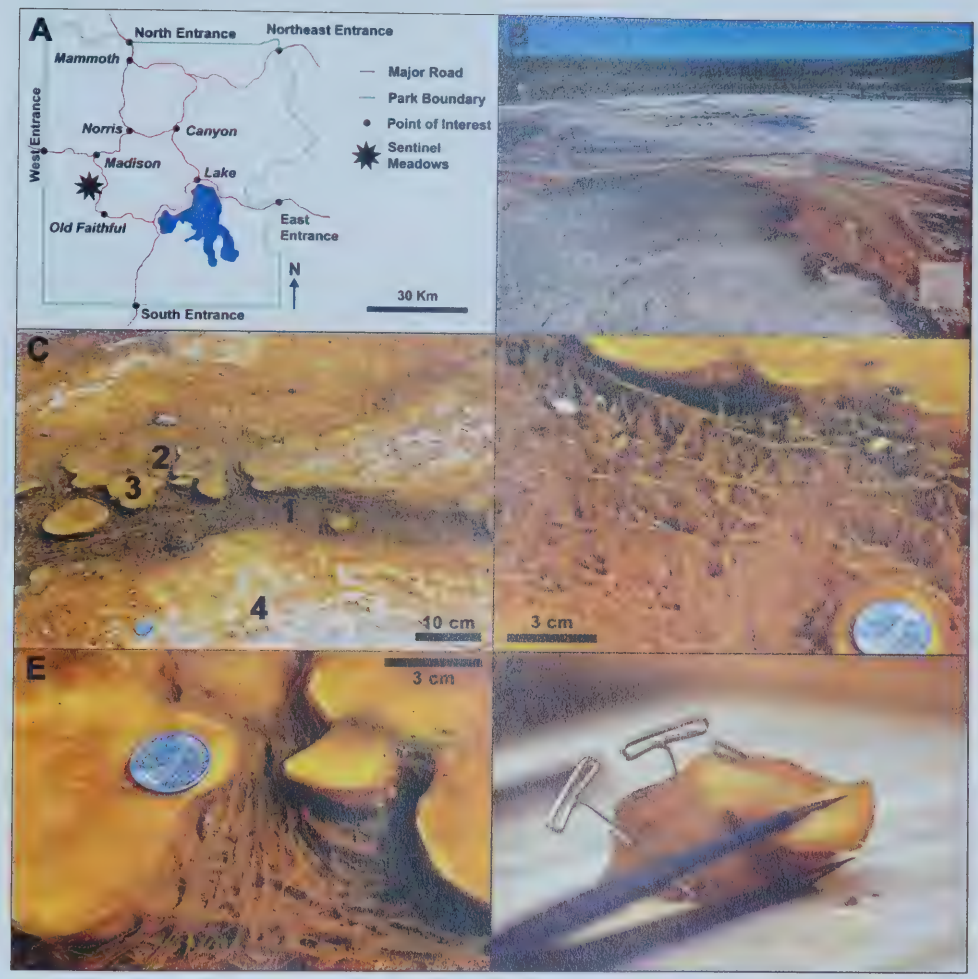

Figure 2-1. Site map (A) and photographs (B-F) showing sample location and mat morphologies. (B) All samples were obtained within an area ~2.5 m^2 (highlighted by white box) that lay ~8 meters from the spring source, chosen for the localized presence of well-developed microbial mats of diverse morphology. The relative position of samples representing four mat morphologies are indicated on (C): (1) subaqueous samples with vertical spire morphology (shown enlarged in (D)) were collected from a small pooled section of stream, (2) samples with streamer morphology were collected from the pool outflow channel (upper part of

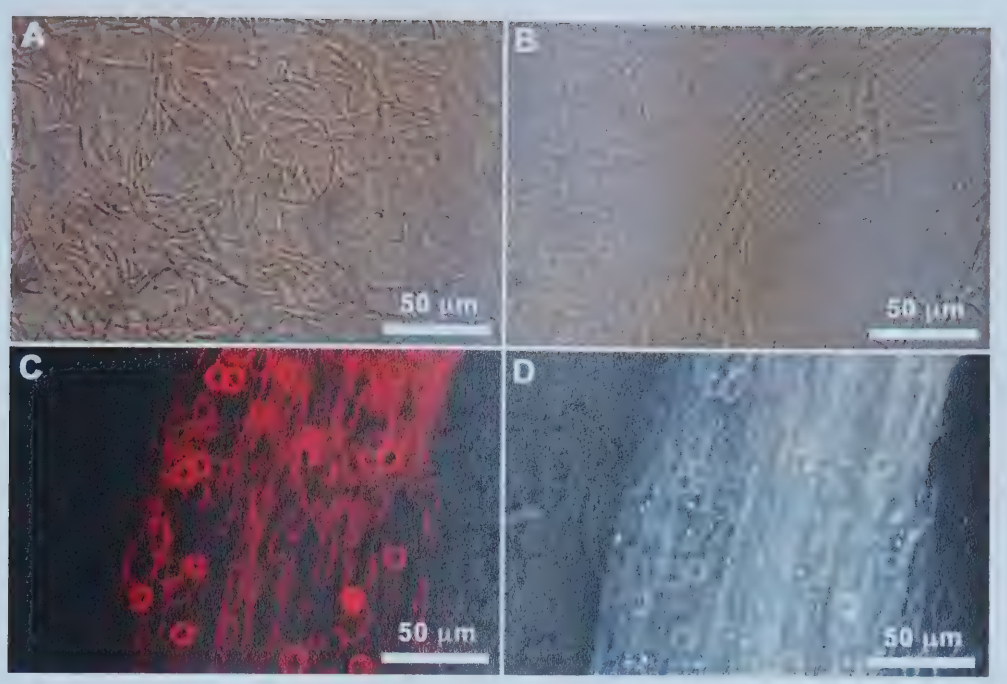

Figure 2-2. Light micrographs depicting microbial community structure within the rigid vertical spires (A-B) and streamers (C-D). The vertical spires are dominated by filamentous bacteria that vary throughout the samples between random (A) and highly aligned (B) orientations. The streamer samples are dominated by filamentous bacteria of similar cell size and filament length, however in these samples some filaments assumed a tightly coiled form (C). In all samples, the filamentous bacteria clearly possessed photosynthetic pigments, as indicated by their strong autofluorescence (e.g., (C)). Dark-field photomicrographs revealed that the streamer samples were incased in a dense matrix of EPS (D); indeed, dark-field microscopy indicated that all biomass samples were incased, to various degrees, in an EPS matrix.

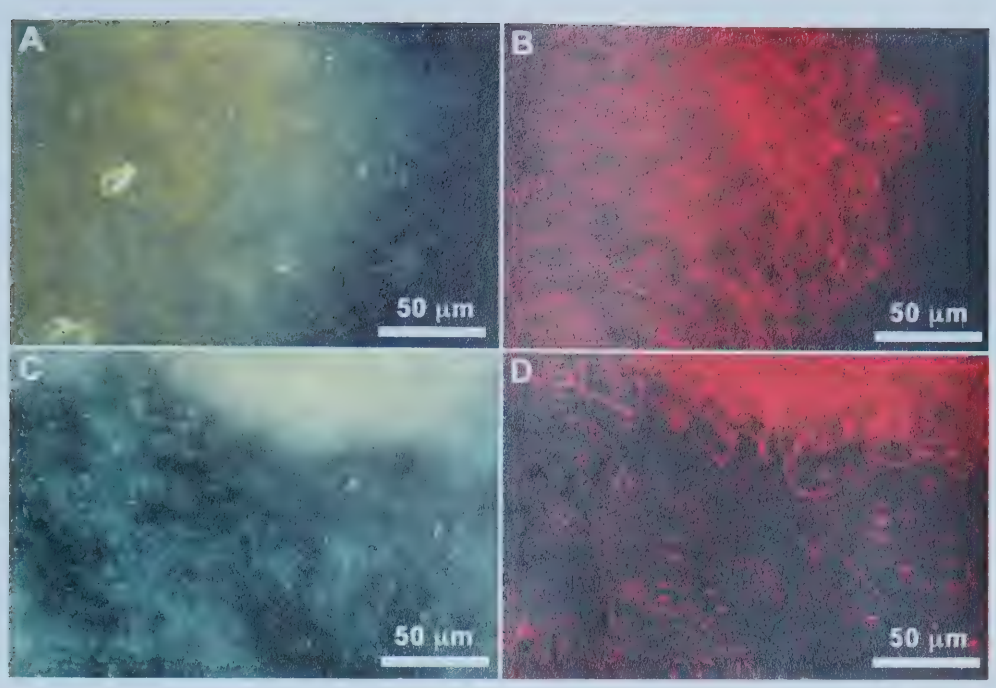

Figure 2-3. Dark-field and epifluorescent micrographs indicate that the upper 5 mm of both laminated mats consists of a dense EPS matrix (A) hosting randomly-aligned filamentous phototrophs (B). Lower sections of the mats show patches of more and less dense EPS (C), the former being occupied by a mix of phototrophic rod-shaped and filamentous cells, and the latter by mostly rod-shaped cells, not all of which displayed autofluorescence (D).

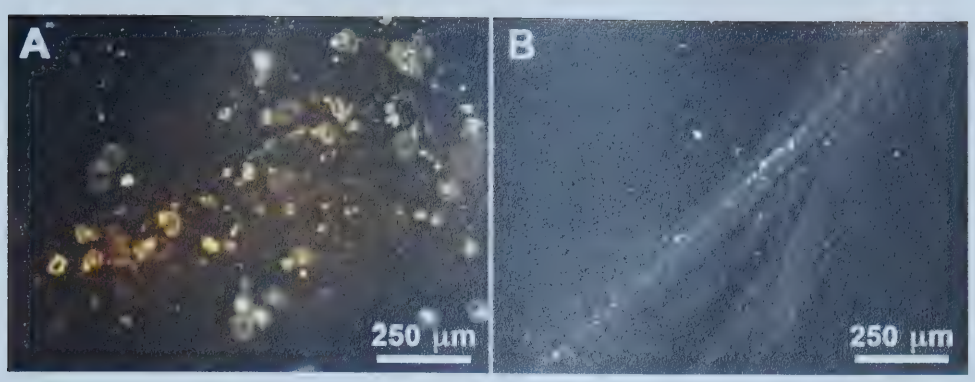

Figure 2-4. Mineral grains of diverse size and morphology were observed in all samples. Crossed-polar light micrographs revealed strong birefringence for some mineral grains, and in consideration of the alkaline stream and mat chemistry, suggest potentially-authigenic carbonates. In the upper layers of the laminated mats, mineral grains larger than 20 mm were abundant (A), while in the lower layers of the laminated mats, as well as in the vertical spires and streamers (imaged in (B)), grains larger than 20 mm were absent, and smaller grains (< 5 mm) dominated.

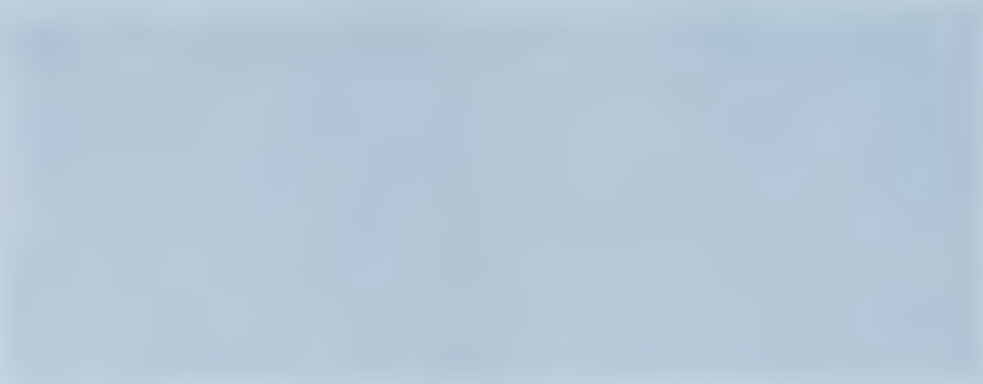

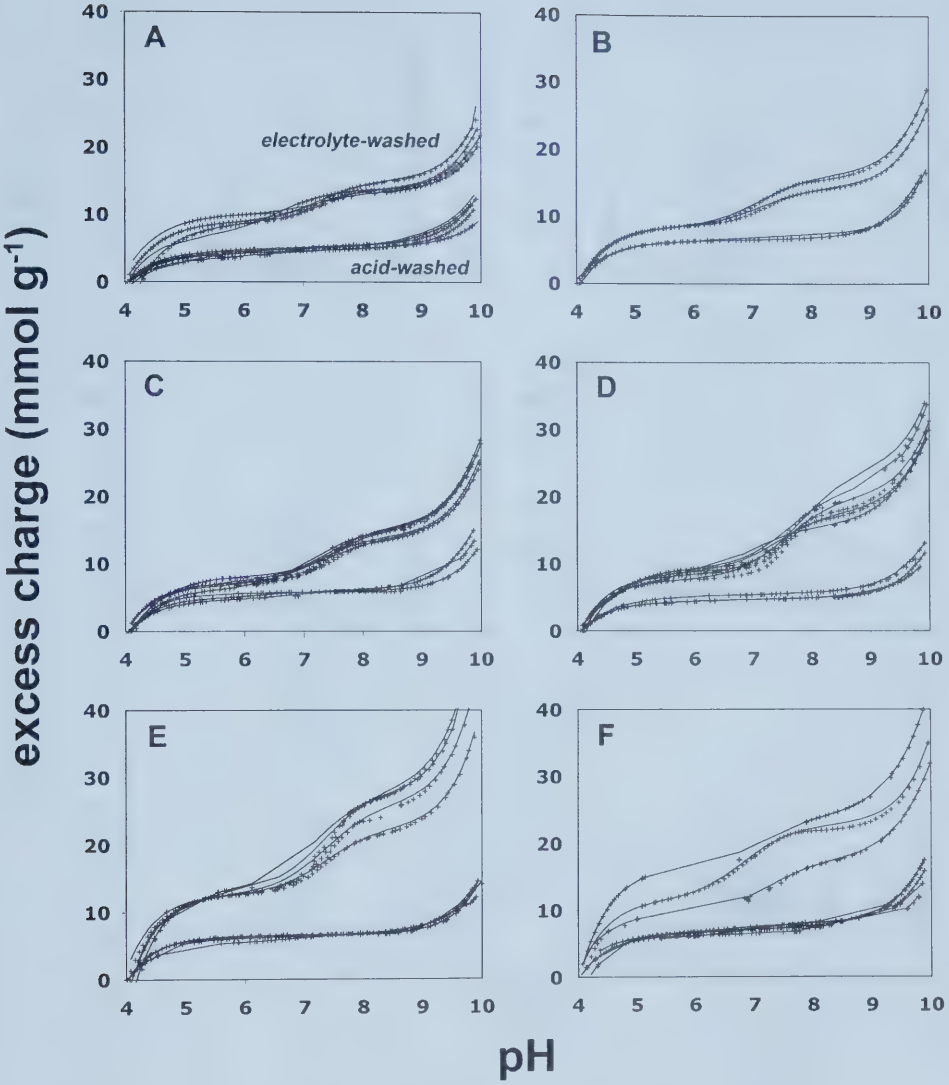

Figure 2-5. Acid-base data presented as excess charge in the titration system. Excess charge plots of electrolyte-washed and acid-washed mat preparations are as follows: (A) spire structures, (B) streamers, (C) upper 5 mm and (D) lower portions of yellow mat, and (E) upper 5 mm and (F) lower portions of white mat. Titration data is plotted as points, and lines demonstrate the excess charge fit by pK_a spectra models.

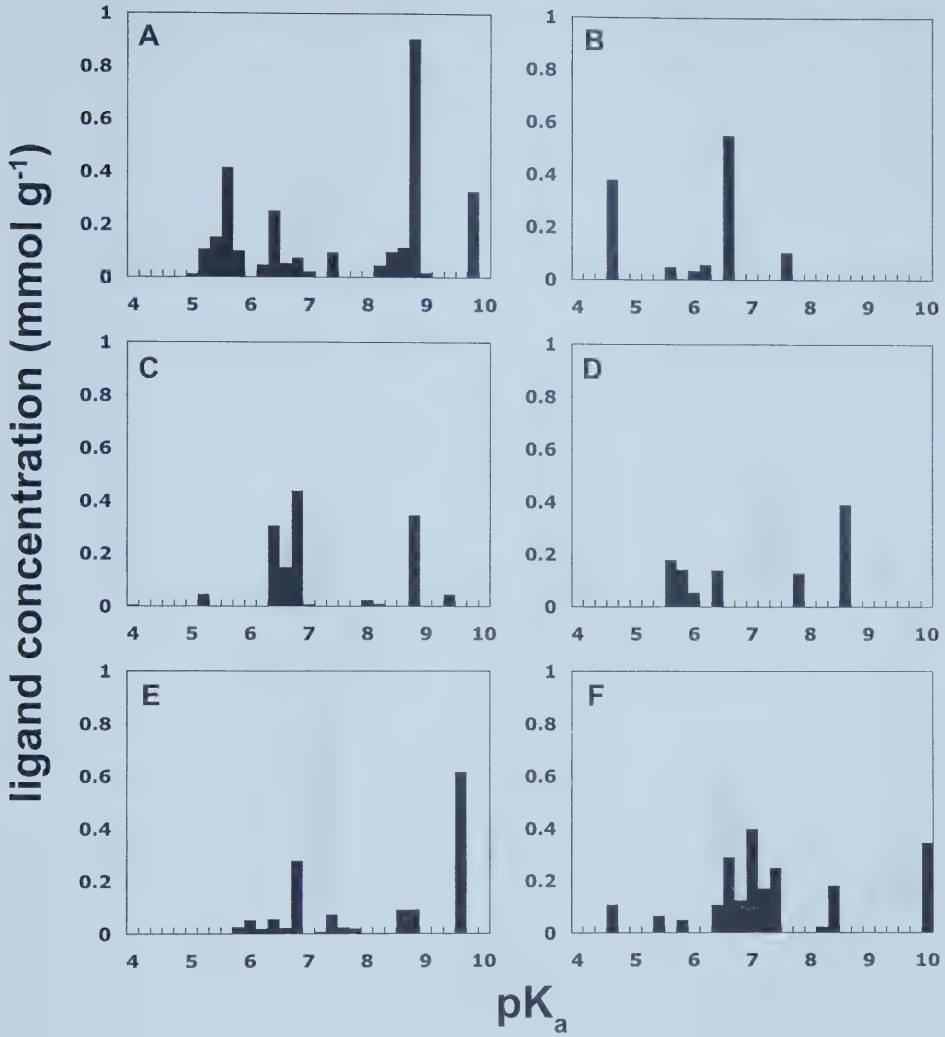

Figure 2-6. The concentrations and pK_a values of ligands modeled from excess charge data of acid-washed samples are diverse: (A) spires, (B) streamers, (C) upper and (D) lower yellow mat, and (E) upper and (F) lower white mat. Ligand concentrations were summed over all replicates and divided by the total weight of all replicates in order to generate the composite plots presented above.

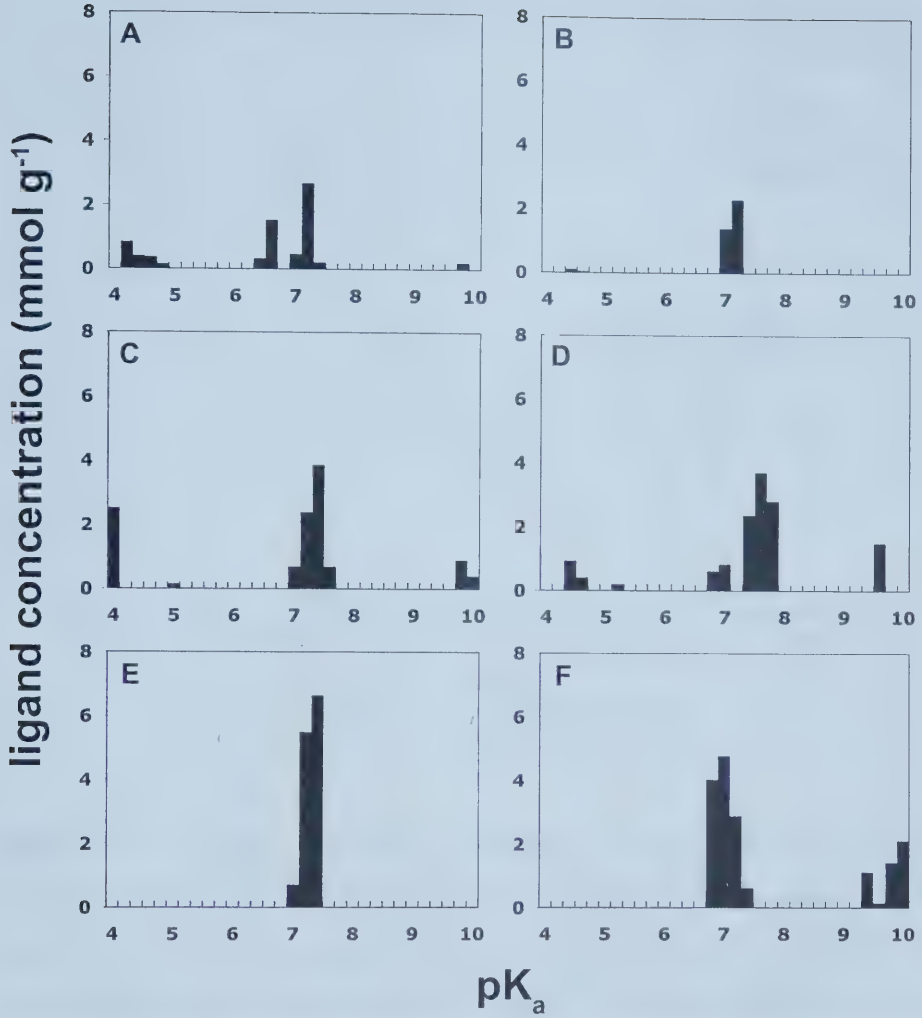

Figure 2-7. pK_a spectra of ligands modeled from excess charge data of electrolyte-washed samples reveal elevated concentrations and the dominance of a conserved ligand around pK_a 7: (A) spires, (B) streamers, (C) upper and (D) lower yellow mat, and (E) upper and (F) lower white mat. Ligand concentrations were summed over all replicates and divided by the total weight titrated of replicates in order to generate the composite plots presented above.

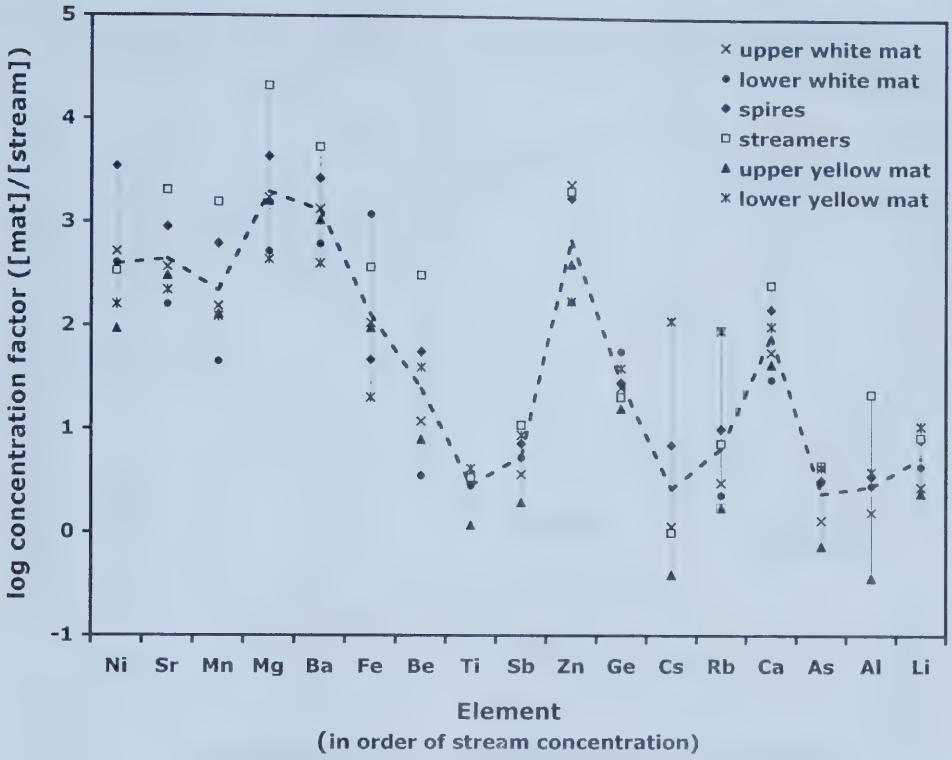

Figure 2-8. A log plot of distribution coefficients, arranged in order of increasing stream concentration, reveals specificity in the adsorption of trace metals from the aqueous phase. Values ranged from less concentrated to nearly 21,000X more concentrated on the biomass than in the stream. The high-low bars demonstrate the spread in values between samples for each element about the mean values (dotted line).

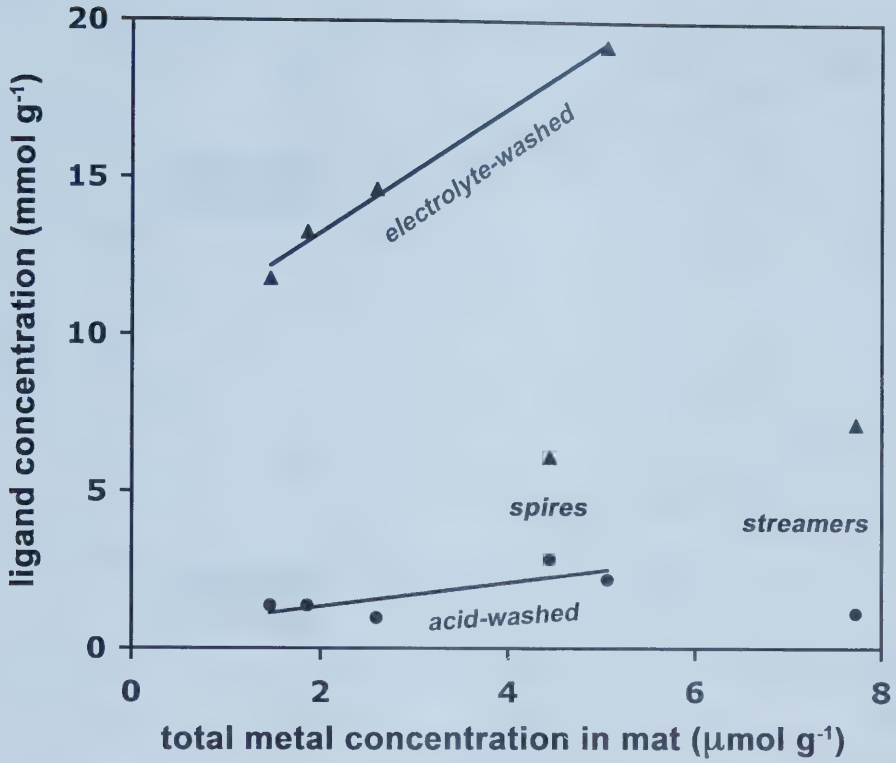

Figure 2-9. Relationships between total mat metal concentrations and ligands determined for both acid-washed (●) and electrolyte-washed (▲) preparations. All of the laminated mat samples show correlations between ligand and metal concentrations, while the spire and streamer samples (labeled) are discrepant.

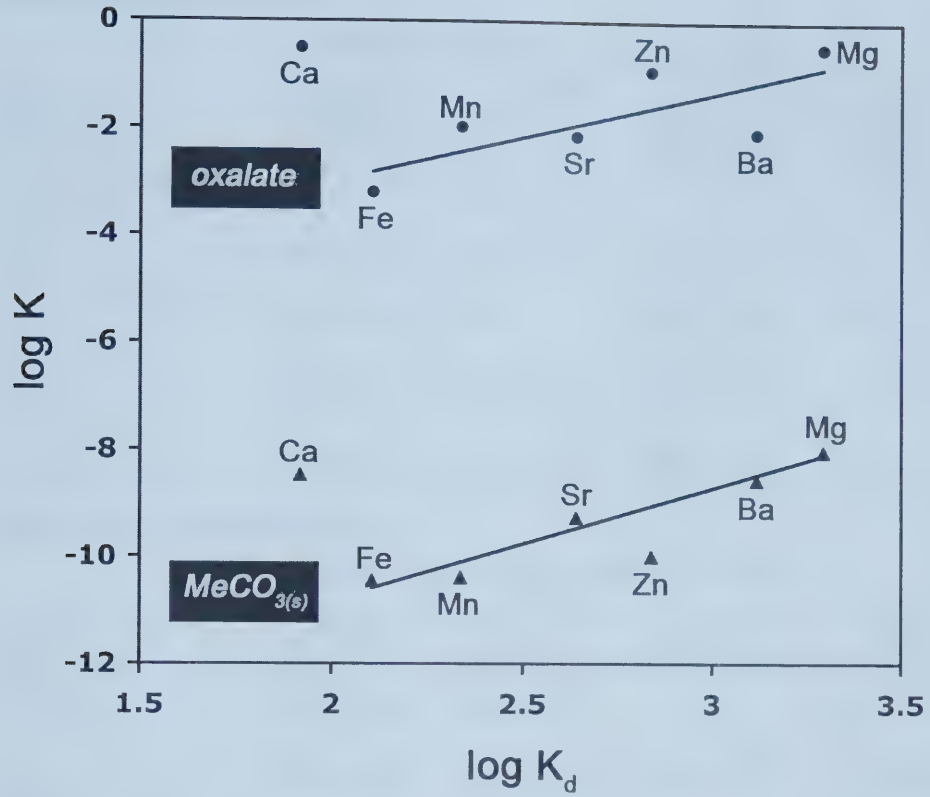

Figure 2-10. A plot of anhydrous metal carbonate ($MeCO_{3(s)}$) solubility products (K_{sp}) vs. their average biomass distribution coefficients displays a strong linear relationship ($R^2 = 0.97$) for most of the carbonate-forming metals. Ca and Zn are treated as outliers and omitted from this regression (see text). However, a similarly linear relationship is observed with Me-oxalate stability constants ($R^2 = 0.60$, Ca omitted), highlighting the difficulty in relating metal sequestration to either mineral precipitation or biomass adsorption from a thermodynamic standpoint.

Acid-washed preparations

Sample	ligand concentration (mmol g^{-1}) per pK_a class			
	4 to 6	6 to 8	8 to 10	Total
spires (n=5)	0.77 ± 0.25	0.53 ± 0.19	1.54 ± 0.38	2.84 ± 0.41
streamers (n=2)	0.40 ± 0.40	0.73 ± 0.28	nd	1.13 ± 0.68
upper yellow mat (n=3)	0.05 ± 0.04	0.88 ± 0.35	0.42 ± 0.31	1.36 ± 0.59
lower yellow mat (n=3)	0.32 ± 0.18	0.35 ± 0.11	0.32 ± 0.32	0.98 ± 0.28
upper white mat (n=5)	0.03 ± 0.03	0.55 ± 0.18	0.79 ± 0.58	1.36 ± 0.76
lower white mat (n=5)	0.25 ± 0.14	1.28 ± 0.38	0.29 ± 0.29	2.20 ± 0.61

Electrolyte-washed preparations

Sample	ligand concentration (mmol g^{-1}) per pK_a class			
	4 to 6	6 to 8	8 to 10	Total
spires (n=5)	1.46 ± 0.71	4.53 ± 1.13	0.14 ± 0.14	6.12 ± 1.39
streamers (n=2)	0.31 ± 0.02	6.87 ± 0.97	nd	7.18 ± 0.98
upper yellow mat (n=5)	2.67 ± 2.48	7.68 ± 0.49	0.97 ± 0.97	11.77 ± 2.28
lower yellow mat (n=5)	1.76 ± 1.02	11.32 ± 1.45	1.54 ± 1.54	14.62 ± 1.21
upper white mat (n=4)	nd	13.26 ± 1.17	nd	13.26 ± 1.17
lower white mat (n=5)	2.16 ± 2.16	9.96 ± 3.69	5.76 ± 3.31	19.23 ± 3.14

Table 2-1. Modeled ligand concentrations of all samples, grouped by preparation method and further classified by ligand pK_a range. Uncertainty is expressed as one standard error.

element	stream conc. (mM)	mat concentration (mmol/Kg) spires	streamers	upper yellow mat	lower yellow mat	upper white mat	lower white mat
Li	2.46E+02	2.73E+03	2.11E+03	6.03E+02	6.95E+02	1.11E+03	2.02E+03
Al	1.53E+01	6.08E+01	3.44E+02	5.57E+00	2.46E+01	4.43E+01	5.47E+01
As	1.47E+01	6.38E+01	6.71E+01	1.09E+01	1.94E+01	4.66E+01	4.83E+01
Ca	1.18E+01	1.22E+03	3.07E+03	5.14E+02	6.79E+02	3.68E+02	1.79E+03
Rb	1.38E+00	1.30E+02	1.03E+01	2.43E+00	4.28E+00	3.20E+00	1.42E+01
Cs	6.88E-01	7.98E+01	6.90E-01	2.68E-01	7.97E-01	6.83E-01	4.95E+00
Ge	6.58E-01	2.62E+01	1.37E+01	1.07E+01	1.70E+01	3.82E+01	1.91E+01
Zn	3.99E-01	7.05E+01	8.22E+02	1.61E+02	9.57E+02	6.93E+01	7.04E+02
Sb	3.86E-01	3.41E+00	4.26E+00	7.58E-01	1.42E+00	2.06E+00	2.85E+00
Ti	3.84E-01	1.62E+00	1.31E+00	4.53E-01	1.26E+00	1.09E+00	1.37E+00
Be	1.57E-01	6.30E+00	4.87E+01	1.25E+00	1.89E+00	5.62E-01	8.91E+00
Fe	8.80E-02	1.76E+00	3.21E+01	8.35E+00	9.35E+00	1.05E+02	4.12E+00
Ba	8.00E-02	3.19E+01	4.30E+02	8.39E+01	1.07E+02	4.93E+01	2.13E+02
Mg	3.50E-02	1.54E+01	7.43E+02	5.71E+01	6.12E+01	1.85E+01	1.54E+02
Mn	1.00E-02	1.21E+00	1.53E+01	1.26E+00	1.52E+00	4.45E-01	6.14E+00
Sr	6.00E-03	1.28E+00	1.18E+01	1.75E+00	2.13E+00	9.31E-01	5.26E+00
Ni	4.00E-03	5.64E-01	1.19E+00	3.26E-01	1.84E+00	1.44E+00	1.23E+01
Sum	2.92E+02	4.44E+03	7.72E+03	1.46E+03	2.58E+03	1.86E+03	5.06E+03
Cl^-	2.24E+02						
F^-	2.38E+01						
SO_4^{2-}	1.59E+01						
Total Alkalinity	5.05E+03						
pH	9.20						
Temp. (°C)	46.0						
Ionic strength (M)	1.10E-02						

Table 2-2. Concentrations of various elements in stream water and their corresponding mat concentrations as inferred by acid-washing. Elements are arranged by their stream water concentration. Also included for stream water are basic parameters as well as principle anion concentrations as determined by ion chromatography. In the case of mat concentrations, values are mmol per Kg of biomass. See methods for detection limits and uncertainty.

2.6 References

Ball, J.W., Nordstrom, D.K., 1991. WATEQ4F--User's manual with revised thermodynamic database and test cases for calculating speciation of major, trace and redox elements in natural waters. U.S. Geological Survey Open-File Report 90-129, 185 pg.

Beveridge, T.J., Murray, R.G.E., 1980. Sites of metal deposition in the cell wall of Bacillus subtilis. Journal of Bacteriology 141, 876–887.

Borrok, D., Fein, J.B., 2005. The impact of ionic strength on the adsorption of protons, Pb, Cd, and Sr onto the surfaces of gram-negative bacteria: testing non-electrostatic, diffuse, and triple-layer models. Journal of Colloidal and Interface Science 286, 110-126.

Borrok, D., Fein, J.B., Tischler, M., O'Loughlin, E., Meyer, H., Liss, M., Kemner, K.M., 2004. The effect of acidic solutions and growth conditions on the adsorptive properties of bacterial surfaces. Chemical Geology 209, 107-109.

Boyanov M.I., Kelly, S.D., Kemner, K.M., Bunker, B.A., Fein, J.B., and Fowle, D.A., 2002. Adsorption of cadmium to *B. subtilis* bacterial cell walls – a pH-dependent XAFS spectroscopy study. Geochimica et Cosmochimica Acta 67, 3299–3311.

Brassard, P., Kramer, J.R., Collins, P.V., 1990. Binding site analysis using linear programming. Environmental Science Technology 24, 195-201.

Cox, J.S., Smith, D.S., Warren, L.A., Ferris, F.G., 1999. Characterizing heterogeneous bacterial surface functional groups using discrete affinity spectra for proton binding. Environmental Science Technology 33, 4514–4521.

Fein, J.B., Boily, J.F., Yee, N., 2005. Potentiometric titrations of Bacillus subtilis cells to low pH and a comparison of modeling approaches. Geochimica et Cosmochimica Acta 69, 1123-1132.

Fein, J.B., Daughney, C.J., Yee, N., Davis, T.A., 1997. A chemical equilibrium model for metal adsorption onto bacterial surfaces. Geochimica et Cosmochimica Acta 61, 3319-3328.

Fein, J.B., Martin, A.M., Wightman, P.G., 2001. Metal adsorption onto bacterial surfaces: Development of a predictive approach. Geochimica et Cosmochimica Acta 65, 4267-4273.

Fowle, D.A., Fein, J.B., 1999. Competitive adsorption of metal cations onto two gram-positive bacteria: testing the chemical equilibrium model. Geochimica et Cosmochimica Acta 63, 3059-3067.

He, L.M, Tebo, B.M., 1998. Surface charge properties of and Cu(II) adsorption by spores of the marine Bacillus sp. strain SG-1. Applied and Environmental Microbiology 64, 1123-1129.

Jiang W., Saxena A., Song B., Ward B.B., Beveridge T.J., and Myneni S.C.B. (2004) Elucidation of functional groups on Gram-positive and Gram-negative bacterial surfaces using infrared spectroscopy. *Langmuir* **20**, 11433-11442.

Kelly S.D., Kemner, K.M., Fein, J.B., Fowle, D.A., Boyanov, M.I., Bunker, B.A., and Yee, N., 2002. X-ray absorption fine structure determination of pH-dependent U-bacterial cell wall interactions. Geochimica et Cosmochimica Acta 66, 3855–3871.

Konhauser, K.O., 2006. Introduction to Geomicrobiology. Blackwell Publishing, Oxford, UK.

Konhauser, K.O., Urrutia, M.M., 1999. Bacterial clay authigenesis: a common biogeochemical process. Chemical Geology 161, 399–413.

Langmuir, D., 1997. Aqueous Environmental Geochemistry. Prentice-Hall: Upper Saddle River, NJ.

Martinez, R.E., Ferris, F.G., 2001. Chemical equilibrium modeling techniques for the analysis of high-resolution bacterial metal sorption data. Journal of Colloidal and Interface Science 243, 73-80.

Martinez, R.E., Smith, D.S., Kulczycki, E., Ferris, F.G., 2002. Determination of intrinsic bacterial surface acidity constants using a Donnan shell model and a continuous pK_a distribution method. Journal of Colloidal and Interface Science 253, 130-139.

Merz-Preiß, M., 2000. Calcification in cyanobacteria. In: Riding, R.E. and Awramik, S.M. (eds), Microbial Sediments. Springer-Verlag, Berlin, pp. 51–56.

Phoenix, V.R., Martinez, R.E., Konhauser, K.O., Ferris, F.G., 2002. Characterization and implications of the cell surface reactivity of the cyanobacteria Calothrix sp. Applied And Environmental Microbiology 68, 4827-4834.

Plette, C.C., Van Riemsdijk, W.H., Benedetti, M.F., Van der Wal, A., 1995. pH dependent charging behavior of isolated cell walls of a gram-positive soil bacterium. Journal of Colloidal and Interface Science 173, 354–363.

Smith, D.S., Adams, N.W.H, Kramer, J.R., 1999. Resolving uncertainty in chemical speciation determinations. Geochimica et Cosmochimica Acta 63, 3337-3347.

Smith, D.S., Kramer, J.R., 1999 Multi-site proton interactions with natural organic matter. Environment International 25, 307-314.

Sokolov, I., Smith, D.S., Henderson, G.S., Gorby, Y.A., Ferris, F.G., 2001. Cell surface
electrochemical heterogeneity of the Fe(III)-reducing bacteria Shewanella putrefaciens. Environmental Science Technology 35, 341-347.

Thompson, J.G., Ferris, F.G., 1990. Cyanobacterial precipitation of gypsum, calcite, and magnesite from natural alkaline lake water. Geology 18, 995–998.

Yee, N., Fowle, D.A., Ferris, F.G., 2004. A Donnan potential model for metal sorption onto Bacillus subtilis. Geochimica et Cosmochimica Acta 68, 3657-3664

Zachara, J.M., Cowan, C.E., Resch, C.T. 1991. Sorption of divalent metals on calcite. Geochimica et Cosmochimica Acta 55, 1549-1562.

CHAPTER 3

Chemical Reactivity of Microbe and Mineral Surfaces in Hydrous Ferric Oxide Depositing Hydrothermal Springs[1]

3.1 Introduction

Chemical reactions occurring at the solid-water interface, including adsorption, ion-exchange, hydrolysis, precipitation, polymerization, oxidation-reduction, and dissolution, are dependant upon the surface charge characteristics of the submerged substratum (Davis and Kent, 1990). Surface charge, in turn, is determined by the properties and concentrations of chemical functional groups (FGs) exposed to the aqueous environment. Some minerals, such as micas, zeolites, and clay minerals, possess permanent structural surface charges resulting from cationic substitution within their crystal lattice, while others, such as metal oxyhydroxides and complex organic macromolecules, develop charge solely as the result of surface functional group protonation/deprotonation reactions (Langmuir, 1997). For example, the typical negative charge associated with the cell walls and extracellular layers of microorganisms develops as a function of pH, primarily via the following four functional group deprotonation reactions:

$$R\text{-}COOH \rightarrow R\text{-}COO^- + H^+ \quad (1)$$

$$R\text{-}PO_4H_2 \rightarrow R\text{-}PO_4H^- + H^+ \quad (2)$$

$$R\text{-}NH_3^+ \rightarrow R\text{-}NH_2 + H^+ \quad (3)$$

$$R\text{-}OH \rightarrow R\text{-}O^- + H^+ \quad (4)$$

where R represents a microbial surface. Reactions (1) and (2) proceed spontaneously at neutral pH, and the deprotonated ligands are responsible for the bulk of the overall negative cell surface charge typical at pH values greater than ~3

[1]A version of this chapter has been published. Lalonde SV, Amskold L, McDermott TR, Inskeep WP, and Konhauser KO. *Geobiology* **5**, 219-234 (2007).

(Bayer and Sloyer, 1990). Reaction (3) occurs at pH values between 8-11 (Hunt, 1986), and reaction (4) only becomes significant at pH values around 11 (Martell and Smith, 1989), thus negligibly affecting microbial surface charge under most conditions. These functional groups also act as efficient ligands for the complexation of various cations and as nucleation sites for a variety of authigenic mineral phases (see Konhauser, 2007 for details). Importantly, the large surface area-to-volume ratios of most microorganisms, their ubiquity in the environment, and in many cases their high population densities, make them extremely important agents in biogeochemical cycles, particularly with respect to elemental partitioning.

Many minerals also possess highly reactive surfaces that exert control over the chemistry of solutions with which they are in contact. Hydrous ferric oxides have received significant attention due to their widespread occurrence and high sorptive capacity; indeed, numerous HFOs have been studied as model surfaces for surface complexation reactions (e.g., Dzombak and Morel, 1990). HFOs are poorly ordered minerals with relatively large surface area (Roden, 2003), and are dominated by basic hydroxyl surface functional groups (e.g., Smith and Ferris, 2001). Such minerals have been shown to precipitate rapidly in environments where Fe(II)-bearing waters come into contact with O_2 at pH > 4. Microorganisms are often implicated in HFO formation, playing either a completely passive role, i.e., becoming covered by abiological precipitates; facilitating mineral nucleation by providing ligands to adsorb dissolved Fe species; or an active role, by causing mineral precipitation through their metabolic oxidation of Fe(II) (Konhauser, 1998).

Solute adsorption to a biological or mineral surface is dictated by the structural and compositional nature of the exposed functional groups, as well as the unique physico-chemical properties of each sorbate forming a surface complex. Spectroscopic methods, such as Fourier transform infrared spectroscopy (FTIR), X-ray absorption near edge structure (XANES), X-ray absorption fine structure (XAFS), and electron energy loss spectroscopy (EELS), can provide detailed information regarding the identity and coordination environment of a surface complex. However, they are unable to provide quantitative estimates regarding the

availability (in terms of concentration) of different surface sites (e.g., functional groups) where adsorption reactions may occur; in other words, the chemical reactivity of the surface in question. The latter, though, can be readily assessed by potentiometric titration, where the deprotonation of surface FGs can be quantified as a function of pH. To this data, concentrations and proton stability constants (also known as acidity constants, or K_a) of discrete surface FG sites may be fitted for bacterial (e.g., Fein et al., 1997; Cox et al.., 1999) and mineral surfaces (e.g., Kennedy et al., 2003; Smith and Ferris, 2003). It should be noted that a single so-called "discrete" site actually represents a mean of compounds that possess a similar FG. The result is a set of chemical parameters quantitatively describing a surface, which may be extrapolated to predict interactions between this surface and competing aqueous species in complex solutions, i.e., using surface complexation models (e.g., Fein et al., 2001).

One motivation for modelling microbial and mineral surface chemistry is that it has wide-ranging implications for solute sorption and biomineralization reactions. For instance, understanding the effectiveness of reactive surfaces in 'fixing' toxic metal cations from solution is vital in constructing accurate contaminant transport models, and ultimately designing effective bioremediation strategies (e.g., Bethke and Brady, 2000). Yet, this is where significant gaps in our current level of understanding exist. Microbial surface reactivity and solute sorption models have, to date, mostly been based on axenic laboratory cultures where cells are harvested at optimal growth conditions, the surface polymers (extracellular polysaccharides (EPS), sheaths, S-layers) may be chemically removed, and the cells may be acid-washed to strip off any cations previously adsorbed to their surfaces (e.g., Yee and Fein, 2001). Despite those studies resolving the capacity of biomass to sorb solutes from solution, they have not yet considered (1) the chemical reactivity of different species growing as part of a complex, mixed microbial community with cells in different growth phases held together by extracellular layers; and (2) the chemical or biological effects that natural, multi-element fluids might have on the charge characteristics of microbial surfaces. Furthermore, the adsorptive properties of microbes living in natural

systems is poorly understood, as separation of microbial and mineral components for individual investigation is fraught with difficulty. In fact, as far as we are aware, only the study of Kennedy et al. (2003) has examined natural mineral-microbe assemblages with the view of measuring the surface reactivity of the composites.

The goal of this preliminary study is to quantify and compare the sorptive properties of the individual microbial and mineral components in a natural microbial ecosystem. We selected geochemically diverse hydrothermal springs in Yellowstone National Park, USA on the basis of well-characterized biomass and the presence of highly reactive iron oxide minerals (HFO). Notably, these particular HFOs are known for their high arsenic content (Lagner et al., 2001; Inskeep et al., 2004), which approach experimental upper limits for arsenic content in synthetic HFO phases (Waychunas et al., 1993). We report functional group concentrations and proton stability constants for the surfaces of HFO from three different springs, and then compare the HFO from one of those springs to the biomass of thermophilic bacteria and algae collected from the same spring. We also measured the concentrations of solutes complexed to these surfaces, and for the HFO samples, applied a diffuse-layer surface complexation model (SCM) to evaluate the predictive ability of the reported surface parameters to describe the nature and extent of sorptive processes occurring on the mineral surface. In doing so, we highlight some of the advantages and disadvantages of applying surface chemical characterization techniques to natural samples that comprise mixtures of microbial and mineral components.

Previous Work at Study Area

The Hundred Springs Plain of Norris Basin (Figure 3-1A) contains a variety of geothermal springs. Some are classified as acid-sulfate-chloride (ASC), which are characterized by low pH, and typically contain high concentrations of reduced chemical species, including H_2, H_2S, As(III) and Fe(II), at discharge (Ball et al., 2002; Langner et al., 2001). Also found are neutral-chloride (NC) springs, which

have similar geochemistry, but higher pH. In this study, we sampled two ASC springs (Beowulf and Gap Spring) and one NC spring, Perpetual Spouter.

Of the three springs, Beowulf Spring has been the subject of recent aqueous, biological, and mineralogical investigations. It is home to microbial mat communities that vary compositionally with distance down the outflow channel (Figure 3-1B), correlating with major changes in temperature and aqueous/solid phase geochemistry (Langner et al., 2001; Inskeep et al., 2004). Those authors reported that vent waters contain abundant dissolved Fe(II) (49.3 μM, with a $Fe(II)/Fe_{total}$ ratio of 0.91 to 0.94), As(III) (23.9 μM), and H_2S (80 μM). The concentration of dissolved H_2S then declines to below 6 μM at 9 m, presumably due to a combination of degassing and oxidation, resulting in the precipitation of elemental sulfur (as determined by energy-dispersive spectroscopy; Langner et al., 2001) that ranges from amorphous to well-crystalline rhombohedral structures (Figure 3-1C; Figure 3-2A). In conjunction with filamentous microorganisms that form visible streamers, the solid-phase S° forms a yellow mat. Molecular analyses of the yellow mats demonstrated the presence of numerous *Hydrogenobaculum*-like populations, and that archaeal phylotypes were conspicuously absent at this location (Jackson et al., 2001). No As(III) oxidation was observed within the S° depositional zone (0–3 m), nor was any As(III) or As(V) sequestered within this zone. However, at downstream locations where H_2S is absent, microbial oxidation of As(III) to As(V) occurred at rates faster than ever reported for natural waters. These reactions are associated with an iron-depositing zone (Figure 3-1D), composed of an electron and X-ray amorphous HFO phase with 0.6–0.7 mole ratio As(V):Fe(III) (with arsenate, $H_2AsO_4^-$, adsorbed as a bidentate complex), amongst the highest As contents observed in naturally occurring HFOs (Morin et al., 2003; Inskeep et al., 2004). Close inspection of the HFOs revealed the presence of an extensive network of microorganisms (0.5 μm in diameter, and reminiscent in morphology to Fe(II)-oxidizing bacteria) with epicellular Fe(III) precipitates that suggest direct microbial templating of iron (Figure 3-2B; Inskeep et al., 2004). Numerous archaeal and bacterial species have been identified here, including those of the genera *Acidimicrobium*, *Thiomonas*, *Metallosphaera*, and *Marinithermus*;

several of these cultured relatives are known Fe(II) and/or As(III) oxidizers (Inskeep et al., 2004). Despite the apparent microbial diversity (Jackson et al., 2001; Inskeep et al., 2004) and SEM evidence of their iron-templating role (e.g., see Fig. 3-2B), the total organic carbon content of the HFO is only approximately 1% (Inskeep et al., 2004). The iron-depositing zone also contains *Hydrogenobaculum* populations. Donohoe-Christiansen et al. (2004) isolated an As(III)-oxidizing *Hydrogenobaculum* from a HFO-rich region in the ASC spring referred to Dragon Spring and showed that H_2S was a potent inhibitor of As(III) oxidation, suggesting the absence of As(III) oxidation activity in the yellow S°–rich mat zone may be due to the presence of high concentrations of H_2S.

High rates of As(III) oxidation were also observed in the adjacent green mats (Langner et al., 2001) (Figure 3-1D) that are characterized by a dense surface coverage of thermoacidophilic eukaryotic algae belonging to the order *Cyanidiales* (Seckbach, 1994). Interestingly, some portions of the green mats show significant concentrations of Fe and As, with elemental ratios identical to the HFOs.

3.2 Methods

3.2.1 Aqueous Sample Collection

Spring waters (25 mL) were obtained by syringe and filtered through 0.22 μm in-line nylon syringe filters. Waters from Gap Spring (Figure 3-1E) and Perpetual Spouter (Figure 3-1F) were collected 1 m from the outflow with temperatures of 83°C and 81°C, respectively. At Beowulf Spring there are two sources (designated 'W' and 'E'), which mix 4-5 m downstream. Waters at Beowulf were collected at locations corresponding to the position of the yellow S°-rich mats at Beowulf W (adjacent to the vent with temperature 55°C), and a further 5 m below the mixing zone in association with the green algal mats and the HFO that form a well-defined thermal gradient of 44-51°C (see Figure 3-1B, 1D). Samples were acidified by TraceMetal grade HNO_3, stored in ice for transport, and immediately refrigerated upon return to the laboratory at Montana State University. Spring temperature and pH were measured in the field using a digital thermometer and an Orion Ross (#8165BN) pH meter calibrated between 2 and 4 for ASC springs and 4 to 10 for the NC spring.

3.2.2 Solid Sample Collection

HFO samples from all three springs were obtained from submerged microbial Fe-encrusted terraced structures using a stainless steel scalpel. At Perpetual Spouter and Gap Spring, approximately 5 g of sample were obtained 1 m from the outflow. At Beowulf Spring, approximately 5 g of brown, HFO-mat composite was collected 5 m downstream from the mixing point of the West and East sources. In addition, at Beowulf, we sampled 1 g of the yellow, S°-rich mats found proximal to geothermal discharge in Beowulf West, and 1 g of green algal cells occupying the thermal gradient running parallel to the HFOs. All samples were stored in spring water for transport and refrigerated until analyses were complete within 48 hours of sampling.

3.2.3 Acid-Base Titration

All glassware and plasticware were acid-washed in ~30% v/v concentrated HCl for a minimum of 30 min, following which they were soaked in deionized water for a minimum of 2 hours. In an attempt to isolate microbial and mineral surfaces with minimal pH disturbance, samples were prepared at, and titrated from, the pH of the spring from which they were obtained. Samples from the two ASC springs (Beowulf, Gap) were prepared for titration by four alternating wash (10 second agitation followed by 10 minute soak) and harvest (centrifugation at 10,000 rpm for 10 minutes) cycles using ~40 ml of 0.01 M KNO_3 titration electrolyte adjusted to pH ~3 with concentrated TraceMetal grade HNO_3. The HFO from Perpetual Spouter (NC type) was similarly prepared at pH ~7, and was titrated up and down from pH 7 to obtain a complete dataset for surface characterization. ASC samples were titrated up from pH ~3 to pH 11; however, additional samples of green algae were instead washed at pH ~11 and titrated down to pH 3 to evaluate pH-dependent effects of the preparation procedure.

For each individual titration, 0.06 to 0.5 g dry weight of washed sample was suspended in ~50 ml of fresh titration electrolyte in a 125 ml titration flask equipped with a pre-calibrated Ross-type pH electrode (Mandel Scientific, Guelph, Ontario), thermocouple, magnetic stir bar, titrant dispenser and N_2 purge line. Titrations were performed at 23°C, either alkalimetrically to pH 11 with 0.01 M NaOH (Fisher Certified 0.01 M NaOH solution) or acidimetrically to pH 3 with 0.01 M HNO_3 prepared from TraceMetal grade HNO_3 and standardized against 0.01 M NaOH. A QC-Titrate autotitrator (Mandel Scientific) was interfaced to a personal computer and set to variably dispense titrant for increments of 0.1 pH units when electrode stabilities of 0.5 mV/sec were achieved. Suspensions were purged with N_2 gas for 30 min prior to, and throughout, the titrations. Electrode calibrations using commercial buffers of pH 3.0, 4.0, 7.0, 10.0, and 12.0 were performed between every set of titration replicates (3-5) representing a single sample, and all pH measurements were automatically temperature-corrected. To satisfy the selected electrode stability criteria, and cover the pH range of interest, each titration took approximately 50 min. Following titration, selected samples

were immediately titrated in the opposite direction to evaluate titration reversibility.

After the titrations, the sample material was collected by filtration onto pre-weighed 1.2 μm glass-fibre filters (GF/C #42, Whatman Inc, Florham park, NJ) and weighed after 7 days of air-drying in covered containers. This weight was subsequently used to normalize functional group concentrations; normalization on the basis of surface area was avoided because (1) surface area analysis by BET involves drying the sample, which may introduce additional error, especially with the biological samples, and (2) most studies on the surface reactivity of microorganisms report their results in terms of mass. In order to determine the concentrations of solutes sorbed under natural conditions, all solutions used for washing and titration were also filtered to 0.22 μm and then subsequently analyzed for selected aqueous species using a Quadrupole ICP-MS (Perkin Elmer Elan 6000, University of Alberta). Method detection limits were below 5 ppb for all elements, with relative standard deviations of less than 1.5% based on repeat standard analyses.

3.2.4 Discrete Site Modelling

In examining the titratible charges, three basic substrata were studied: HFOs, S°-rich mats, and green mats of *Cyanidia* cells. Due to the HFO encrustation of microbial cells in the iron-depositing zone, and the low organic C content (1%) of the HFO (recall Inskeep et al., 2004), titratable charges associated with those samples were assumed to be dominated by the mineral precipitates associated with the microbial community, and not from microbial cell surface functional groups themselves. The green mat samples, however, are dominated by *Cyanidia* algae, and so consequently, we expect cell surface FGs (i.e. amino acids, carboxylic acids, some hydroxyl groups) to be most important, and indeed, dominate, proton exchange reactions.

A pK_a spectrum approach was employed to model mineral and biological functional group concentrations; possible FG acidity constants (expressed herein as - log K_a, or pK_a) values are fixed in an interval (in this study 3–11, with increments

of 0.2) and FG concentrations are iteratively optimized across the pK_a spectrum by linear programming until the best fit to measured excess charge is achieved (Brassard et al., 1990). The charge balance of the system is first rearranged such that the surface charge arising from the deprotonation of discrete FGs may be expressed in terms of measured parameters (right hand side of equation (5)):

$$\sum_{j=1}^{n}[L_j^-] - [ANC] = Cb_i - Ca_i + [H^+]_i - [OH^-]_i \qquad (5)$$

where, for the i^{th} addition of titrant, Cb and Ca are the concentrations of base and acid, respectively; $[H^+]$ (and $[OH^-]$ by proxy) are monitored by the pH electrode; $[L_j^-]$ is the concentration of deprotonated FGs for the j^{th} monoprotic site of *n* possible sites set by the pK_a spectrum; and the acid-neutralizing capacity [ANC] is a constant offset representing the difference between FGs that remain protonated and those that deprotonate over the titration range (Smith and Ferris, 2001). By this arrangement, surface charge is assumed to arise solely from the deprotonation of FGs (left hand side of equation (5)), i.e., the surface charge at any given pH is equal to either side of equation (5). At the initial pH of titration, the concentration of base is set to zero, and the concentration of acid is assumed to equal $[H^+] - [OH^-]$, so that surface charge is zero at initiation. This formalism does not affect the spectrum of modelled FG sites; the ANC term serves as a constant surface charge offset accounting for the zero initial charge assumption, from which the modelled FG site distribution is independent. The assumption of zero surface charge at titration initiation simply facilitates the presentation of surface charge excess plots (see results).

FG concentration at each pK_a interval was fitted to the excess charge data by expressing the left hand side of equation 5 in terms of the both protonated and deprotonated (total) sites (L_{Tj}):

$$\sum_{j=1}^{n}\frac{K_{aj}[L_{Tj}]}{[H^+]_i + K_{aj}} - [ANC] = Cb_i - Ca_i + [H^+]_i - [OH^-]_i \qquad (6)$$

Fitting was performed with the computer program Matlab (version 6.5.1, The Mathworks, Inc., Natick, MA) by linear programming (Brassard et al., 1990), using a scripted implementation provided by D. Scott Smith (Wilfrid Laurier University).

The pK_a spectrum modelling approach ignores pH-dependent charging effects on proton stability constants, and thus all pK_a values reported here are apparent, rather than intrinsic. Apparent point of zero charge (PZC), the pH value where the concentration of protonated and deprotonated FGs is equivalent (i.e., surface charge is zero), was calculated for each sample by finding the concentration-weighted pK_a mean of discrete sites; it is important to note that FGs not detected over the modelled range (pH 4 – 10) may lead to a significant discrepancy between the apparent and "true" PZC. Diffuse-layer surface complexation modelling was applied to the three natural HFO surfaces using Visual MINTEQA2 (Gustafsson, 2000).

3.3 Results

3.3.1 Stream geochemistry

Analyses of the 3 springs indicate very similar chemistry (Table 3-1), with the exception of pH and Fe. Both locations sampled at Beowulf (E and W) and Gap Spring have a pH around 3, while Perpetual Spouter has a neutral pH. Iron concentrations are an order of magnitude greater in Gap Spring than in Perpetual Spouter, at 79.0 μM and 2.7 μM, respectively. The Fe concentrations measured at Beowulf lie between these two values, at 34.6 and 38.7 μM for 'W' and 'E' sources, respectively.

3.3.2 Bulk composition of HFOs

The HFOs from Beowulf Spring have been previously characterized utilizing a suite of microscopic and spectroscopic methods (Inskeep et al., 2004). Their high As content (As:Fe mole ratio = 0.62) is typical of other HFOs from acidic springs in Norris Geyser Basin, including the additional ASC spring used in this study, Gap Spring. Using XANES and EXAFS data, the same authors also concluded that arsenate is bound to Fe-octahedra via primarily bidentate binuclear surface complexes. The Fe cluster size was estimated to be only 40-80 atoms, based on complete surface coverage by arsenate. In contrast, the HFOs from Perpetual Spouter have a significantly different composition. First, the As content is very low, despite the fact that the aqueous arsenate concentration is higher than ASC spring waters (Table 3-1). Second, unlike the ASC HFOs, the HFOs found at Perpetual Spouter contain considerable Si; preliminary EDAX analyses show that the HFOs from the latter have a Si:Fe mole ratio of approximately 4.3:1 versus negligible Si content at Beowulf and Gap Spring (Inskeep, unpublished data). Further characterization of this phase is underway, and at this time it is difficult to ascertain relative contributions from particulate silicate mineral phases (e.g., quartz) versus authigenically precipitated amorphous silica versus HFO that has sorbed or co-precipitated significant amounts of silica. Given the high concentration of impurities, it is questionable as to whether or not the Fe-rich materials can actually be considered true HFO. It is not surprising that these natural

HFO-like precipitates contain significant As and Si, given the highly reactive nature of HFO. Previous studies have shown that 0.5 mole ratio arsenic contents are not inconsistent with HFO, based on HFO surface reactivity (see Inskeep et al., 2004 and references therein), and for the scope of this paper, we consider silica in the same context. Accordingly, in this study we employ the term "HFO" until a more appropriate one may be defined.

3.3.3 Surface elemental concentrations

Elements concentrated on surfaces were determined by analyzing solutes desorbed during wash and titration procedures. For all HFO and biomass samples, Mg is universally found at the highest surface concentrations (Table 3-2). In the case of the HFOs, the surface concentrations of Al, Rb, Cs, Li, Ca, Mn, Ba, Sr, and Zn are all at least an order of magnitude greater at Perpetual Spouter than the ASC springs, while the concentration of As is considerably less. In terms of biomass (both of which were from Beowulf), the green *Cyanidia* mats consistently released higher concentrations of analyzed elements than the yellow S°-rich mats.

These patterns are similarly reflected by concentration factors, which allow for a quick evaluation of how elements are partitioned between the aqueous and solid phases, with positive values indicating preferential accumulation on the solid relative to the effluent. For example, Mg was concentrated to the greatest extent by all samples (Figures 3-3 and 3-4). Furthermore, the HFO from Perpetual Spouter more strongly concentrated all elements than the ASC HFOs, with the exception of As and Cu (Figure 3-3). Interestingly, the HFOs from Beowulf and Gap Spring showed almost identical patterns, despite having formed from different spring waters. In comparison with HFO from Beowulf, the biomass samples (both yellow and green mats) from Beowulf typically display higher concentration factors, with the green mats showing the greatest sorptive capacity (Figure 3-4).

3.3.4 Substrate surface charge

Excess surface charge, as evaluated by right hand side of equation (5), and normalized to sample dry weight, is presented in Figure 3-5. At any given point, excess charge is equivalent to the cumulative surface concentration of deprotonated FGs, and the slope of the excess charge plot is the surface buffering capacity. For presentation purposes, excess surface charge plots were adjusted to zero at pH 4, and because the ANC term fitted by the pK_a spectrum modelling approach serves as a constant offset, the FGs modelled from titration data depend solely on the shape of the curve, and are thus independent of the apparent point of zero charge (see methods). All of the titration data is presented in Figure 3-5 for the qualitative comparison of charging behaviour between samples, and for a visual indication of titration repeatability. Also included in Figure 3-5 is the excess surface charge calculated from the set of FG concentrations that were fit to the measured excess surface charge data (i.e., from the left side of equation (5)), indicating the model goodness of fit for each replicate.

HFO obtained from the ASC springs (Beowulf and Gap Spring, Figure 3-5A, and 5B, respectively) show comparable pH-dependent charging behaviour, with increased buffering capacity towards higher pH, as previously noted for synthetic HFOs (Dzombak and Morel, 1990). In contrast, HFO from the NC spring, Perpetual Spouter (Figure 3-5C), displays charging behaviour that is largely static across the titration range, and the increased buffering capacity is noticeably absent until pH ~10. In other words, while the charging behaviour of HFO from ASC springs indicates relatively significant concentrations of FGs that deprotonate at circumneutral pH, the HFO from the NC spring indicates a lack of such sites. Discrete site modelling (discussed below) enables the quantification and direct comparison of such differences that are only visually inferred from excess charge data.

Excess charge plots representing Beowulf biomass are shown in Figure 3-5D. The yellow mats display low reactivity over the entire titration range. In contrast, the green mats display significant surface reactivity, and similar to HFO samples from ASC springs, show increased buffering capacity at alkaline pH. It is critical to

note that the green mat samples were split and prepared in two different ways: (1) the curves labelled 'green mat' correspond to samples that were rinsed at spring pH and ionic strength to examine the surfaces under conditions as close as possible to their *in-situ* state, while (2) the 'base-washed' green mat samples were washed at alkaline pH to release any surface-complexed elements, and accordingly, better reflect surface charging inherent to the native microbial surface. 'Base-washed' green mat samples display charge profiles that are largely consistent with their unwashed counterparts at low pH, but display relatively increased reactivity at higher pH. In fact, sharp inflection in the former's excess charge curves at pH ~7 indicate a high concentration of sites with apparent pK_a values around 7.

3.3.5 Discrete site modelling

FG distributions for the HFO samples, modelled from the excess charge curves presented above, and composited over all replicates, are presented in Figure 3-6. The HFOs from ASC springs (Beowulf and Gap, Figure 3-6A and 6B, respectively) show FGs that are broadly consistent in pK_a distribution (e.g., four main sites) and in the relative concentrations of sites. Conversely, the HFOs from Perpetual Spouter show a FG distribution that is noticeably different; although it too has four main sites, they are noticeably less important at high pH, and the dominant site is an apparently acidic FG, suggestive of an apparent point of zero charge <7 (Figure 3-6C).

FG distributions for microbial substrata are presented in Figure 3-7. The yellow mats show a low density of FGs (note different y-axis increments), with a more or less scattered distribution, and for this reason assignment of individual types of FGs was not attempted (Figure 3-7A). Unwashed green mats (Figure 3-7B) show three FGs of approximately equal concentration, and a fourth, more acidic type of lesser concentration. Base-washed green mats (Figure 3-7C) show FG types 1, 3, and 4 that are largely consistent with acid-washed counterparts in both pK_a and concentration; however, the concentration of FG type 2 is increased ~8 fold, most likely by the desorption of surface complexes as a consequence of the base-washing procedure (see discussion).

We also evaluated the reversibility of protonation/deprotonation reactions for green-mat samples in order to ensure that cells were not irreversibly altered (i.e., by cell lysis) at high pH. We did so by titrating unwashed samples from pH 11 to 3 immediately following their titration from pH 3 to 11, without changing the titration electrolyte (and thus retaining all metals that may have hydrolysed and desorbed during the up titration). Presented in Figure 3-8 is an example excess surface charge plot for up and down titrations of the same green mat sample (Figure 3-8A), as well as the sites modelled independently from 'up' titration (Figure 3-8B) and 'down' titration (Figure 3-8C) data. Both titration directions show similar pH-dependent charging profiles, and the slightly decreased reactivity during 'down' titration may be attributable, in part, to decreased sensitivity introduced by dilution of the titration suspension as a consequence of titrant previously added during 'up' titration. Nonetheless, it is evident from Figure 3-8 that deprotonation/protonation reactions were largely reversible by the methods utilized herein, and that cell lysis was not likely responsible for the changes observed after the base-washing of green mat samples.

FG parameters for all samples are summarized along with estimates of error in Table 3-3. For HFO samples, total FG concentrations were assessed as the sum of sites 1 and 2 combined with the average of sites 3 and 4, as we assume the latter represents the stepwise deprotonation of iron oxide surface sites (i.e., $>FeOH_2^+ \rightarrow >FeOH \rightarrow >FeO^-$, where ">" denotes the parent compound). The HFO samples from ASC springs show elevated total site concentrations (5.44 mmol g^{-1} and 4.63 mmol g^{-1} for Beowulf and Gap springs, respectively) relative to the Perpetual Spouter HFO (2.16 mmol g^{-1}). They also contain abundant FGs with high pK_a values, while the Perpetual Spouter HFO is deficient in such sites; correspondingly, the ASC HFOs are characterized by high apparent point of zero charge (PZC) values (7.59 and 7.87 for Beowulf and Gap Spring, respectively), while the Perpetual Spouter shows a lower apparent PZC of 6.21. The biomass samples also showed high apparent PZC values (ranging from 7.25 to 7.87), but varied considerably in their total FG concentration. For instance, the yellow mat possesses a low total FG concentration of 0.52 mmol g^{-1}, while the green mat had an order of

magnitude more FGs (5.59 mmol g^{-1}), which more than doubles (to 12.30 mmol g^{-1}) as the result of the base-washing procedure. As was mentioned in the methods, we define apparent PZC as the mean of FG pK_a values weighted by their concentration (apparent PZC, see Table 3-3), as compared to a true PZC, which is defined as the pH where surface charge is zero. The difference herein lies in the fact that we could not measure FGs of extreme pK_a, as well as FGs that may have retained adsorbed surface complexes throughout titration. This explains the discrepancy between previous studies showing PZC values of microbial cell surfaces between 2 and 4 (Harden and Harris, 1953) and our results.

3.4 Discussion

3.4.1 HFO surface reactivity

HFOs from both ASC springs (Beowulf and Gap) are characterized by an abundance of FGs at pK_a 7 and 9, ascribed to the first and second stepwise deprotonation of iron-oxyhydroxide hydroxyl groups. Actually, these HFOs closely mimic pure synthetic HFO with respect to FG site concentrations, pK_a distribution (Smith and Ferris, 2001), and high PZC (e.g., 8.8, Sverjensky and Sahai, 1996). In contrast, the NC spring (Perpetual Spouter) HFO is largely dominated by a low pK_a FG (4.1) and correspondingly, has a lower apparent PZC of 6.2. Although we cannot be absolutely confident as to why differences in apparent PZC exist between the HFOs from ASC and NC springs, the most noticeable difference in HFO composition is the amount of silica associated with these solids. For example, HFOs from Beowulf and Gap Spring have low to undetectable silica contents, whereas the HFOs from Perpetual Spouter contain up to 78% SiO_2 by weight (Inskeep, personal communication). Silica incorporation into HFO is important because previous studies have shown that it effectively lowers the PZC to values between 5-7 (Schwertmann and Fechter, 1974). Thus far, no studies that we are aware have described the characteristics of silica-rich HFO in terms of FG site distribution, but we find that in the NC system, HFO hydroxyl site concentrations are considerably lower, presumably as a result of solid phase silica (detrital quartz or authigenic amorphous silica) "diluting" the concentration of the available HFO sites, or alternatively, dissolved silica reacting with Fe resulting in HFO surface sites whose chemical nature is distinct from the individual components. Although all springs investigated possess similar dissolved silica concentrations (recall Table 3-1), the fact that protons appear to inhibit the polymerization of silica (Fournier, 1985), and at low pH, amorphous silica has a more neutral surface charge (PZC ~2; Parks, 1965), may better explain the absence of silica in the ASC HFOs than an absence of detrital silica. In the case of HFO material from the ASC spring Beowulf where bulk compositional data is available, low Al (<1%) and Ti (<300 ppm) concentrations (Inskeep et al., 2004) suggest a predominately authigenic origin.

The PZC of the HFOs have an important bearing on sorption reactions taking place at the mineral-water interface. HFOs from the ASC springs are in equilibrium with waters at pH <3, and consequently, an apparent PZC of 7.6-7.9 means that their surfaces will remain positively-charged. This facilitates the electrostatic adsorption and surface complexation of dissolved anions. In the ASC springs, arsenate ($H_2AsO_4^-$) is highly concentrated by the HFOs as the result of edge and corner sharing bidentate binuclear and bidentate mononuclear As(V) complexation to hydroxyl groups of Fe(III) (Inskeep et al., 2004). However, Fe(III) hydroxyl FGs with pK_a 7-9 are noticeably absent for HFO from Perpetual Spouter. The apparent PZC of these HFO surfaces is 6.2, less than the pH of the waters to which these surfaces are exposed (7.0). Unlike the ASC HFOs, the NC HFO surfaces will be negatively charged, and indeed, they are more reactive to dissolved cations (see Table 3-2). For example, Al, Ba, Ca, Cs, Li, Mn, Sr, Rb, and Zn are found in concentrations that are an order of magnitude higher than on the ASC HFO. Conversely, the concentration of arsenate is an order of magnitude lower than on ASC HFO surfaces. These results clearly demonstrate the importance of surface chemical functional groups, and the surface charge they confer, for solute adsorption in these hydrothermal systems.

3.4.2 Microbial surface reactivity

Surface reactivity varies considerably between the two different microbial communities associated with Beowulf Spring. SEM images show the yellow mat consists of filamentous microorganisms within a matrix of amorphous and rhombohedral S° (Langner et al., 2001; Macur et al., 2004). Our results indicate that the yellow mats have a surface reactivity (0.52 mmol g^{-1} summed over the titration range) that is comparable to previously reported values for thermophilic bacteria (e.g., 0.85 mmol g^{-1}, Burnett et al., 2006), but lower than values reported for mesophilic bacterial cultures (averaging 3.2 ± 1.0 mmol g^{-1}, after Borrok et al., 2006, and assuming a 10:1 wet-to-dry weight ratio for the purposes of comparison). The lower surface reactivity of the yellow mats may be due to (i) an inherent quality of thermophilic cell surfaces; (ii) the low reactivity of elemental

sulfur during titration; and/or (iii) possibly a relatively high weight ratio of EPS to cells. In the case of the latter scenario, EPS may not contribute excess charge within our titration range as it can be dominated by hydrated polysaccharides rich in hydroxyl functional groups that deprotonate at pH values greater than 10 (Liu and Fang, 2002).

Green mats sampled at Beowulf are dominated by *Cyanidia* algae (Jackson et al. 2001). Unlike other samples, surface properties of the green mats were determined by titration following two different preparation procedures; (1) rinsing at stream pH and ionic strength to leave natural sorbates intact on the algal surfaces, and (2) washing at pH 11 to strip the sorbates and better reveal native FGs on the cell surfaces. Our results show that both unwashed and washed FG concentrations (5.59 mmol g^{-1} and 12.30 mmol g^{-1} dry weight, respectively; Table 3-2) are not only higher than the yellow mats, but they are also higher than total FG concentrations determined for other eukaryotes; e.g. the alga *Pseudokirchneirella subcapitata* (~0.4 mmol g^{-1} dry weight from pH 3 to 10, Kaulbach et al., 2005) and the fungus *Saccharomyces cerevisiae* (~1.4 mmol g^{-1}, Naeem et al., 2006) (note: we assume a wet to dry weight ratio of 10:1 for the purpose of these comparisons). Indeed, our values are considerably higher than previously reported for any microbial surface. With that said, our samples likely contain a heterogeneous mixture of intact cells, cellular debris, and cells that lysed during wash at pH 11; the latter two would expose additional FGs not associated with cell surface layers.

Unlike most bacteria that possess an abundance of FGs with low pK_a (generally attributed to carboxyl groups; e.g., Beveridge and Murray, 1980; Jiang et al., 2004), such FGs are found in low concentration for *Cyanidia* (Figure 3-7B and 7C). Instead, the algal surfaces appear dominated by FGs with pK_a values above 5, leading to an apparently high PZC. Based on the organic acid protonation constants from Martell and Smith (1989), we attribute site 1 to carboxyl groups, site 2 to phosphate groups, site 3 to phosphate or amino groups, and site 4 to amino groups. It is interesting that sites 1, 3, and 4 remained unchanged by the washing procedure; not only does this imply that they represent organic surface sites, but that any elements released into solution during the titration of unwashed samples

had a negligible effect on modelled FG site concentrations (Figure 3-7A vs. 7B). By comparison, there was a nearly ~5 fold increase in the concentration of site 2 as the result of the pH 11 washing procedure.

The washing procedure also resulted in the desorption of a range of elements, in particular Mg and As (see Table 3-2). The changes in site 2 and the release of Mg and As suggests that these elements were bound to that FG. Certainly, the concentration of site 2 FGs that were revealed by washing can more than quantitatively account for the whole of Mg and As adsorption. The association of Mg with cell surfaces may not be unsurprising given that previous findings have shown that Gram-positive bacteria utilize it to cross link phosphate residues associated with teichoic acid molecules, and in doing so, eliminate the repulsive anionic charges between adjacent molecules, giving rise to more dense but stable structures (Doyle et al., 1974). In Gram-negative bacteria, calcium functions in a similar manner, bridging adjacent molecules of LPS together and anchoring the outer membrane to the underlying peptidoglycan layer (Ferris and Beveridge, 1986). At present, information regarding *Cyanidia* surface ultrastructure is insufficient for us to conclude with any level of certainty whether the adsorbed Mg here serves a similar function. With regards to As, its association is unexpected because of its anionic nature. Although the FG responsible for As(V) sorption may have a pK_a that lies outside of the titration range, it is also possible that Mg serves as a cation bridge between phosphate FGs and arsenic oxyanions. In fact, magnesium oxides and hydroxides have been patented for use in As(V) sequestration from drinking water supplies (United States Patent 6821434). Additional spectroscopic methods, as described above, would be required to confirm the nature of the algal As(V) surface complexes.

3.4.3 Surface complexation modelling

The main goal of this study was to evaluate and compare the natural surface reactivity of hydrothermal HFOs and microbial communities. The surface chemical data presented herein is directly applicable to surface complexation models designed to account for ion sorptive behaviour as a function of temperature, ionic

strength, and sorbent to sorbate ratio. These models predict adsorption equilibrium by considering the formation of surface complexes to be governed by mass-action equations. Additionally, surfaces that are charged possess electrical potential gradients that may strongly influence sorption reactions by the energy required to move ions against those gradients, and the various surface complexation models (e.g., constant capacitance, triple-layer, etc.) differ in the mathematical representation of these electrical potential gradients. For example, the diffuse-layer model presupposes that all adsorbed ions occupy the same surface plane, and that the charge associated with that surface is balanced by charge associated with aqueous counter ions positioned in a diffuse layer that forms the boundary between the surface and the aqueous phase. The energy associated with moving an ion from the bulk solution to the surface, with or against the electrical potential gradient, is accounted for by a change in apparent ion activity, as determined by an exponential Boltzmann expression:

$$(X_s^z) = (X^z)[e^{-\psi F / RT}]^z \qquad (8)$$

where the surface activity (X_s^z) of ion X with charge z is related to the activity of X in solution (X^z) by the unitless Boltzmann factor $e^{-\psi F / RT}$ considering surface potential (ψ) , Faraday constant (F), ideal gas constant (R), and absolute temperature (T) (Langmuir, 1997).

These models require prior knowledge of all potential surface complexes, their intrinsic stability constants, and chemical and electrical parameters describing the surface of interest. At present, there is a paucity of stability constants describing metal sorption to microbial surfaces, although methods have been proposed to extrapolate microbial surface stability constants from stability constants describing aqueous complexation between elements and analogous organic acids (Fein et al., 2001). Fortuitously, many proton and metal stability constants have been previously determined for HFO surface FGs, and surface complexation models have extensively applied to synthetic HFO surfaces (Dzombak and Morel, 1990). In this study, we use our experimentally determined

surface chemical parameters, along with literature metal-HFO stability constants, to test the ability of the SCM to describe metal sequestration by natural HFOs.

In order to apply a diffuse-layer SCM, several important assumptions regarding the nature of our HFO samples were required:

(i) For modelling purposes, and as discussed previously, FG types 3 and 4 represent the stepwise deprotonation of $>FeOH_2^+$; thus the concentration of iron surface sites were taken as an average of FG types 3 and 4, and their intrinsic proton stability constants were replaced in the Visual MINTEQA2 HFO sorption database by their apparent proton stability constants determined in this study by titration.

(ii) FG types 1 and 2 correspond to surface moieties of an Fe-As oxyhydroxide, and their apparent proton stability constants were assumed to represent the deprotonation from >(Fe,As)OH to $>(Fe,As)O^-$. No data exists pertaining to sorption reactions involving such ligands, and for modelling purposes, the stability constants of surface complexes compiled for HFO were assigned to these putative species. As discussed below, these FGs must be accounted for in order to explain the observed elemental partitioning to the As-rich HFO surfaces.

(iii) The relative concentration of surface FGs vs. solutes is very low on a per-litre basis in all hydrothermal springs investigated. This assumption allows for consideration of the rapidly moving stream water with which the HFO surfaces are in contact; as stream water is in contact with a given surface for only a short period, the adsorption of ions to the HFO surface should not deplete their aqueous concentration in stream water. In other words, to avoid the depletion of solutes in our model, we assume that a rapidly flowing stream is equivalent to a large volume of water with which the HFO surface is in contact. As long as this assumption is valid, other competing sorbents (such as bacteria, algae, other mineral phases, DOC, etc.) will also have negligible effect on stream water composition, and thus may be considered as systems separate to that of the HFO-water interface.

(iv) The surface area of the HFO is similar to that of synthetic HFO (600 m^2/g, Rodin et al., 2003), and that there existed no difference in surface area between the various HFO samples. We consider this assumption a potentially large source of error; however, due to the solid nature of the HFO mats and the homogenization required for analysis, independent assessments of mineral surface area were not possible.

The predicted and measured surface concentrations of various ions for all three HFOs are presented in Figure 3-9 (note that cesium, lithium, and rubidium species could not be considered in the model due to a lack of thermodynamic data describing their affinity for the HFO surface). The plots are organized such that (1) surface FG site concentrations that are under-predicted by the model are found at the left hand side, (2) the surface FG site concentrations that are over-predicted by the model are found on the right hand side, and (3) the best fit is found about the center.

The HFOs from the ASC springs, Beowulf and Gap Spring (Figure 3-9A and 9B, respectively) show similar predicted and measured surface FG concentrations. In both cases, the sorption of As is well accounted for by the surface properties of the HFOs, as determined by discrete site modelling; the sorption of arsenate is predicted to occur onto positively charged $>FeOH_2^+$ sites (represented by FG types 3 and 4 in Figure 3-6), and these sites, being fully protonated at stream pH in both ASC springs, do not contribute to the sorption of cationic species. Meanwhile, the adsorption of cations is dependent on assumption 2, that the sites of lower pK_a (FG types 1 and 2, Figure 3-6) deprotonate from a neutral state to a negative one, and consequently, a small proportion (predicted from pK_a and concentration data by SCM) will remain deprotonated at the low stream pH and present negatively charged reactive sites for the sorption of cations. Accordingly, surface complexation modelling predicts that FG types 1 and 2 are responsible for the bulk of cation complexation. The breakdown of the model in Figure 3-9A and 9B on either side of arsenic can be attributed to the differences in the previously determined affinity of synthetic HFO sites and the true affinity of Fe-As

oxyhydroxide sites for available cations. Therefore, assumption 2, whereby such FGs are presumed to have a similar affinity for aqueous cations as HFO sites, is invalid. The model thus demonstrates that while the As-rich HFOs from ASC springs possess $>FeOH_2^+$ surface FGs that fully account for the adsorption of arsenic, the presumed Fe-As sites differ in affinity for aqueous cations, with Al, Zn, Mg, Ba, and Sr having a higher affinity for a fully deprotonated Fe-As site than a fully deprotonated FeO^- site, and for B, Mn, Cu, and Ca, the reverse is true.

In the case of the NC spring, the above assumptions become even less valid; Perpetual Spouter has abundant silica in the solid phase, and as a result, the concentration of surface FGs that may be compared with synthetic HFO (such as types 3 and 4 in the case of ASC springs) is noticeably reduced. The sorption of arsenic should occur with strong preference to $>FeOH_2^+$ sites, as exemplified in Figures 9A and 9B. However, in the case of Perpetual Spouter, arsenic is the surface species most over predicted by SCM (Figure 3-9C). The predicted surface arsenic concentration is calculated using the concentration of Fe sites as determined by titration, and the Fe sites presumed to be present on the HFO from Perpetual Spouter should have bound more arsenic than was measured there. Unlike ASC springs, where discrepancies were solely attributed to the different affinities of cations to Fe and (Fe,As) surface sites, the deviation of Perpetual Spouter from the model likely results from the significant presence of silica, although some FG sites attributable to silica may fall outside of the titration range and therefore cannot be included in SCM. As discussed above, silica will serve to lower the PZC of the solid from Perpetual Spouter (see section 3.4.1) and electrostatically inhibit the sorption of arsenic, as appears to be the case with the HFO samples. Similarly, surface complexes of Mg (as well as Al and Zn) that are under-predicted by the model have a high affinity for silica, and although they are undetectable by titration, silica surface sites also possibly account for the sorptive behaviour of these dissolved species.

Finally, although the adsorption of metals occurred while the substrates were submerged at temperatures ranging from ~80 to ~50 °C, depending on the spring, modelling was performed using functional group concentrations, proton stability

constants, and literature thermodynamic data based on 25°C. Although the temperature dependence of proton adsorption may be minimal in the case of microbial surfaces (Wightman et al., 2001), and metal adsorption slightly more dependant on temperature (Gorman-Lewis et al., 2006), the effect of temperature on HFO protonation and metal sorption could not be tested at present with the SCM employed here.

3.5 Conclusion

In ASC springs, HFO and green *Cyanidia* algae have similar overall reactivity, and display comparable elemental sorption patterns, despite possessing FGs that differ in chemical composition, site concentration, and pK_a distribution, whereas yellow S^0-encrusted mats possess significantly lower overall reactivity. These findings highlight the fact that sorptive properties may vary between different microbial populations in close proximity. We also show that HFO from a NC spring bound significantly more cations, but less arsenic, than ASC HFOs, a pattern coincident with a lower apparent PZC and a high solid-phase silica content. The additional application of diffuse-layer surface complexation modelling to the HFO samples suggests that iron-arsenic oxyhydroxide (ASC springs) or silica (NC springs) sites are responsible for the majority of cation adsorption at such low pH conditions. Overall, these results highlight the importance of chemical parameters, such as surface functional group concentrations and pK_a distributions, in accounting for complex sorption phenomena. While surface complexation modelling could, at present, only be applied to the HFO samples, it is assumed that a similar approach may eventually be achieved for microbial biomass, and ultimately, facilitate a better understanding of the microbial role in elemental partitioning in natural systems.

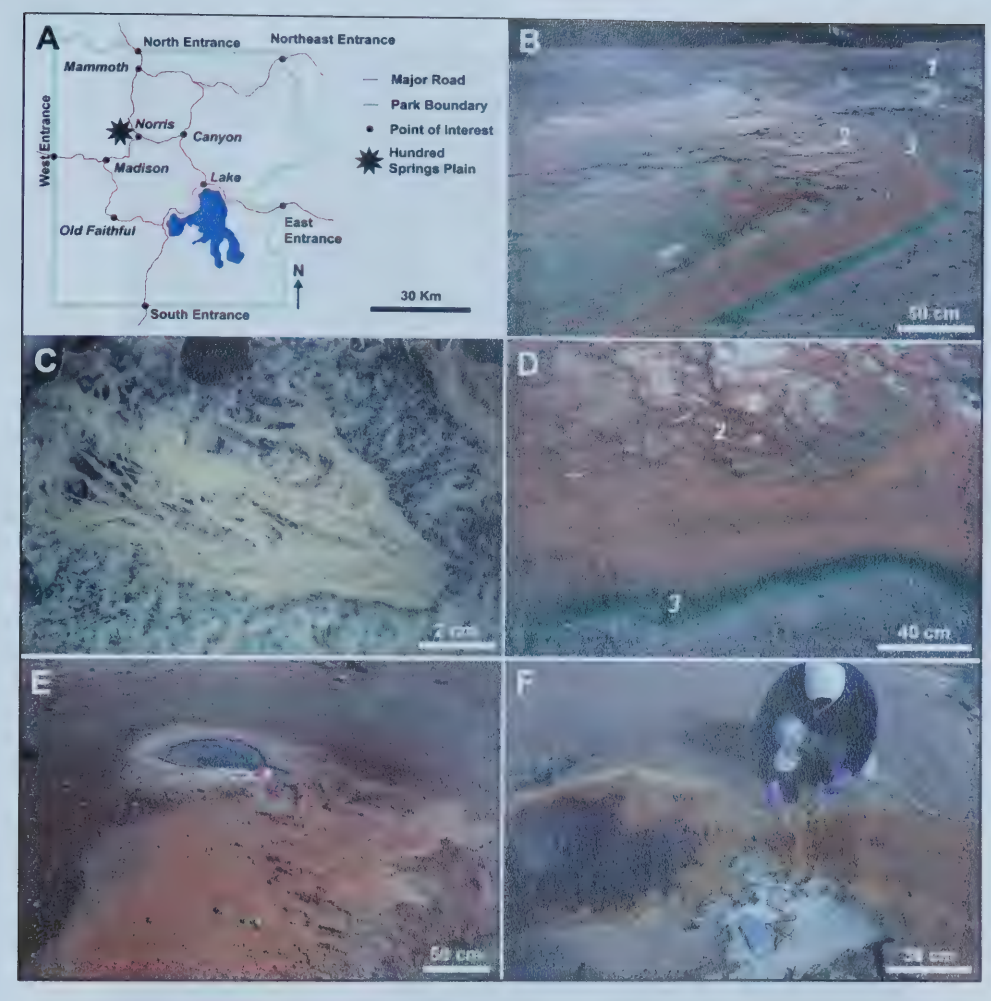

Figure 3-1. (A) Map of sampling locations in Norris Geyser Basin, YNP. (B) Overview of Beowulf Spring, with close up of (C) 'yellow mat' (labelled 1 in (B)) consisting of thermophilic, filamentous bacteria and elemental sulfur precipitates and (D) the sharp transition zone between the HFO (label 2) and the green mat of *Cyanidia* algae (label 3). (E) Gap spring, where terraced HFO mats accumulate within the outflow surrounding the vent. (F) Perpetual Spouter, similarly showing HFO deposition within the outflow channel.

Figure 3-2. Scanning electron micrographs (SEM) of filamentous microorganisms from Beowulf Spring associated with S^0–rich mats (A) or encrusted with high As-rich, hydrous ferric oxide (HFO) precipitates (B). SEM image of Fe-encrusted cells (see arrow). See Langner et al. (2001) and Inskeep et al. (2004) for SEM procedures.

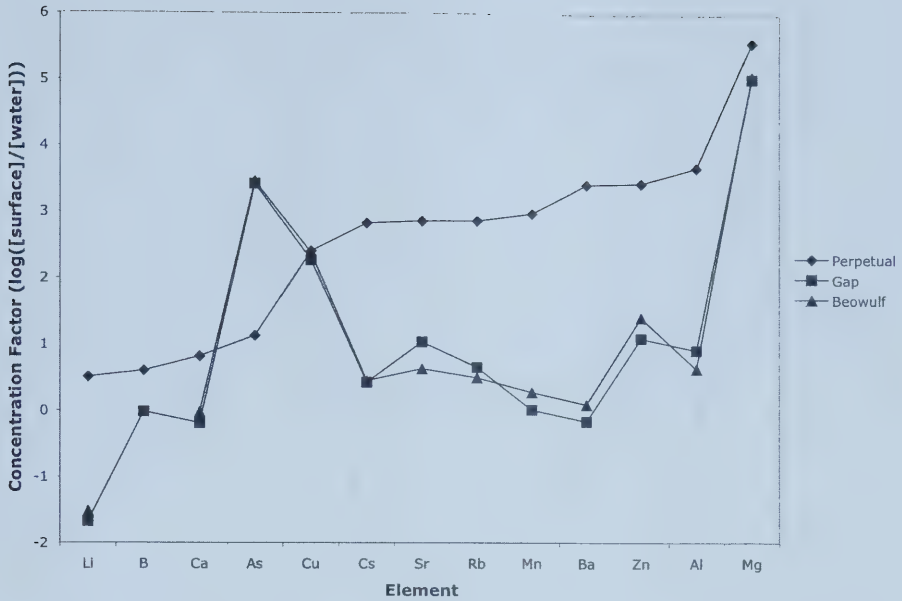

Figure 3-3. Elemental concentration factors for HFO surfaces relative to spring water (log ([surface]/[stream]) from three different springs.

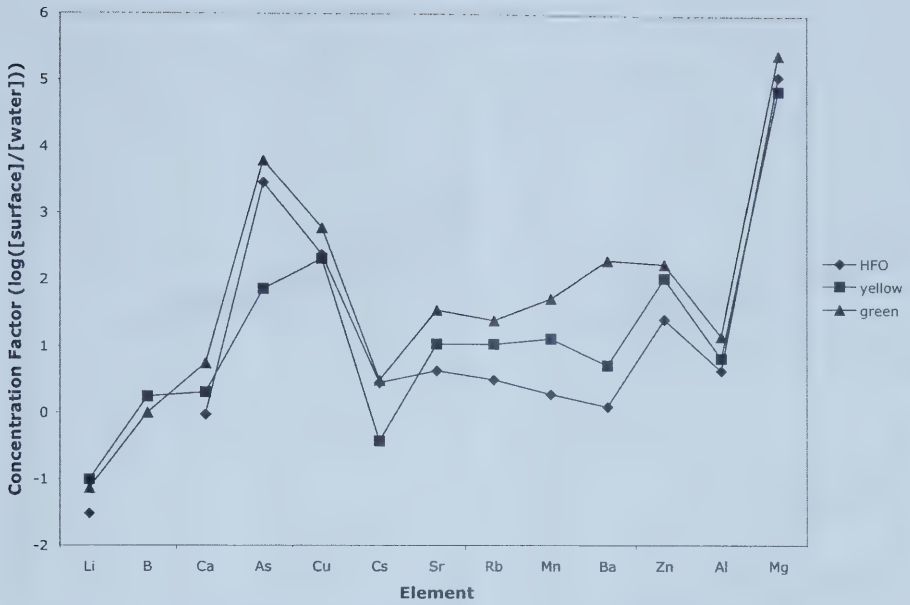

Figure 3-4. Elemental concentration factors for HFO surfaces relative to spring water (log [surface]/[stream]) for the sampling sites within Beowulf Spring.

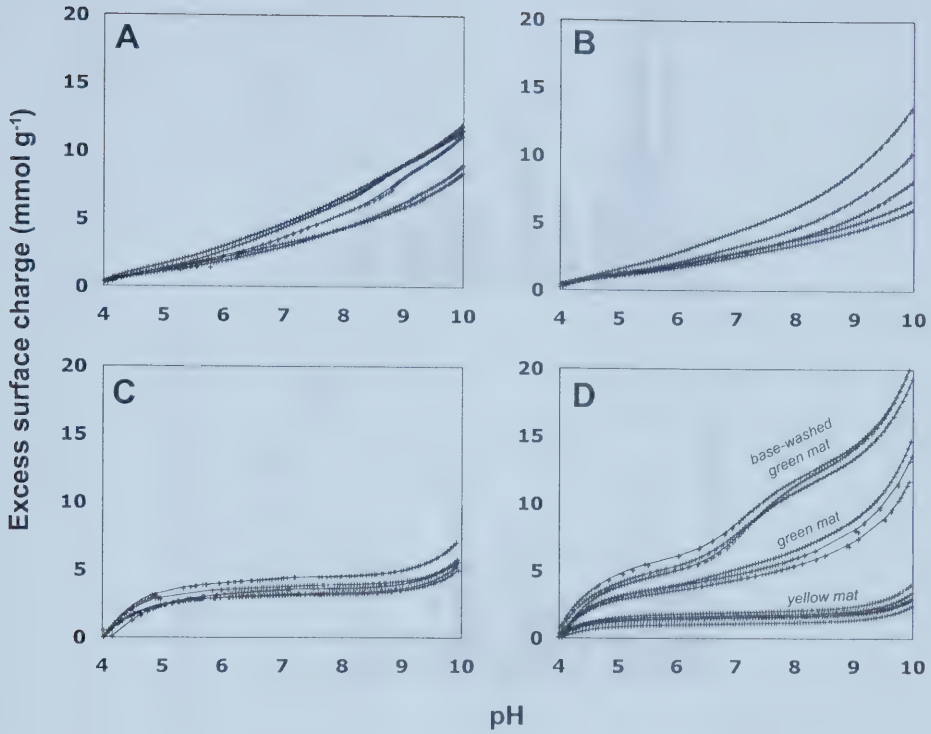

Figure 3-5. Plots of excess surface charge associated with HFO samples from: (A) Beowulf Spring; (B) Gap Spring; (C) Perpetual Spouter; and (D) samples of the yellow S^0–rich and the green *Cyanidia* mats from Beowulf Spring. All replicates are plotted together (n=3 or n=5). Data points represent excess charge data measured during titration and solid lines represent the excess charge calculated to arise from the set of functional groups modelled after each titration (the model goodness-of-fit).

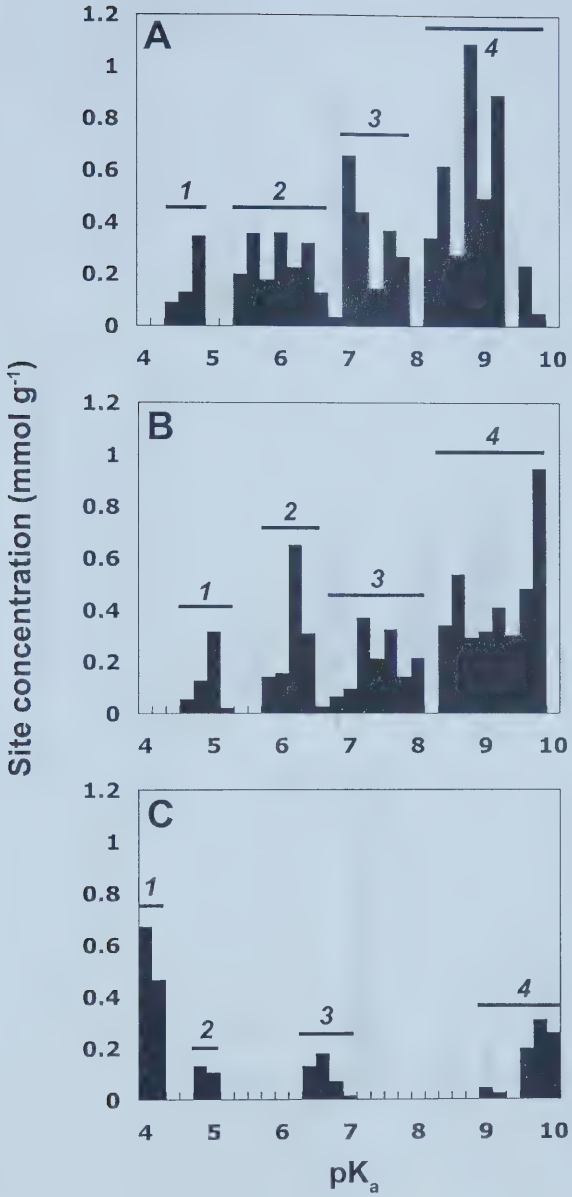

Figure 3-6. Modelled functional group (FG) distributions for HFO samples: (A) Beowulf Spring, (B) Gap Spring, and (C) Perpetual Spouter. For this composite plot, FG concentrations were summed over all five replicates at each pK_a interval and then normalized to total weight titrated. Individual surface FG types are identified by number for summary in Table 3-3.

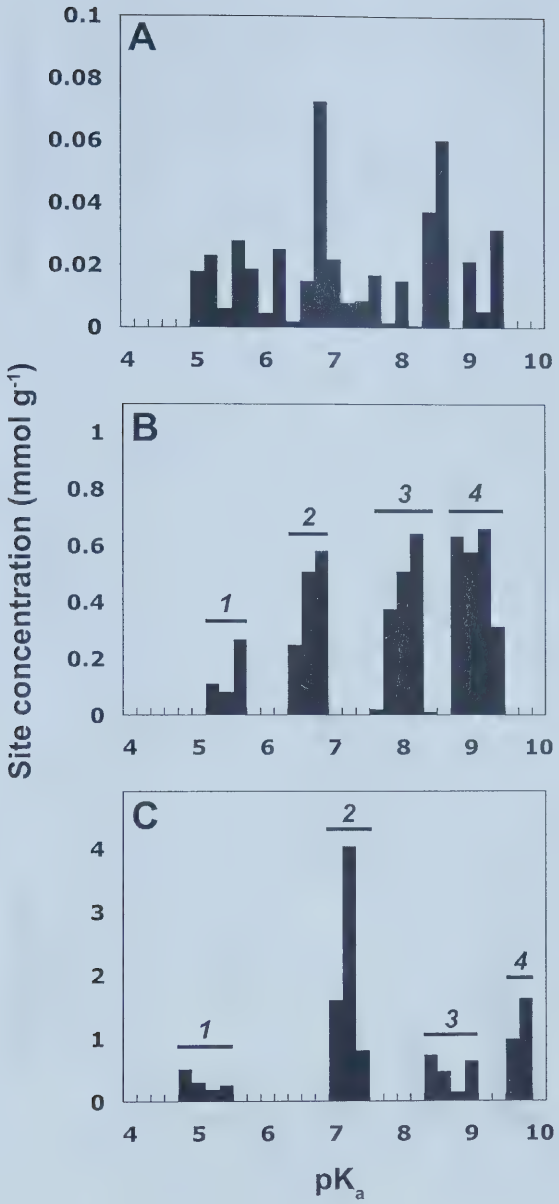

Figure 3-7. Modelled functional group distribution for other microbial mat samples from Beowulf Spring: (A) green mat, (B) base-washed green mat, and (C) yellow mat. For this composite plot, FG site concentrations were summed over all five replicates at each pK_a interval and then normalized to total weight titrated. Individual surface FG types are identified by number for summary in Table 3-3.

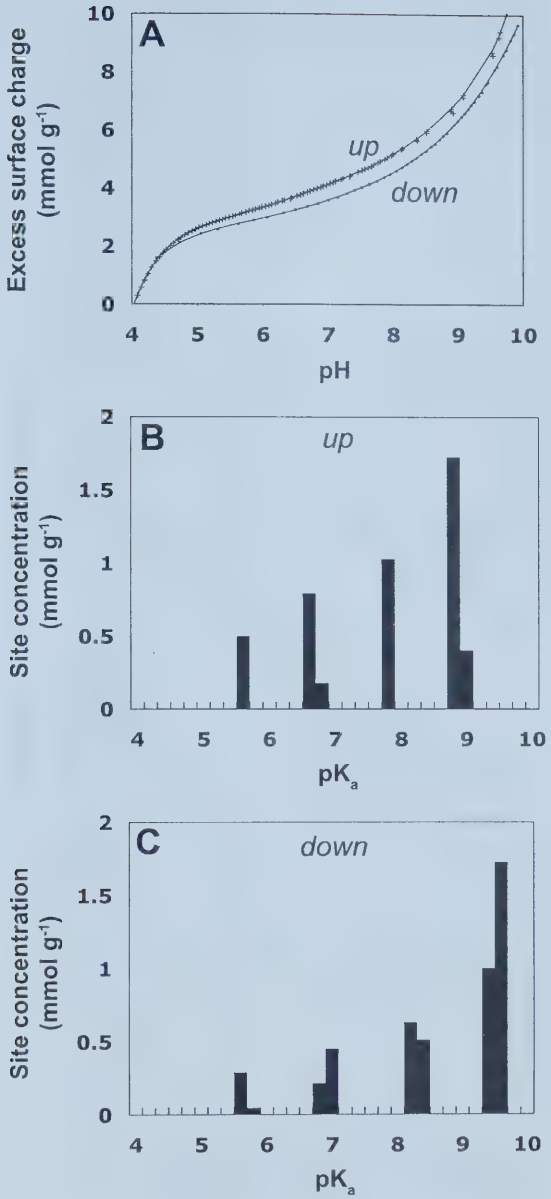

Figure 3-8. Evaluating the reversibility of protonation/deprotonation reactions by reverse titration. (A) Surface charge plot showing reverse titration, where this sample (green mat from Beowulf Spring) was titrated up from 3 to 11, and then immediately back down to 3. The modeled site distributions for (B) up titration and (C) down titration show model sensitivity, as well as an indication of the data obtained from the modeling of a single titration.

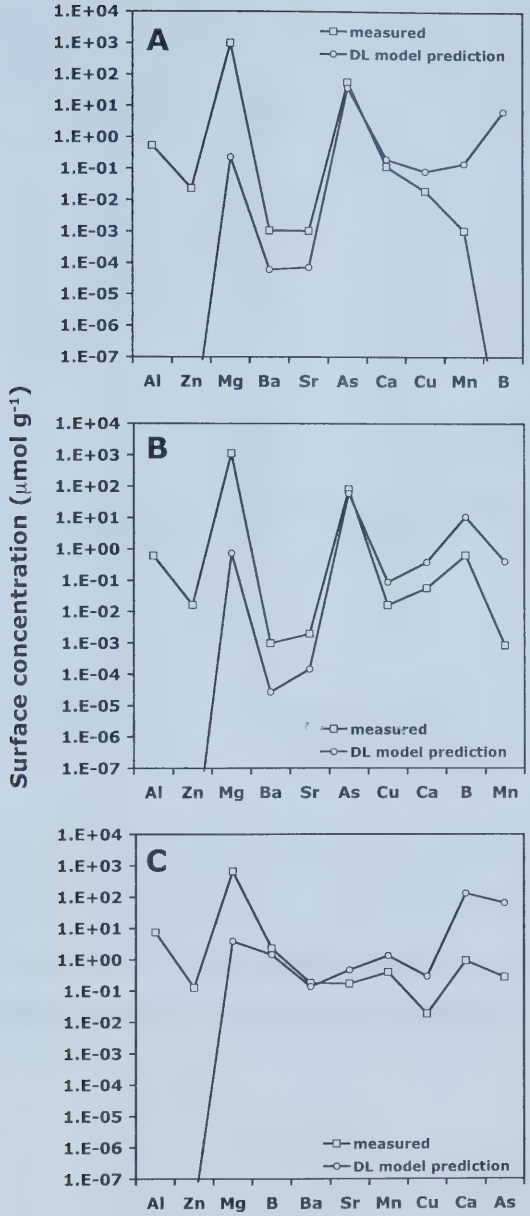

Figure 3-9. Measured surface ion concentrations associated with HFOs compared to those predicted by diffuse-layer surface complexation modelling. Elements are ordered according to their degree of under- or over-prediction. (A) Beowulf Spring, (B) Gap Spring, and (C) Perpetual Spouter Spring.

Analyte ($\mu mol\ L^{-1}$)	Spring			
	Perpetual Spouter	Gap Spring	Beowulf West	Beowulf East
pH	7.0	3.3	3.0	3.1
Temp (°C)	83.6	81	52.5	67
Na	19762.5	11759.1	11572.1	11135.8
Si*	5100	5300	4700	4700
K	1411.8	1028.2	1240.5	1225.1
B	1132.2	657.6	644.6	640.6
Li	944.3	454.0	544.4	537.4
Ca	274.8	87.4	127.9	124.5
As	40.4	30.2	18.7	19.6
Rb	5.7	2.9	3.8	3.8
Cs	4.7	2.0	2.7	2.6
Mg	3.4	10.3	8.5	8.2
Al	3.1	73.6	125.9	123.7
Fe	2.7	79.0	34.6	38.7
($nmol\ L^{-1}$)	Perpetual	Gap	Beowulf W	Beowulf E
Mn	805	810	564	546
Sr	457	182	242	239
Ba	134	1410	847	841
Be	91	208	114	124
Cu	142	88	82	82
Se	148	93	95	93
Zn	90	1297	455	873

Table 3-1. Values for pH, temperature and concentration of various elements (μM or nM) in aqueous samples taken at the same locations of solid phase samples. *concentrations from Inskeep (determined at Montana State University). See methods for instrumental detection limits and reproducibility.

Analyte (μmol g^{-1})	Perpetual HFO	Gap HFO	Beowulf HFO	Beowulf YLW	Beowulf GRN
Mg	1300.5	1124.8	981.3	623.2	2111.6
Fe	N/A	N/A	N/A	0.6	4.0
Al	14.8	0.6	0.5	0.8	1.8
As	0.5	79.8	56.7	1.4	121.1
(nmol g^{-1})	Perpetual	Gap	Beowulf HFO	Beowulf YLW	Beowulf GRN
B	4508	630	<500	1130	2880
Rb	4219	13	12	41	93
Cs	3187	5	7	1	8
Li	3006	10	16	54	40
Ca	1799	56	118	258	687
Mn	766	1	1	7	29
Ba	356	1	1	4	168
Sr	332	2	1	3	8
Zn	251	16	23	49	152
Cu	36	16	19	17	49

Table 3-2. Concentration of elements (μmol or nmol g^{-1} dry weight) desorbed from hydrous ferric oxide (HFO) and microbial samples. The last column is the difference in elements desorbed during titration of washed and unwashed *Cyanidia* mat material. Note: Iron concentrations are considered not applicable for HFO washing fluids.

	pK_a					Concentration (mmol/g)				
	site 1	site 2	site 3	site 4	Apparent PZC	site 1	site 2	site 3	site 4	total
HFO Beowulf	4.61±0.17	5.96±0.23	7.34±0.29	8.86±0.15	7.59±0.12	0.58±0.37	1.83±0.31	1.92±0.44	4.14±1.08	5.44±0.92
HFO Gap Spring	4.98±0.12	6.21±0.03	7.45±0.07	9.27±0.20	7.87±0.33	0.57±0.19	1.40±0.47	1.51±0.38	3.80±1.54	4.63±1.24
HFO Perpetual Spouter	4.10±0.04	5.20±0.57	6.59±0.14	9.63±0.30	6.21±1.76	1.33±2.60	0.21±0.29	0.41±0.14	0.84±0.45	2.16±2.39
Synthetic HFO	4.78±0.34	5.73±0.50	7.32±0.44	8.75±0.37	nd	0.34	0.37	0.30	1.06	2.42
green mat	5.43±0.24	6.65±0.03	8.00±0.23	9.03±0.24	7.87±0.29	0.46±0.09	1.37±0.65	1.59±0.59	2.17±0.88	5.59±0.98
base-washed green mat	5.11±0.32	7.17±0.10	8.64±0.33	9.65±0.17	7.72±0.20	1.27±0.56	6.46±0.89	2.00±0.45	2.57±2.55	12.30±1.94
yellow mat	nd	nd	nd	nd	7.25±0.40	nd	nd	nd	nd	0.52±0.13

Table 3-3. Individual functional group pK_a values and concentrations for all samples investigated. Uncertainty is given as 2 standard error (p=0.05) where available. Apparent PZC represents the pK_a value where the modelled concentration of sites is equal on both sides of the pK_a spectrum. Note that for HFO sites, the total concentration depends on presumed site identities (see text). Synthetic HFO data (sites 2 through 5 only) from Smith and Ferris (2001).

3.6 References

Ball, J.W., McCleskey, R.B., Nordstrom, D.K., Holloway, J.M, and Verplanck, P.L. (2002) *Water-chemistry data for selected springs, geysers, and streams in Yellowstone National Park, Wyoming 1999–2000.* Boulder, CO, USA: United States Geological Survey Open File Report 02-382.

Bayer, M.E. and Sloyer Jr., J.L. (1990) The electrophoretic mobility of gram-negative and gram-positive bacteria: an electrokinetic analysis. *J Gen Microbiol* **136:** 867-874.

Bethke, C.M. and Brady, P.V. (2000) How the Kd approach undermines ground water cleanup. *Ground Water* **38:** 435-443.

Beveridge, T.J. and Murray, R.G.E. (1976) Uptake and retention of metals by cell walls of *Bacillus subtilis*. *J Bacteriol* **127:** 1502-1518.

Brassard, P., Kramer, J.R., and Collins, P.V. (1990) Binding site analysis using linear programming. *Environ Sci Technol* **24:** 195-201.

Cox, J.S., Smith, D.S., Warren, L.A., and Ferris, F.G. (1999) Characterizing heterogeneous bacterial surface functional groups using discrete affinity spectra for proton binding. *Environ Sci Technol* **33:** 4514-4521.

Davis, J.A. and Kent, D.B. (1990) Surface complexation modeling in aqueous geochemistry. In *Reviews in Mineralogy Vol 23: Interface Geochemistry*. Hochella, M.F. and White, A.F. (eds). Washington, DC, USA: Mineralogical Society of America, pp. 177-248.

Donahoe-Christiansen, J., Jackson, C.R., D'Imperio, S., Inskeep, W.P., and McDermott, T.R. (2004) Arsenite-oxidizing *Hydrogenobaculum* sp. isolated from an acid-sulfate-chloride geothermal spring in Yellowstone National Park. *Appl Environ Microbiol* **70:** 1865-1868.

Doyle, R.J., McDannel, M.L., Streips, U.N., Birdsell, D.C., and Young, F.E. (1974) Polyelectrolyte nature of bacterial teichoic acids. *J Bacteriol* **118:** 606-615.

Dzombak, D.A. and Morel, F.M.M. (1990) *Surface Complexation Modeling. Hydrous Ferric Oxide*. New York, NY, USA: John Wiley and Sons.

Fein, J.B., Daughney, C.J., Yee, N., and Davis, T.A. (1997) A chemical equilibrium model for metal adsorption onto bacterial surfaces. *Geochim Cosmochim Acta* **61:** 3319-3328.

Fein, J.B., Martin, A.M., and Wightman, P.G. 2001. Metal adsorption onto bacterial surfaces: Development of a predictive approach. Geochimica et Cosmochimica Acta, 65:4267-4273.

Ferris, F.G. and Beveridge, T.J. (1986) Physiochemical roles of soluble metal cations in the outer membrane of *Escherichia coli* K-12. *Can J Microbiol* **32:** 594-601.

Fournier, R.O. (1985) The behaviour of silica in hydrothermal solutions. In: Geology and Geochemistry of Epithermal Systems (eds Berger BR, Bethke PM). Reviews in Economic Geology 2:45–61.

Gorman-Lewis, D., Fein, J.B., and Jensen, M.P. (2006) Enthalpies and entropies of proton and cadmium adsorption onto *Bacillus subtilis* bacterial cells from calorimetric measurements. *Geochim Cosmochim Acta* **70**: 4862-4873.

Gustafsson, J.P. (2000) Visual Minteq [WWW document]. URL http://www.lwr.kth.se/English/OurSoftware/vminteq/ (verified 13 March 2006).

Harden, V.P and Harris, J.O. (1953) The isoelectric point of bacterial cells. *J. Bacteriol* **65**: 198-202.

Hunt, S. (1986) Diversity of biopolymer structure and its potential for ion-binding applications. In *Immobilisation of Ions by Bio-Sorption*. Eccles, H. and Hunt, S. (eds). Chichester, UK: Ellis Harwood, pp. 15-46.

Inskeep, W.P., Macur, R.E., Harrison, G., and Bostick, B.C. (2004) Biomineralization of As(V)-hydrous ferric oxyhydroxide in microbial mats of an acid-sulfate-chloride geothermal spring, Yellowstone National Park. *Geochim Cosmochim Acta* **68:** 3141-3155.

Jackson, C.R., Langner, H.W., Donahoe-Christiansen, J., Inskeep, W.P., and McDermott, T.R. (2001) Molecular analysis of microbial community structure in an arsenite-oxidizing acidic thermal spring. *Environ Microbiol* **3:** 532-542.

Jiang, W., Saxena, A., Bongkeun, S., Ward, B.B., Beveridge, T.J., and Myneni, S.C.B. (2004) Elucidation of functional groups on Gram-positive and Gram-negative bacterial surfaces using infrared spectroscopy. *Langmuir* **20:** 11433-11442.

Kaulbach, E.M., Szymanowski, J.E.S., and Fein, J.B. 2005. Surface complexation modelling of proton and Cd adsorption onto an algal cell wall. *Environ Sci Technol* **39**: 4060-4065.

Kennedy, C.B., Martinez, R.E., Scott, S.D., and Ferris, F.G. (2003) Surface chemistry and reactivity of bacteriogenic iron oxides from Axial Volcano, Juan de Fuca Ridge, north-east Pacific Ocean. *Geobiology* **1:** 59-70.

Konhauser, K.O. (1998) Diversity of bacterial iron mineralization. *Earth Sci Rev* **43:** 91-121.

Konhauser, K.O. (2007) *Introduction to Geomicrobiology*. Oxford, UK: Blackwell Publishing.

Langner, H.W., Jackson, C.R., McDermott, T.R., and Inskeep, W.P. (2001) Rapid oxidation of arsenite in a hot spring ecosystem, Yellowstone National Park. *Environ Sci Technol* **35:** 3302-3309.

Langmuir, D. (1997) *Aqueous Environmental Geochemistry*. New Jersey, NJ, USA: Prentice Hall.

Liu, H. and Fang H.P. (2002) Characterization of electrostatic binding sites of extracellular polymers by linear programming analysis of titration data. *Biotechnol Bioeng* **80:** 806-811.

Macur, R.E., Langner, W.H., Kocar, B.D., and Inskeep, W.P. 2004. Linking geochemical processes with microbial community analysis: successional dynamics in an arsenic-rich, acid-sulphate-chloride geothermal spring. *Geobiology* **2:** 163-177.

Martell, A.E. and Smith, R.M. (1989) *Critical Stability Constants*. New Jersey, NJ, USA: Plenum Press.

Morin, G., Juillot, F., Casiot, C., Bruneel, O., Personné, J.C., Elbaz-Poulichet, F., et al. (2003) Bacterial formation of tooeleite and mixed arsenic (III) or arsenic (V) – iron (III) gels in the Carnoulès acid mine drainage in France: a XANES, XRD, and SEM study. *Environ Sci Technol* **37:** 1705–1712.

Naeem, A., Woertz, J.R., and Fein J.B. 2006. Experimental measurement of proton, Cd, Pb, Sr, and Zn adsorption onto the fungal species Saccharomyces Cerevisiae. *Environ Sci Technol* **40**: 5724-5729.

Roden, E.E. (2003) Fe(III) oxide reactivity toward biological versus chemical reduction. *Environ Sci Technol* **37:** 1319-1324.

Schwertmann, U. and Fechter, H. (1982) The point of zero charge of natural and synthetic ferrihydrites and its relation to adsorbed silicate. *Clay Miner* **17:** 471–476.

Seckbach, J. (1994) The natural history of *Cyanidium* (Geitler 1933): past and present perspectives. In *Evolutionary Pathways and Enigmatic Algae: Cyanidium caldarium (Rhodophyta) and Related Cells.* Seckbach, J. (ed). The Netherlands: Kluwer Academic Publishers, pp. 99-112.

Smith, D.S., and Ferris, F.G. (2001) Proton binding by hydrous ferric oxide and aluminium oxide surfaces interpreted using fully optimized continuous pKa spectra. *Environ Sci Technol* **35:** 4637-4642.

Smith, D.S. and Ferris, F.G. (2003) Specific surface chemical interactions between hydrous ferric oxide and iron reducing bacteria determined using pK spectra. *J Colloid Interface Sci* **266:** 60-67.

Sverjensky, D.A. and Sahai, N. (1996) Theoretical prediction of single-site surface-protonation equilibrium constants for oxides and silicates in water. *Geochim Cosmochim Acta* **60:** 3773-3797.

Waychunas, G.A., Rea, B.A., Fuller, C.C., and Davis, J.A. (1993) Surface chemistry of ferrihydrite: Part 1. EXAFS studies on the geometry of coprecipitated and adsorbed arsenate. *Geochim Cosmochim Acta* **57:** 2251-2269.

Wightman, P.G., Fein, J.B., Wesolowski, D.J., Phelps, T.J., Benezeth, P., and Palmer, D.A. (2001) Measurement of bacterial surface protonation constants for two species at elevated temperatures. *Geochim Cosmochim Acta* **65**: 3657-3669.

Yee, N. and Fein, J.B. (2001) Cd adsorption onto bacterial surfaces: A universal adsorption edge? *Geochim Cosmochim Acta* **65:** 2037-2042.

CHAPTER 4

Investigating the Geochemical Impact of Burrowing Animals: Proton and Cadmium Adsorption onto the Mucus Lining of Terebellid Polychaete Worms[1]

4.1 Introduction

Estuaries are the depositional interface between fluvial- and marine-waters. Estuarine settings are also widely regarded as sediment sinks that trap land-derived detritus and tidally delivered sands. Concomitant with sediment transport is the arrival of dissolved ions from fluvial and marine water sources. The juxtaposition of fine-grained sediments (i.e. silts and clays), metal ions, and rapid changes in water temperature, salinity, and chemistry due to mixing, leads to the accumulation of metals at the seafloor. The amount of accumulated metals will depend on several processes, including: (1) the composition of the sediment; (2) transport of metals from the bulk ocean water to sediment porewaters; (3) transformation of metals (e.g. methylation, hydrolysis, oxidation-reduction); (4) competition between sediment minerals and organic phases for metals; and (5) the influence of bioturbation on these processes (Bryan and Langston, 1992).

The distribution of metals in estuarine settings is reasonably well studied. This is due to a number of reasons, including the economic use of estuaries for shellfish harvesting (e.g. Willapa Bay, Chesapeake Bay, Prince Edward Island) and the common occurrence of industry along fluvial inputs to estuaries (e.g. Benoit et al., 1994; Chiffoleau et al., 1994; Millward and Glegg, 1997). Traditionally, studies have focused on the partitioning of metals into fine-grained sediment and on the enrichment of metals in animals resulting from bioaccumulation (e.g. Bryan and Hummerstone, 1973; Bryan et al., 1983; Luoma et al., 1998). One commonly overlooked component in these types of studies is the presence of organic coatings

[1]A version of this chapter has been published. Lalonde SV, Dafoe LT, Pemberton SG, Gingras MK, and Konhauser KO. *Chemical Geology* **271**, 44-51 (2010).

produced by burrowing organisms that are prevalent along the sediment-water interface.

A variety of worms are known to thrive in estuarine settings, including polychaetes, nemerteans and hemichordates. Indeed, worm-like organisms represent one of the most important group of macroscopic, bioturbating animals in marginal-marine settings; more than 10,000 species of marine polychaetes have been identified in settings ranging from the intertidal through to the continental shelf (Rouse and Fauchald, 1997). Estuarine worms are diverse as well, and are represented by the Subclass Palpata and the families Glyceridae, Nephtyidae, Nereididae, Serpulidae, Sabellidae, Spionidae, Pectinariidae, and Terebellidae. Worms within these families are generally capable of binding sediment with mucous excretions that serve to physically support burrow walls, prevent desiccation, and function as nutrient-rich organic substrates that foster microbial symbiosis within the burrow lining (e.g., Aller and Aller, 1986).

The presence of mucous linings at the sediment-water interface likely plays an important role in ion complexation and mineral nucleation reactions due to the presence of highly reactive surface adsorption sites typical of organic matter. It is well known that the surfaces of organic matter in natural systems, including bacterial, fungal, and eukaryotic cells, as well as natural organic matter (dissolved and particulate phases), possess functional group ligands that are anionic at seawater pH and are capable of binding metal cations and nucleating mineral phases (c.f. Konhauser 2007 and references therein). While previous work has demonstrated significant enrichment of metals (Al, Cu, Fe, Mn, Ni, Zn, up to 4X enrichment) in burrow walls relative to unburrowed sediment (Over et al., 1990), as well as selective mineralization and concretion formation in relict burrows (Zorn, 2007), a complete understanding of processes influencing the accumulation of metals in estuarine sediments must also include the adsorptive role of macrofaunal mucous material.

In this study, we incubated the terebellid polychaete *Thelepus crispus* for the purposes of isolating its mucous burrow lining for chemical characterization both in terms of composition and surface adsorptive behavior. The latter was

assessed by potentiometric titration and metal adsorption experiments. We employ Cd to evaluate metal-ligand stability constants for several reasons: (1) Cd remains soluble over the pH range of interest, (2) to facilitate comparison with other metal adsorption studies involving fulvic/humic acids and bacteria; and (3) for its relevance to near-shore ocean and estuary waters where Cd concentrations may be elevated as the result of industrial input. All titration and Cd adsorption experiments are performed near seawater salinity (using 0.5M NaCl) to best provide applicability to marine systems. The results are modeled within a surface complexation framework that permits the extrapolation of our experimentally-derived thermodynamic constants to systems that vary considerably in terms of pH, ionic strength, and temperature. We demonstrate through this approach that metal adsorption onto worm mucus (1) can be accounted for by surface complexation modeling that takes into account adsorptive ligand properties and metal-ligand stability constants and (2) appears to differ from bacterial surfaces and other organic matter by an abundance of highly-chalcophile thiol functional groups.

4.2 Methods

4.2.1 Mucus Procurement

Thelepus crispus terebellid worms were collected by Westwind sealab supply (Victoria, BC) and stored in cold seawater during overnight shipment to the University of Alberta. Worms were segregated into polycarbonate containers with lids and walls that were perforated by hand drill to promote water circulation, and the containers were submerged in a continuously circulating salt-water tank at 4 to 8 °C for 15 days. Three different substrates were explored for promoting burrow formation: (1) worms were placed on 100 mesh acid-washed quartz sand (Sigma-Aldrich Canada, Oakville, Ontario), (2) worms were individually placed within 15 mm glass test tubes (Fisher Scientific, Ottawa, Ontario), and (3) worms were individually placed within sections of PVC tubing (1/2 inch inner diameter, Fisher Scientific, Ottawa, Ontario) that were sealed at one end with cheesecloth. With the exception of attempts using quartz sand, the polycarbonate containers in which the worms were segregated contained no mineral or organic detritus (e.g., Fig4-1B). Only the PVC tubing promoted burrow formation; in each instance, the worm lined the PVC tubing with mucous material, and in some cases, the worm exited the open end of the tubing, extending the burrow well beyond the length of tubing (see Figure 1) and into the free space available in the submerged and capped polycarbonate container. After 15 days, the PVC tubes containing mucous-lined burrows were collected. For each, the PVC tubing was split by sterile scalpel, and the mucous burrow linings were easily separated from the PVC with tweezers. It is interesting to note that all worms constructing burrows under the experimental conditions imported material from the surrounding salt-water tank by extending tentacles through the small (~5 mm diameter) water circulation holes drilled in the polycarbonate containers. The resulting mucous lining had incorporated within it sand grains, shell fragments and organic matter from the surrounding tank, as well as brown fecal matter generated by the worms themselves. The mucous material was cleaned vigorously several times by rinsing under a stream of ultrapure water with the use of forceps and spatula to physically remove any detritus not washed

away by water. After all visible foreign matter had been removed, mucous samples were stored in ultrapure water at 4 °C until later use.

4.2.2 Mucus compositional analysis

Subsamples of mucous material were incubated in 0.01M HCl for 30 minutes to remove any carbonate components, rinsed 3 times with ultrapure water, and lyophilized for further analysis. Major element composition (C,H,N,S) was determined using a Carlo Erba EA 1108 elemental analyzer. Weight percent nitrogen was used as an estimate of protein content (crude protein (CP) = N x 6.25) (Maynard and Loosli, 1969). Carbohydrate and fatty acid compositions of lyophilized samples were determined after separate acid and organic solvent extractions, respectively, by gas chromatography (Varian 3400 gas chromatograph with flame ionization detector) at the Human Nutrition Research Unit, University of Alberta. FTIR spectra were collected from 650 to 4000 cm^{-1}, at 0.5 cm^{-1} resolution, using a Nicolet Magna 750 FTIR spectrometer connected to a Nic-plan FTIR microscope operating in absorbance mode in the Department of Chemistry Analytical and Instrumentation Laboratory, University of Alberta. Sixty four scans of air-dried samples on a KCl plate were combined to obtain the final spectra, with scans of the clean KCl plate prior to mucous addition used for background correction.

4.2.3 Acid-base titration and Cd adsorption

All glassware and plasticware was acid-washed for >12 hours in a 30% v/v HCl bath, rinsed three times with ultrapure water, soaked in an ultrapure water bath for >24 hours, rinsed again three times, and dried prior to use. The preparation of all solutions was done gravimetrically on an analytical balance. Mucous material was rinsed three times in ~ 50 ml of 0.5M NaCl, resuspended in ~ 30 ml of 0.5M NaCl in wide-mouth pyrex beakers (for final mucus concentrations of 0.75 – 0.9 dry g/L), and acidified to pH ~3 with 2M HCl. A double-junction glass pH electrode (Orion ROSS ultra, filled with 3M KCl) was calibrated using commercial pH buffers (Thermo Fisher Scientific, Waltham, MA; pH 2, 4, 7, 10, 12) that had been

adjusted to 0.5M NaCl by the addition of NaCl salt, and added to the flask along with a Teflon stir bar, gas bubbler, thermocouple, and titrant dispenser. The flask was then sealed with Parafilm™ and purged with N_2 for 30 min prior to titration, and throughout titration. Titrations were performed using a computer-controlled PC-Titrate auto-titrator (Mandel Scientific, Guelph, Ontario) set to deliver 0.01 ± 0.00005 M NaOH (commercial titrant, Thermo Fisher Scientific, Waltham, MA) in increments of 10 additions per pH unit, from pH 3 to 11, with stability criteria of 0.5 mV/sec between additions. NaOH titrant was purged for 30 min with N_2 prior to titration, each titration lasted approximately 1 h, with sample temperature remaining approximately constant (23 ± 1 °C) throughout all titrations. Several samples were first acid-washed for 30 min in 0.01 M HCl to remove any carbonate components prior to preparation and titration, although this acid-washing step had no discernable effect (data not shown). After titration, mucous material was filtered onto 1.2 μm Whatman GF/C filters and air-dried to constant mass.

Mucous material for Cd adsorption experiments was washed in 0.5 M NaCl as above, but suspended in a magnetically stirred 0.5 M NaCl solution containing 5 ppm Cd (prepared from a 1000 ppm Cd commercial AAS standard, Fisher Scientific) that had been acidified to pH 2.0 - 2.5 with 2 M HCl. Due to the limited amount of mucous material available, Cd adsorption experiments were run in a serial fashion, rather than a batch fashion. Briefly, after an equilibration time of 30 min, an aliquot of ~10 ml of the mucous-bearing Cd solution was removed by syringe, filtered to 0.22 μm using nylon membrane filters, and acidified with trace-metal grade HNO_3 for analysis by flame-AAS (Perkin Elmer 3000, Department of Chemical Engineering, University of Alberta). Method detection limit was <0.01 ppm Cd using matrix-matched standards. After sampling, the pH of the experiment was adjusted up by one pH unit using 2 M NaOH, and the process was repeated until pH ~11 was achieved. The adsorption experiment was performed twice (the second time with a consistent pH offset of 0.5), and the results were combined for a single adsorption isotherm. Cd adsorption blanks were not run simultaneously, but have previously indicated negligible adsorption to the experimental apparatus (data not shown). Chemical equilibrium modeling of Cd speciation in experimental

solutions was performed using visual MINTEQ (Gustafsson, 2009) using specific ion interaction theory (SIT) activity correction for high ionic strength as implemented by Pettit et al. (2006) and with stability constants from the MINTEQA2 v4.0 database (Allison et al., 1991).

4.3 Results and Discussion

The *Thelepus* worms (Figure 4-1A) generated copious amounts of mucous material when placed in open-ended sections of PVC tubing and submerged in a circulating salt water tank at 4-8 °C for 15 days (Figure 4-1B and C). The worms failed to create mucous material when placed on pure quartz sand or in round-bottom glass test tubes (data not shown). In the construction of their mucus-lined PVC domiciles, the worms used their palps to gather material from outside their restricted area of the salt-water tank, and added this material to the mucous matrix.

4.3.1 Composition of Mucous Lining

The results of compositional analysis (CHNS, carbohydrates, and lipids) are presented in Table 4-1. Considering that mucous glycoproteins consist of a protein core to which carbohydrate moieties are attached, the abundance of protein (~ 20 wt%) relative to carbohydrate (~5%) is not surprising. Lipids form only a minor constituent of the mucous material. With regards to the elemental analysis, of particular note is the presence of sulfur, which is consistent with the high abundance of thiol-conferring cysteine residues that characterize mucous glycoproteins (Leitner et al., 2003).

FTIR spectra of the mucous material (Figure 4-2A) indicates a predominance of glycoprotein and shows strong spectral similarity with isolated mucins from across the animal kingdom. From right to left, strong organic functional group absorption peaks can be tentatively assigned to complex sugar C-O stretching and S=O stretching (1070 cm^{-1}), S=O stretching (1180 cm^{-1}), CH_2 scissoring (1448 cm^{-1}), N-H bending (amide II) (1543 cm^{-1}), N-C=O stretching (amide I) (1656 cm^{-1}), and various C-H stretching modes (2851 and 2926 cm^{-1}) (Brandenburg and Seydel, 1996; Bavington et al., 2004). In particular, strong absorbance by both S=O and and complex sugar C-O stretching at 1070 cm^{-1}, combined with strong adsorption at amide I and II, are considered specific to glycoproteins (but also glycosamineglycans; Brandenburg and Seydel, 1996; Bavington et al., 2004). Comparison with FTIR spectra obtained for a variety of isolated animal mucin, and echinoderm mucous material in particular, reveals striking similarities that strongly

point to a predominance of the glycoprotein mucin in the terebellid burrow lining. The strong spectral similarity likely stems from the well conserved and broadly distributed nature of the mucin family of glycoproteins that appear to dominate these materials (Bavington et al., 2004; Lang et al., 2007). Of the three echinoderm mucins investigated by Bavington et al. (2004), the FTIR spectra of partially purified mucin from the brittlestar *Ophiocomina nigra* provided a nearly identical match to the terebellid mucous material (Figure 4-2B, reproduced from Bavington et al. (2004)). Spectra representing two other echinoderm species, *M. glacialis* and *P. pulvillus*, as well as spectra for bovine mucin, porcine mucin, bovine aggrecan, heparin, chondroitin-4-sulfate, dermatan sulfate, and hyaluronic acid all show adsorption features that are broadly consistent with the terebellid mucus, as well as with each other, highlighting the common organic functional groups comprising these diverse mucin-type glycoproteins (Bavington et al., 2004). This commonality is not surprising considering that mucin-type glycoproteins are widely-occurring biomolecules whose relatively ancient origins can be traced to as far as lower metazoa (e.g., sea anemones; Lang et al., 2007),

4.3.2 Proton Adsorption and Discrete Ligand Modeling

Potentiometric titration data are first evaluated as charge excess in the titration system, expressed at any point in the titration as

$$C_b + [H^+] + [ANC] = C_a + [OH^-] + \sum_{j=1}^{n} [L_j^-] \qquad (1)$$

where C_b and C_a are the concentrations of base and acid, $[H^+]$ and $[OH^-]$ are concentrations calculated with SIT activity coefficients (Pettit et al., 2006) from H^+ activity data recorded by the pH electrode, $[L_j^-]$ is the concentration of deprotonated functional groups for the j^{th} monoprotic ligand of n possible ligands, and the acid-neutralizing capacity [ANC] is a constant representing the difference between functional groups that remain protonated and those that remain deprotonated over the titration range. A zero proton condition cannot be defined from these data sets, as the mucous material exchanges protons over the entire titration range; instead, charge excess is assigned to zero at pH 4, and all reported

charge excess values (and modeled functional group concentrations) are relative to the titration starting point (pH 4). Charge excess is assumed to accumulate with increasing pH by the deprotonation of proton-reactive functional group ligands (L_n) in the form:

$$HL_n^{+1} \leftrightarrow L_n^{-1} + H^+ \quad (3)$$

Discrete ligand models accounting for excess charge by functional group deprotonation were fitted to the data in two ways: (1) using linear programming to optimize ligand concentrations at every possible point in a fixed pK_a interval (in this case, 4 to 10 in 0.2 increments) (Matlab script complements of D. Scott Smith; c.f. Brassard et al., 1990; Cox et al., 1999; Smith et al., 1999; Lalonde et al., 2008, for further details), and (2) using least squares optimization in FITEQL (Westall, 1982) to resolve, for a pre-determined number of ligands, pK_a values and ligand concentrations that best describe the excess charge data. In the case of the latter, a three-ligand model adequately described the data (V(Y)=3.70±0.20 (2 SE)), and a four-ligand model provided no significant improvement. A non-electrostatic model (NEM) was chosen here for simplicity, as only one ionic strength (0.5M NaCl) was explored, and recent studies have indicated that electrostatic surface field effects on protonation are minimal relative to experimental uncertainties for routine titration of organic materials such as bacterial surfaces (Borrok and Fein, 2005) and humic/fulvic acids (Borrok and Fein, 2004).

Charge excess in the titration, assumed here to arise solely by the deprotonation of organic functional groups in the mucous material, is presented in Figure 4-3A. Distinct inflection points are absent in the titration data, consistent with complex organic matter possessing diverse functional groups with pK_a values distributed over the entire titration range. Interestingly, the shape of the charge excess curves mimic those determined for a variety of humic and fulvic substances by Milne et al. (2001). Differences in excess charge between titration replicates represents some degree of irreproducibility, possibly indicating sample heterogeneity. Discrete ligand models fit to the excess charge data are presented as calculated excess charge (solid and stippled lines in Figure 4-3A), and as pK_a spectra in Figure 4-3B (linear programming optimization) and Figure 4-3C (least

squares optimization). While the discrete ligand model developed by least squares optimization (Figure 4-3C) was constrained to three ligands by the optimization algorithm, the number of ligands in the model developed by linear programming is limited only by the chosen pK_a interval (in this case, 30 ligands, spanning from pK_a 4 – 10 in increments of 0.2), and a best fit was obtained by a combination of three major ligands and three minor ligands. The three major ligands in this model approximately correspond to the three ligands in the least squares model in terms of pK_a and concentration (see Figure 4-3; Table 4-1). Based on compositional data, FTIR spectra, and analogy in acidity constant with respect to known compounds, the three ligands likely correspond to carboxyl, phosphoryl, and thiol groups, respectively, although, more detailed spectroscopy aimed at determining surface ligand structures would be required for absolute identification (see discussion below). Differences between the two models, namely the presence of "other ligands" beyond the three major ligands identified by both, can be attributed to the fact that the linear programming optimization possesses the freedom to attribute excess charge from what would be restricted to a single ligand in the least squares optimization to multiple ligands in the linear programming optimization, for marginally small increases in the goodness of fit of the model. As both models describe the titration data with little relative error, the supposition of additional ligands by the linear programming optimization is of little benefit. As such, it is presented only for the purposes of comparison to other studies where linear programming optimization was similarly employed.

The model parameters fitted to the titration data are presented in Table 4-1; both modeling approaches yielded total ligand concentrations in the pK_a 4 to 10 range of approximately 11 mmol per dry gram, with no significant difference in total ligand concentrations between the two models (within experimental uncertainty). This value is relatively high compared to that observed for fulvic substances (7.74 mmol/g, average of 25 fulvic acids, Milne et al. (2001)), humic substances (5.70 mmol/g, average of 24 humic acids, Milne et al. (2001)), and bacterial surfaces (3.2 mmol/g (assuming a dry:wet ratio of 10:1), average of 36 bacterial species, Borrok et al. (2005)) (Figure 4-4). It is also significantly higher

than values observed for inorganic phases commonly considered to be important sorbents in surface and near-surface environments, such as hydrous ferric oxide (synthetic: 2.42 mmol/g, Smith and Ferris, 2001; natural, 2.16 to 5.44 mmol/g, Lalonde et al., 2007). The elevated surface ligand concentration of the mucous material relative to other organic materials is possibly due to the highly soluble nature and extended fiber conformation of mucin-type materials at circumneutral pH; porcine gastric mucin, an analogous compound often employed for the physiological study of mucus and as a growth substrate for enterobacteria, possesses an extended fibrous structure of 1-2 nm in diameter and approximately 400 nm in length at pH 5-7 (Hong et al., 2005). Such an extended conformation may provide proton access to ligands that would otherwise be inaccessible in more aggregated biomolecules. The mucous material possesses an acid-base reactivity (over the pH 4-10 range) that is 1.2 to 3 times that of other forms of natural organic matter (e.g. fulvic, humic, and bacterial organic matter; Figure 4-4); clearly, the mucous material possesses the potential, in terms of available reactive ligands, to significantly influence dissolved ion mobility at the organic-water interface. Furthermore, the mucous material exchanges protons over the entire titration range investigated herein (pH 4-10), such that with increasing pH, the proportion of deprotonated ligands that are available to participate in cation adsorption reactions increases steadily with increasing pH. At typical seawater pH (7.4 - 8.2), approximately half of the inferred ligands should be in an anionic form immediately conducive to metal adsorption. Thus, with respect to both adsorption ligand density and availability, and in terms of reactive components in marine sediment, mucous materials associated to burrowing animals should be considered an important potential sink for metals. We further investigate this potential using batch Cd adsorption experiments, described below.

4.3.3 Cadmium adsorption

In addition to the availability of absorptive ligands in terms of concentration, the affinity of surface-complexed metals for each of these ligands also plays a central role in determining partitioning between solid surfaces and the aqueous phase.

This affinity is best described in the form of metal-ligand stability constants that can be employed in a chemical equilibrium framework accounting for speciation of both surface ligands and the speciation of potential sorbates in the aqueous phase.

For our experimental conditions (approximating seawater chloride salinity), chemical equilibrium modeling reveals that Cd is present largely as the chloride complexes $CdCl_2$ (aq) and $CdCl^-$, with lesser $CdCl_3^-$ and Cd^{2+} (Figure 4-5). In the pH 2 - 10 working range, these dominant species are largely insensitive to changes in pH, although at alkaline pH the hydrolyzed Cd species $CdOHCl^0$ (aq), and to a lesser extent, $CdOH^+$, and $Cd(OH)_2$ (aq), become important. $Cd(OH)_2$ (s) precipitation was not indicated for any experimental condition. Stability constants from the MINTEQA2 v4.0 database (Allison et al., 1991) for all Cd species displayed in Figure 4-5 were included for consideration in modeling of Cd-ligand stability constants, discussed below.

Experimental data for Cd adsorption to worm mucous material is presented in Figure 4-6. Cd adsorption generally increases with increasing pH as functional groups progressively deprotonate, however, at low pH some Cd is adsorbed despite the fact that ligands 1-3 are largely protonated below pH 4. For surface complexation modeling of Cd adsorption data, Cd-ligand stability constants were defined based on the following hypothesized surface adsorption reactions, for ligands $L_1 - L_3$ identified by least squares optimization of titration data (Table 4-2):

$$L_n^{-1} + Cd^{2+} \leftrightarrow L_nCd^{+1} \quad (3)$$

These three reactions alone were insufficient to account for adsorption data at low pH (see below), and at high pH, $CdOHCl^0$ becomes the dominant Cd species; accordingly, two additional reactions were considered in the adsorption models:

$$HL_n + Cd^{2+} \leftrightarrow HL_nCd^{+2} \quad (4)$$

$$L_n^{-1} + CdOHCl^0 \leftrightarrow L_nCdOHCl^- \quad (5)$$

Reaction (4) involves Cd adsorption to a fully protonated functional group and can account for the observed Cd adsorption at low pH where no ligands are significantly deprotonated, while reaction (5) can account for Cd adsorption at alkaline pH where $CdOHCl^0$ is the most abundant Cd species (as per Figure 4-5). Various permutations of possible adsorption reactions were examined for fit to the

data using the program FITEQL (Westall, 1982). Table 4-3 lists the individual models considered, along with best-fit Cd-ligand stability constants and a model variance parameter (V(Y)) that provides an indication of goodness-of-fit, with smaller values indicating better agreement between the experimental data and the model.

Models invoking Cd adsorption to only one or two of the three ligands provided relatively poor fits (Table 4-3), as did models negating the possibility of adsorption to protonated sites (reaction 4). It can be seen from both model variance parameters and fitted log K values that model fit was insensitive to the particular ligand (HL1, HL2, HL3) chosen as the site for protonated-ligand Cd adsorption (i.e., compare models 10-11, 13-15); this is due to high similarity in ligand concentrations and protonation states at low pH ranges where HL_xCd^{2+} surface complexation is most important to the model fit. Model fit was similarly insensitive to choice of ligands forming complexes with $CdOHCl^0$ because this Cd species has little effect on model fit until pH >9 where its concentration becomes important. While consideration of Cd adsorption in the form of $CdOHCl^0$ logically follows from its increasing importance at alkaline pH (see Figure 4-5), the consideration of Cd adsorption in the form of Cd^{2+}, to both protonated and deprotonated sites, is less obvious. Cd^{2+} should, with its smaller radius and greater charge, be the most reactive of the Cd species under consideration, and indeed, previous work indicates that the reactivity of cadmium-chlorine complexes appears negligible compared to Cd^{2+} (Voegelin et al., 2001; Temminghoff et al., 1995). However, it must be noted that due to relatively unchanging speciation of dissolved cadmium over the experimental pH range (2-10), adsorption reactions involving Cd species other than Cd^{2+}, such as $CdCl^+$, $CdCl_2$ (aq), and $CdCl_3^-$, while less likely to be important, cannot be ruled out by the adsorption data alone.

Best fit to total Cd adsorbed is achieved when all three ligands are modeled as participating in Cd adsorption, and when reactions (4) and (5) are included (models 16-18, essentially identical in goodness-of-fit). Cd adsorption calculated for one of these models (model 16, black line) is presented alongside the experimental data in Figure 4-6A, accompanied by calculated Cd speciation over the experimental pH

range (Figure 4-6B). Also included in Figure 4-6A is model 12 (grey line), where only Cd^{2+} adsorption to the three deprotonated ligands are considered. The increase in model goodness-of-fit resulting from the consideration of reaction (4) and (5) is readily apparent, where HL_1Cd^{2+} better accounts for adsorption at low pH, and $L_1CdOHCl^-$ provides slightly increased fit at high pH, respectively. The increase in model goodness-of-fit by consideration of reaction (5) is relatively minor (compare models 13-15 with 16-18); this is attributable to the fact that reaction (5) is important only at the alkaline extreme of the adsorption experiments, and as such, support for it in this dataset is relatively weak, resting on a single data point. While $CdOHCl^0$ adsorption could be ignored for the modeling of most natural waters (i.e., pH <9) without consequence (Table 4-3), it is included here for the consideration of future studies examining Cd adsorption at more alkaline or saline conditions where $CdOHCl^0$ is the dominant Cd species. At low pH, it should be noted that some adsorption may be due to functional groups undetected by titration that continue to exchange protons and metals at low pH; such appears to be the case with fulvic substances (Saar and Weber, 1979), humic substances (Liu and Gonzales, 2000) and bacteria (Fein et al., 2005).

Although certain assignment of specific ligand identities (such as the carboxyl, phosphoryl, thiol, amino, and hydroxyl functional groups typical of organic matter) is not possible without additional spectroscopic evidence, assignment based on acidity constants alone, in a manner similar to Fein et al. (1997), would indicate that ligands 1 and 2 represent carboxyl and phosphoryl groups, respectively. Best-fit Cd-ligand stability constants (log K values; model 16) for these ligands are 2.19 and 3.86, surprisingly comparable to some ligands of similar pK_a that have been indicated for a range of bacterial consortia (log K values of 2.7 and 3.95; sites 2 and 3, Borrok et al., 2004). With this tentative ligand assignment, the adsorption of Cd^{2+} as a function of pH onto deprotonated ligands L1 and L2 (Figure 4-6B) parallels observations from x-ray adsorption fine-edge spectroscopy of Cd adsorption to *Bacillus subtilis* cell walls (Boyanov et al., 2003) in that Cd adsorption occurs predominately to carboxyl ligands at pH ranges

between 5-7, with smaller contribution from a possible Cd-phosphoryl complex at higher pH (>7.8).

The third site (L3) possesses the highest Cd-ligand stability constant. Strong Cd adsorption in this pH range is consistent with the presence of highly-chalcophile thiol functional groups as indicated by infrared spectroscopy (discussed above). The assignment of the highly Cd-reactive thiol functional groups for ligand 3, in lieu of other possible organic ligands for this acidity range (e.g., amino, hydroxyl), is preferred as the latter have not been reported to possess strong affinity for Cd, whereas Cd adsorption to thiol groups is strong (log K values of 8.8 and 4.8 for 3-mercaptopropionic acid Cd^{2+} -monothio and -diothio complexes, respectively; Vairavamurthy et al., 2000). Indeed, the high thiol functional group content of mucus and mucin-type glycoproteins has been long known, and has been implicated in the strong adhesivity of these materials by enhanced disulfide cross-linking ability (e.g., Leitner et al., 2003).

It appears that mucous materials such as the *Thelepus* mucus studied herein possess strong affinities for chalcophile elements such as Cd, potentially as a consequence of their "sticky" nature conferred by the presence of abundant thiol groups and thiol-rich cysteine residues. It is possible that mucous materials possess, or once possessed, a dual function, one being physical protection in the form of adhesion and resistance to desiccation, and the other being chemical, acting as a nutrient sieve that focuses metals and nutrients for the organism's benefit, or perhaps the benefit of the microbial colonies that typically accompany the linings of burrowing organisms in a symbiotic fashion (e.g., Aller and Aller, 1986). Given their small size, dense surface ligand concentrations, and pervasive occurrence across the animal kingdom, mucus secretions comprised of mucin-type glycoproteins hold a vast potential with respect to metal sequestration budgets in estuarine settings. Further work quantitatively exploring the distribution and abundance of such mucous materials in estuarine sediments will enable a better understanding of the overall importance of such materials in the sequestration of dissolved metals and contaminants.

4.4 Conclusion

It was determined that the mucous material produced during bioturbation by *Thelepus crispus* worms consists of a mucin-type glycoprotein that is homologous to other marine animal mucus secretions (e.g., those of echinoderms), and is likely representative of mucous secretions throughout the marine worm community. Acid-base titrations revealed that the mucous material possesses unusually high proton reactivities, on the order of 11 mmol per dry gram summed over pH 4 to 10, with proton-exchanging ligands distributed approximately equally across the titration range. Discrete ligand modeling indicated that three ligands are sufficient to accurately describe proton adsorption across the titration range, and when considered in combination with FTIR and compositional data, indicate the presence of abundant proton-exchanging carboxyl, phosphoryl, and thiol functional groups. Cd adsorption experiments indicate strong adsorption of Cd to worm mucous material, with Cd-ligand stability constants comparable to those determined for bacterial surfaces. While it is possible that worm mucous linings play some physiological role as ion-selective sieves, it is clear that they serve as efficient sorbents for chalcophile elements such as Cd, potentially due in part to high thiol functional group content. Based on these findings, the mucous secretions produced by burrowing marine organisms should not be overlooked when evaluating seawater metal partitioning at the sediment-water interface.

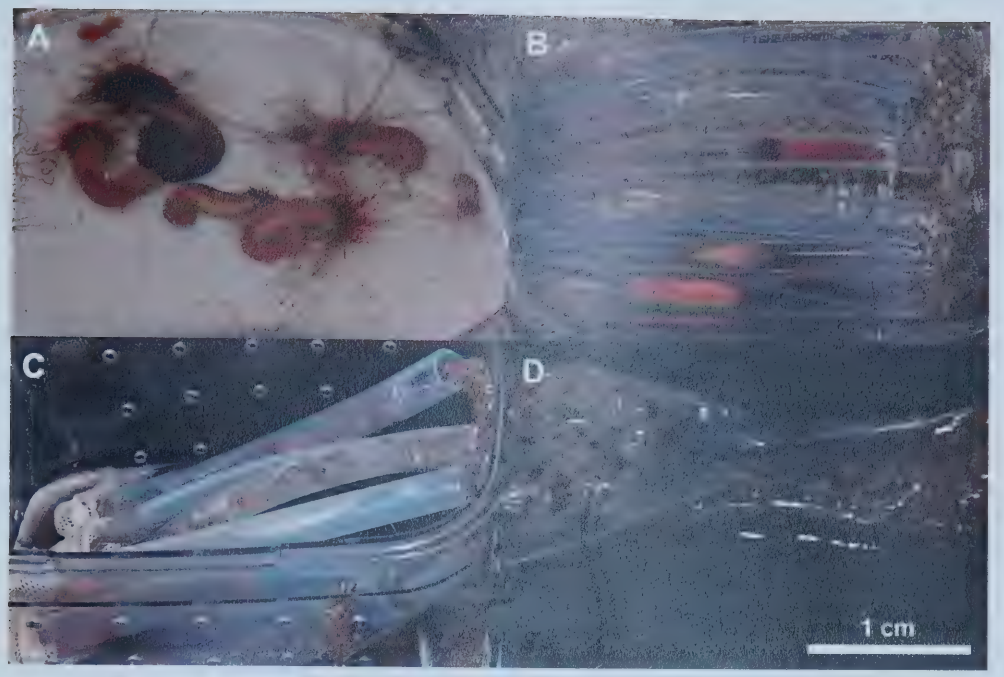

Figure 4-1. (A) Terebellid *Thelepus crispus* worms resting on pure quartz sand within an isolated section of a circulating salt-water tank. Note the extended palps used to transport food particles to the mouth. (B) Worms in another isolated section of the same tank, inserted into ½ inch PVC tubing to stimulate mucus production. One end of each tube was subsequently sealed with cheesecloth for the duration of incubation. (C) Mucous burrow linings produced after 15 days of incubation in PVC tubing. Several worms continued to produce burrows even upon exiting their PVC tubing. (D) Isolated burrow lining. Brown substance likely represents microbial and fecal organic matter, and was removed by scraping, agitation, and rinsing prior to analyses.

A

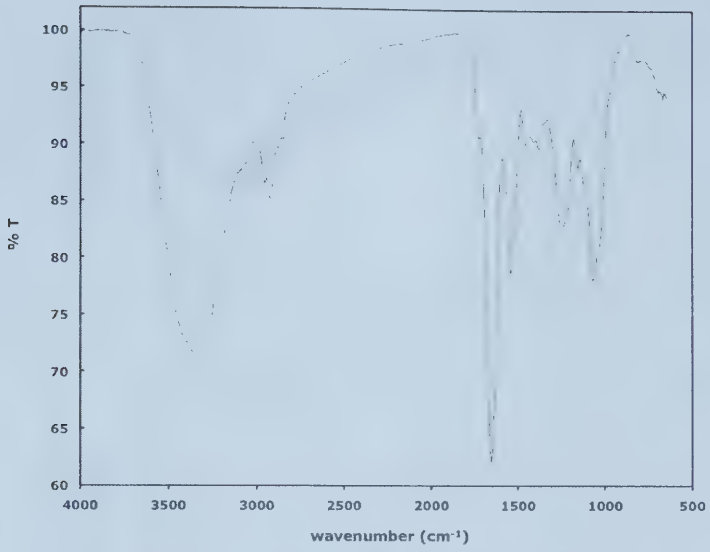

B

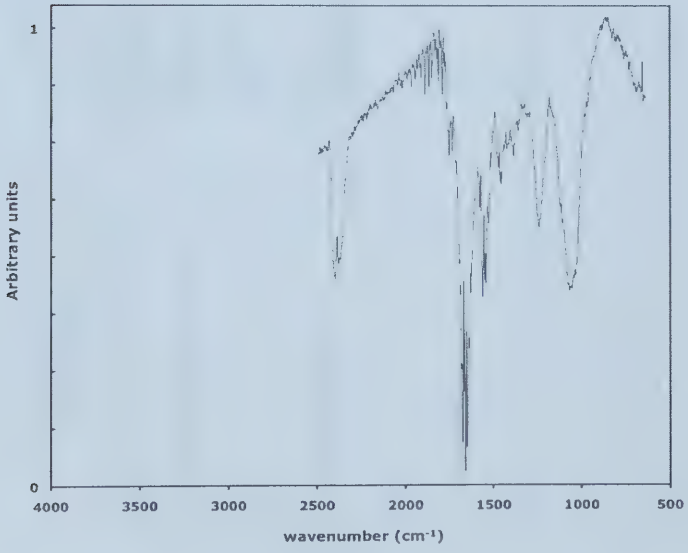

Figure 4-2. FTIR spectra of (A) air-dried *Terebellid* burrow wall mucous material (transmission mode microscope-FTIR, this study), and (B) partially-purified and freeze-dried mucous glycoproteins from the brittlestar *Ophiocomina nigra* (zinc-selinide ATR-FTIR, reproduced from Bavington et al., 2004).

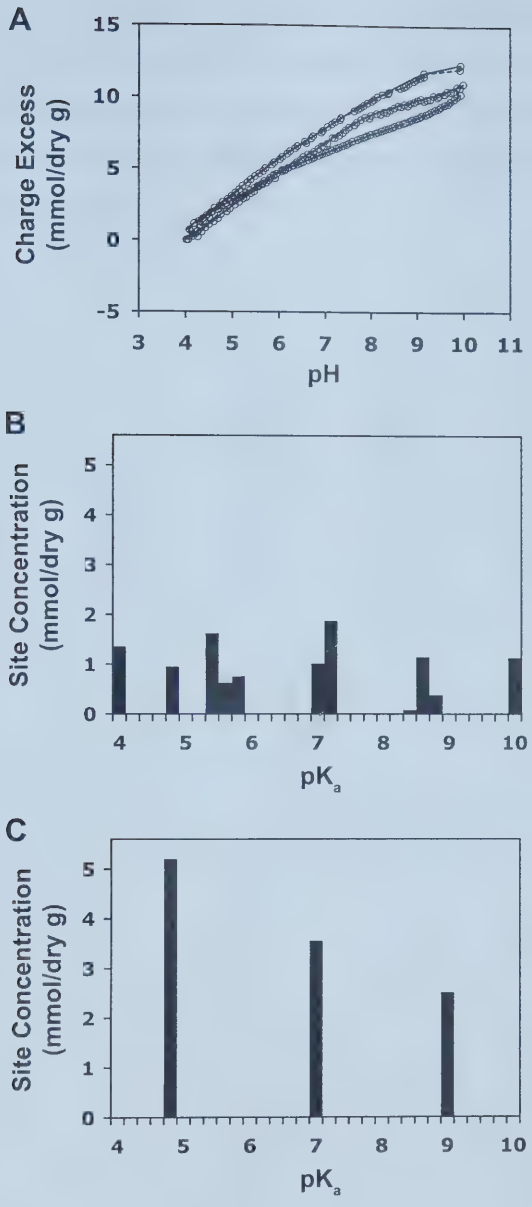

Figure 4-3. (A) Excess charge arising as a function of pH during acid-base titration, reflecting progressive deprotonation of organic functional groups comprising the mucous material. Data points represent titration data, while solid and stippled lines represent the model fit excess charge calculated from the discrete ligand models presented in (B) and (C). In (B) and (C), best-fit discrete ligand models obtained by linear programming (B) and least squares (C) optimization

represent the set of functional groups, in terms of concentration (y-axis) and acidity constant (x-axis), that best describe the charge excess data. The least squares optimization was constrained in number of ligands (three) while the linear programming optimization was constrained by pK_a resolution (pK_a values only permitted in increments of 0.2).

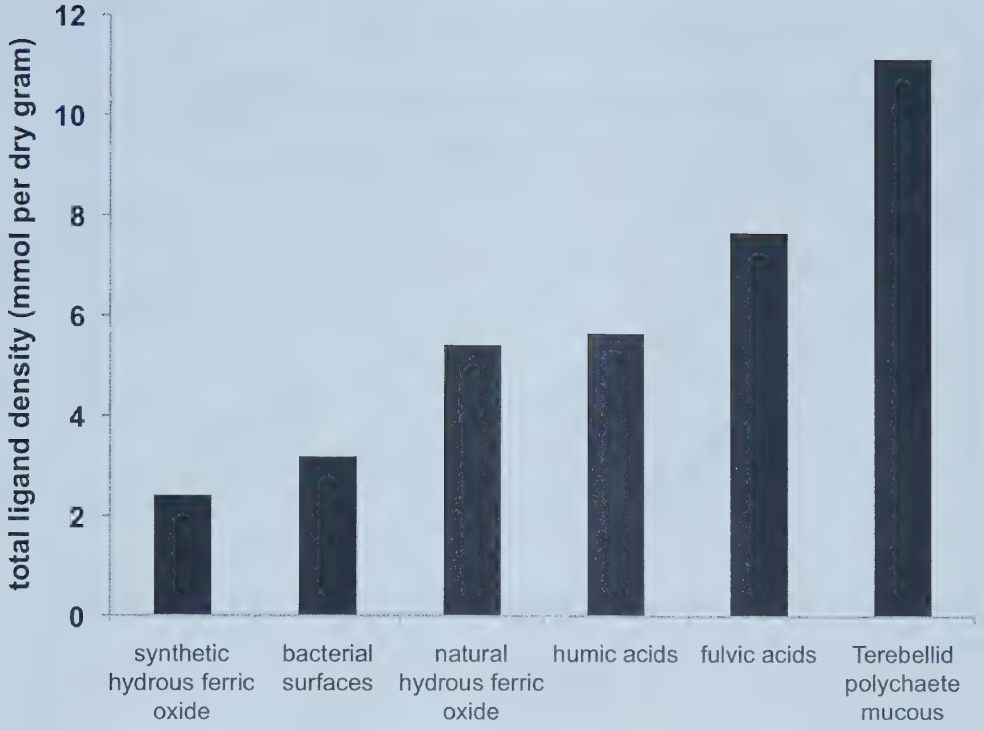

Figure 4-4. Comparison of *Terebellid* mucous total ligand density (summed over pH 4-10 range) with other materials considered important adsorbents in natural systems. See text for values and references.

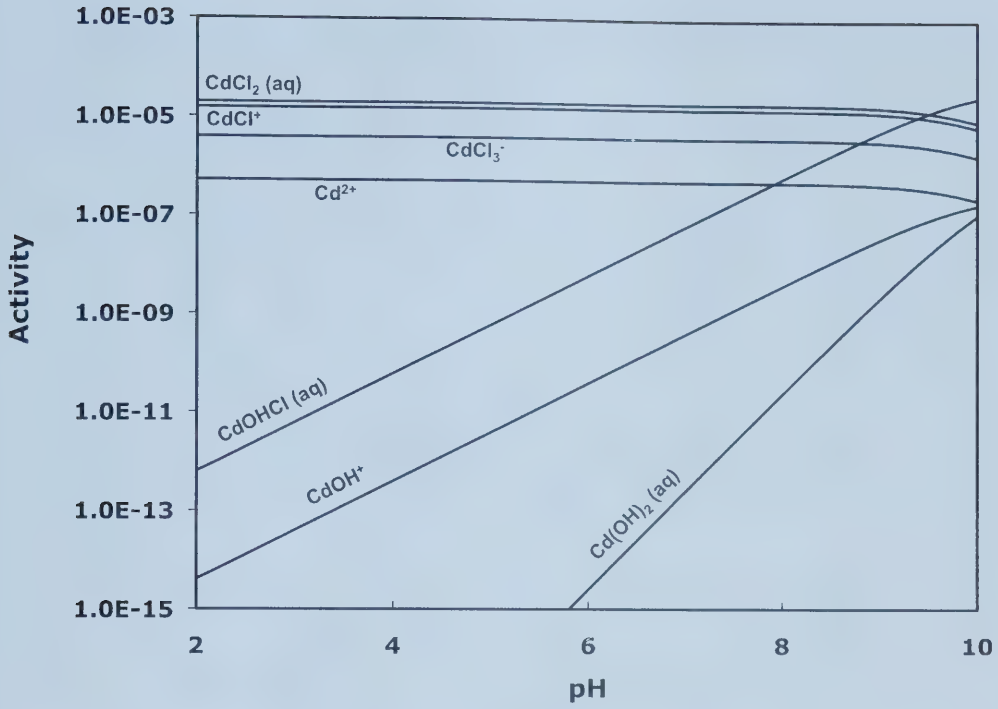

Figure 4-5. Aqueous Cd speciation as a function of pH for the Cd adsorption conditions (0.5 M NaCl, 5 ppm Cd, pH 2 - 10). Cadmium chloride complexes form the dominant species below pH ~9. See methods for equilibrium modeling details.

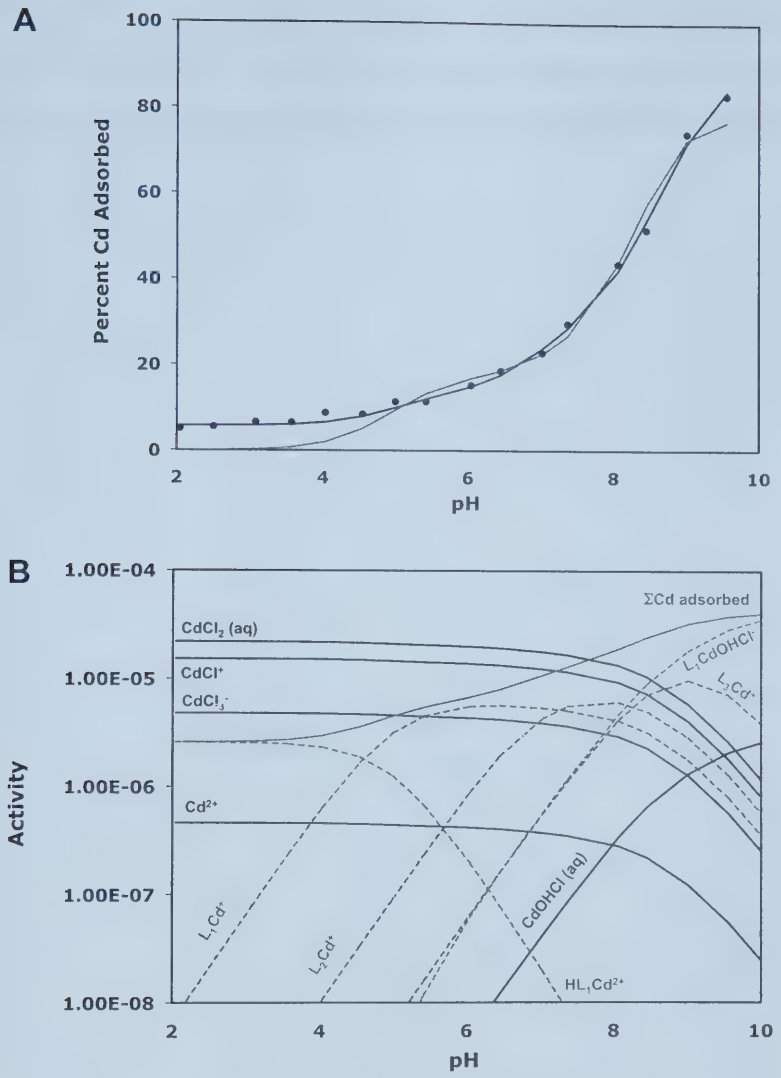

Figure 4-6. (A) Cd adsorption data (points) as a function of pH for 5 ppm Cd solutions with 1.0 g/L of mucous material. Two non-electrostatic Cd surface complexation models are presented: Cd^{2+} adsorption to deprotonated ligands L1-L3 only (Table 4-3, model 12; grey line), and the same with the inclusion of reactions 4 and 5 (Table 4-3, model 16; black line). Best-fit is achieved when reactions 4 and 5 are considered, better accounting for adsorption at the low and high pH extremes, respectively, although the importance of reaction 5 is relatively small and unsupported (see text). (B) Cd speciation calculated for the best fitting model

(Table 4-3, model 16; black line in (A)) as a function of pH in the Cd adsorption experimental conditions. Aqueous species are presented as black solid lines, adsorbed species as grey dotted lines, and the total Cd adsorbed as a solid grey line.

Carbon	Hydrogen	Nitrogen	Sulfur	Protein	Carbohydrate	Lipid*
15.70±1.64	2.37±0.35	3.13±0.41	1.23±0.08	19.56±4.54	4.72±1.21	0.10

Table 4-1. Terebellid mucous compositional data. All data expressed in weight percent (error 2SE). C,H,N, and S were analyzed by a gas chromatograph elemental analyzer, protein calculated from N content, and carbohydrate and lipid quantified by solvent extraction followed by gas chromatography (see methods 4.2.2). *Single analysis.

	pKa			concentration (mmol/g)				
	Site 1	Site 2	Site 3	Site 1	Site 2	Site 3	other sites	Total
Linear Programming (MATLAB 7)	5.57±0.23	7.14±0.06	8.65±0.14	3.01±0.61	3.07±0.70	1.65±0.95	3.26±0.92	10.99±3.18
Sum of Squares (FITEQL 4.0)	4.89±0.18	6.93±0.26	8.98±0.50	5.20±0.23	3.55±0.88	2.51±0.68	n/a	11.26±1.79

Table 4-2. Parameters obtained from best-fit non-electrostatic proton adsorption models of titration data. For the purposes of comparison, ligands in the linear programming model with pK_a values below 5 or above 9 were classified as "other ligands". These ligands, while always indicated by linear programming, were inconsistent in pK_a between independent titrations. Uncertainties represent 2SE calculated from independent modeling of titration triplicates.

model	Cd-complexing ligands	log K					V(Y)
		$L_xCdOHCl^-$	HL_xCd^{2+}	CdL1	CdL2	CdL3	
1	L1 only			-1.65			54.08
2	L2 only				-3.17		24.93
3	L3 only					-4.17	17.66
4	L1 and HL1		1.91	-1.66			57.51
5	L2 and HL2		2.48		-3.18		22.28
6	L3 and HL3		2.86			-4.27	4.54
7	L1 and L2			-2.44	-3.22		25.47
8	L2 and L3				-3.52	-4.47	9.28
9	L1 and L3			-2.04		-4.36	3.08
10	HL1, L1, L3		2.24	-2.07		-4.35	1.22
11	HL3, L1, L3		2.56	-2.21		-4.35	1.22
12	L1-L3			-2.07	-4.41	-4.38	3.24
13	HL1, L1-L3		2.27	-2.16	-4.10	-4.40	0.99
14	HL2, L1-L3		2.44	-2.34	-3.95	-4.40	0.99
15	HL3, L1-L3		2.59	-2.34	-4.10	-4.39	0.99
16	HL1, HL1, L1-L3	-9.62	2.28	-2.19	-3.86	-4.88	0.30
17	HL2, HL2, L1-L3	-11.49	2.45	-2.41	-3.74	-4.89	0.30
18	HL3, HL3, L1-L3	-13.39	2.60	-2.41	-3.86	-4.57	0.30

Table 4-3. Cd adsorption models based on adsorption data (points in Figure 4-5) and the three proton-reactive ligands (L1, L2, L3) indicated by titration. HL1, HL2, and HL3 correspond to the same ligands in protonated form. Fitted model parameters (log K) are provided in order of the Cd-complexing ligands under consideration (first column), along with an indication of model fit (the FITEQL variance function V(Y)), where smaller values indicate better fit to the data.

4.5 References

Aller, J.Y., Aller, R.C., 1986. Evidence for localized enhancement of biological activity associated with tube and burrow structures in deep-sea sediments at the HEBBLE site, western North Atlantic. Deep Sea Res Part A 33 (6A), 755-790.

Allison, J.D., Brown, D.S., and Novo-Gradac., K.J. .1991. MINTEQA2/PRODEFA2, A geochemical assessment model for environmental systems: Ver. 3.0 Users manual. Athens, GE, USA: US EPA.

Bavington, C.D., Lever, R., Mulloy, B., Grundy, M.M., Page, C.P, Richardson, N.V., McKenzie, J.D., 2004. Anti-adhesive glycoproteins in echinoderm mucus secretions. Comp. Biochem. Physiol. Part B: Biochem. Mol. Biol. 138 (4), 607-617.

Benoit, G., Oktay-Marshall, S.D., Cantu, A., Hood, E.M., Coleman, C.H., Corapcioglu, M.O., Santaschi, P.H., 1994. Partitioning of Cu, Pb, Ag, Zn, Fe, Al, and Mn between filter-retained particles, colloids, and solution in six Texas estuaries. Mar. Chem. 45 (4), 307-336.

Borrok, D.M., Fein, J.B., 2004. Distribution of protons and Cd between bacterial surfaces and dissolved humic substances determined through chemical equilibrium modeling. Geochim. Cosmochim. Acta 68 (14), 3043-3052.

Borrok, D.M., Fein, J.B., 2005. The impact of ionic strength on the adsorption of protons, Pb, Cd, and Sr onto the surfaces of Gram negative bacteria: testing non-electrostatic, diffuse, and triple-layer models. J. Colloid Interface Sci. 286 (1), 110-126.

Borrok, D.M., Turner, B.F., Fein, J.B., 2005. A universal surface complexation framework for modeling proton binding onto bacterial surfaces in geological settings. Am. J. Sci. 305 (6-8), 826-853.

Boyanov, M.I., Kelly, S.D., Kemner, K.M., Bunker, B.A., Fein, J.B., Fowle, D.A., 2003. Adsorption of cadmium to *Bacillus subtilis* bacterial cell walls: A pH-dependent X-ray absorption fine structure spectroscopy study. Geochim. Cosmochim. Acta 67 (18), 3299-3311.

Brandenburg, K., Seydel, U., 1996. Fourier transform infrared spectroscopy of cell surface polysaccharides. In: Mantsch, H.H., Chapman, D. (Eds.), Infrared Spectroscopy of Biomolecules. Wiley-Liss, New York, 203-237.

Brassard, P., Kramer, J.R., Collins, P.V., 1990. Binding site analysis using linear programming. Environ. Sci. Technol. 24 (2), 195-201.

Bryan, G.W., Hummerstone, L.G., 1973. Adaptation of the polychaete Nereis diversicolor to estuarine sediments containing high concentrations of zinc and cadmium. J. Mar. Biol. Assoc. U.K. 53 (4), 839-857.

Bryan, G.W., Langston, W.J., 1992. Bioavailability, accumulation and effects of heavy metals in sediments with special reference to United Kingdom estuaries: a review. Environ. Pollut. 76 (2), 89-131.

Bryan, G.W., Langston, W.J., Hummerstone, L.G., Burt, G.R., Ho, Y.B., 1983. An assessment of the gastropod, Littorina littorea, as an indicator of heavy-metal contamination in United Kingdom Estuaries. J. Mar. Biol. Assoc. U.K. 63 (2), 327-345.

Chiffoleau, J.F., Cossa, D., Auger, D., Truquet, I., 1994. Trace metal distribution, partition and fluxes in the Seine Estuary (France) in low discharge regime. Mar. Chem. 47 (2), 145-158.

Cox, J.S., Smith, D.S., Warren, L.A., Ferris, F.G., 1999. Characterizing heterogeneous bacterial surface functional groups using discrete affinity spectra for proton binding. Environ. Sci. Technol. 33 (24), 4514-4521.

Fein, J.B., Boily, J-F., Yee, N., Gorman-Lewis, D., Turner, B.F., 2005. Potentiometric titrations of Bacillus subtilis cells to low pH and a comparison of modeling approaches. Geochim. Cosmochim. Acta 69 (5), 1123-1132.

Fein, J.B., Daughney, C.J., Yee, N., Davis, T.A., 1997. A chemical equilibrium model for metal adsorption onto bacterial surfaces. Geochim. Cosmochim. Acta 61 (16), 3319-3328.

Gustafsson, J.P. (2000) Visual Minteq [www document]. URL http://www.lwr.kth.se/English/OurSoftware/vminteq/ (verified 25 October 2009).

Hong, Z., Chasan, B., Bansil, R., Turner, B.F., Bhaskar, K.R., 2005. Atomic force microscopy reveals aggregation of gastric mucin at low pH. Biomacromolecules 6 (6), 3458-3466.

Konhauser, K.O., 2007. Introduction to Geomicrobiology. Blackwell publishing, Oxford, UK.

Lalonde, S.V., Amskold, L., Mcdermott, T.R., Inskeep, W.P., Konhauser, K.O., 2007. Chemical reactivity of microbe and mineral surfaces in hydrous ferric oxide depositing hydrothermal springs. Geobiology 5 (3), 219-234.

Lalonde, S.V., Smith, D.S., Owttrim, G.W., Konhauser, K.O., 2008. Acid–base properties of cyanobacterial surfaces I: Influences of growth phase and nitrogen metabolism on cell surface reactivity. Geochim. Cosmochim. Acta 72 (5), 1257-1268.

Lang, T., Hansson, G.C., Samuelsson, T., 2007. Gel-forming mucins appeared early in metazoan evolution. Proc. Nat. Acad. Sci. 104 (41), 16209-16214.

Leitner, V.M., Walker, G.F., Bernkop-Schnürch, A., 2003. Thiolated polymers: evidence for the formation of disulphide bonds with mucus glycoproteins. Eur. J. Pharm. Biopharm. 56 (2), 207-214.

Liu, A., Gonzalez, R.D., 2000. Modeling adsorption of copper (II), cadmium (II) and lead (II) on purified humic acid. Langmuir 16 (8), 3902-3909.

Luoma, S.N., Van Geen, A., Lee, B.G., Cloern, J.E., 1998. Metal uptake by phytoplankton during a bloom in South San Francisco Bay: Implications for metal cycling in Estuaries. Limnol. and Oceanogr. 43 (5), 1007-1016.

Maynard, L.A. and Loosli, J.K., 1969. Animal Nutrition. 6th Ed., McGraw-Hill, New York, USA

Millward, G.E., Glegg, G.A., 1997. Fluxes and retention of trace metals in the Humber Estuary. Estuarine Coastal Shelf Sci. 44 (Supp. A), 97–105.

Milne, C.J., Kinniburgh, D.G., Tipping, E., 2001. Generic NICA-Donnan model parameters for proton binding by humic substances. Environ. Sci. Technol. 35 (10), 2049-2059.

Over, D. (1990) Trace metals in burrow walls and sediments, Georgia Bight, USA. Ichnos 1(1), 31-41.

Pettit, L.D., Sukhno, I., Buzko, V. (2006) *Ionic Strength Corrections for Stability Constants using Specific Interaction Theory. Ver. 2.0.* York, UK: IUPAC-Academic Software.

Rouse, G.W., Fauchald, K., 1997. Cladistics and polychaetes. Zoologica Scripta 26 (2), 139-204.

Saar, R.A., Weber, J.H., 1979. Complexation of cadmium (II) with water-and soil-derived fulvic acids: effect of pH and fulvic acid concentration. Can. J. Chem. 57 (11), 1263-1268.

Smith, D.S., Adams, N.W.H., Kramer, J.R., 1999. Resolving uncertainty in chemical speciation determinations. Geochim. Cosmochim. Acta 63 (19-20), 3337-3347.

Smith, D.S., Ferris, F.G., 2001. Proton binding by hydrous ferric oxide and aluminum oxide surfaces interpreted using fully optimized continuous pK_a spectra. Environ. Sci. Technol. 35 (23), 4637-4642.

Temminghoff, E.J.M, Van Der Zee, S.E.A.T.M., and De Haan, F.A.M. (1995) Speciation and calcium competition effects on cadmium sorption by sandy soil at various pHs. Eur. J. Soil Sci. 46, 649-655.

Vairavamurthy, M.A., Goldenburg, W.S., Ouyang, S., and Khalid, S. 2000. The interaction of hydrophilic thiols with cadmium: investigation with a simple model, 3-mercaptopropionic acid. Mar. Chem. 70, 181-189.

Voegelin, A., Vulava, V.M., and Kretzschmar, R. 2001. Reaction-based model describing competitive sorption and transport of Cd, Zn, and Ni in an acidic soil. Environ. Sci. Technol. 35 (8), 1651-1657.

Westall, J.C., 1982. FITEQL: A computer program for determination of chemical equilibrium constants from experimental data. Version 4.0, Dept. Chem., Oregon St. Univ., Corvallis, OR, USA.

Zorn, M.E., Muehlenbachs, K., Gingras, M.K., Konhauser, K.O., Pemberton, S.G., Evoy, R., 2007. Stable isotopic analysis reveals evidence for groundwater-sediment-animal interactions in a marginal-marine setting. Palaios 22 (5), 546-553.

CHAPTER 5

Summary

5.1 Surface chemical reactivity of natural microbial biomass

Microbial cell surfaces and polymeric exudates are important natural sorbents owing to their ubiquity, hydrophilicity, high surface area to volume ratios, and abundance of reactive organic surface functional groups. Knowledge of the composition, concentration, and aqueous ion affinities of microbial surface functional groups is crucial for understanding the microbial role in elemental mobility and mineral nucleation in soils, sediments, and natural waters. Surface complexation models originally developed for mineral surfaces have achieved significant success in accounting for proton and metal adsorption by microbial biomass cultured under laboratory conditions (e.g., Fein et al., 1997; Borrok et al., 2004). However, difficulties inherent in isolating microbes from other sediment constituents in natural samples have prevented the direct characterization of naturally-occurring microbial biomass. To bridge this knowledge gap between laboratory experiments and natural systems, microbial biomass was harvested from several contrasting hydrothermal springs in Yellowstone National Park (YNP), USA, where it grows naturally as macroscopic mats largely free of detrital material. As described in Chapters 2 and 3, samples were subjected to leaching experiments to evaluate elemental partitioning from stream waters, and subject to acid-base titration to characterize and quantify proton-reactive surface functional groups for direct comparison to data from laboratory cultures.

In Chapter 2, samples of cyanobacterial mat of diverse morphologies (e.g., streamers, spires, and thick mats) were collected from Mound spring, an alkaline hydrothermal system in the Sentinel Meadows area, YNP. A small sampling area (<2.5 m^2) was chosen to ensure all samples were exposed to similar aqueous geochemical conditions, and to evaluate whether differences in proton or metal adsorption behavior exist between closely-related mat samples. Acid-base titrations were performed in two ways: first, after acid-leach experiments aimed at removing

surface adsorbed metals and saturating functional groups with protons for quantification of proton-reactive organic ligands, and second, after rinse in only titration electrolyte adjusted to spring pH to evaluate titratable charges not limited to the mat samples' organic components.

In the first case, organic functional group concentrations and acidity constants proved comparable to values reported for cyanobacterial laboratory cultures. This is particularly significant as cyanobacteria are one of the most important primary producers of organic matter, a fact that speaks strongly to the widespread applicability of the findings presented here. A caveat exists, however, in that only benthic cyanobacteria were examined in Chapter 2 owing the limited locales (e.g., hot springs) where natural cyanobacteria may be readily collected in appreciable quantities. In terms of global importance, marine cyanobacteria are an obvious target for future research as they account for upwards of 60% marine biological CO_2 fixation (Jardillier et al., 2010), and differences in surface chemical reactivity between benthic and planktonic cyanobacterial species has been previously noted (e.g., Fattom and Shilo, 1984). Future experiments might employ flow-cytometry cell sorting to isolate cyanobacterial populations from seawater (e.g., Jardillier et al., 2010) for the purposes of acid-base titration, however the feasibility of such an effort is largely unexplored.

In the second case, samples that were merely rinsed showed acid-base behavior dominated by a singular and abundant proton-reactive moiety that was most likely inorganic mat-hosted aqueous or mineral carbonate. Significant variability between samples in total proton-reactive ligand concentrations was observed for both preparations. Partition coefficients derived from acid-leach experimental data reveal preferential sequestration of divalent metal cations by the mats, and a linear free energy approach was employed in an attempt to determine the relative roles of aqueous carbonate complexation, carbonate mineral precipitation, and organic complexation by carboxyl functional groups in divalent cation sequestration. Partition coefficients for these elements were observed to approximately correlate with both their respective carbonate solubility products and aqueous carboxyl (oxalate) stability constants; this feature is not surprising

considering the chemical homology between carboxyl and carbonate functional groups, but complicates the identification of trace element adsorption processes by organic matter as they occur from alkaline or other carbonate-rich waters. Issues pertaining to the actual fate of metals within the mats may be resolved by the application of micro-scale techniques more sensitive to coordination environment (e.g., synchroton X-ray adsorption spectroscopy), or more discriminant on the basis of mass differences (e.g., secondary ion mass spectrometry). Such techniques represent the logical approach to the problem raised by the linear free-energy correlation reported here, and are strongly recommended for the future study of metal partitioning in natural cyanobacterial mats.

As described in Chapter 3, microbial mats of *Cyanidia* sp. red algae and *Hydrogenobaculum* sp. chemolithoautotrophic bacteria, along with authigenic hydrous ferric oxides (HFO), were collected from two acid-sulfate-chloride springs and a neutral-sulfate-chloride spring in the Norris Geyser Basin area of YNP. Acid-base titration of biomass material indicated proton-reactive surface site densities (over the pH 4-10 range) that were significantly lower for the bacterial samples relative to *Cyanidia*, although both proved within an order of magnitude of literature values for laboratory cultures. While the unusually low surface site density of the *Hydrogenobaculum* bacterial mat appears at odds with reported values for most laboratory bacterial cultures, it is in accordance with the only available previous work using a related laboratory strain from the order *Aquificales* where unusually low total site densities were also reported (Lalonde et al., 2005). While additional work is clearly required, these findings add to amassing evidence that there exists significant variation in surface chemical reactivity across the microbial biosphere.

Additional titration of *Cyanidia* mat material after leaching experiments revealed a significant increase in reactive sites only at a –log acidity constant (pK_a) around 7; considering a corresponding abundance of Mg preferentially released by the leaching procedure, this is hypothesized to reflect the release of surface-adsorbed Mg, or potentially disruption of the cell wall by the release of Mg that may play a structural charge-bridging role. As with the cyanobacterial mats

described in Chapter 2, adsorbed metal concentrations also scaled with inferred site concentrations for all samples. Remarkably, organic matter and HFO substrates from the same spring showed elemental partitioning from spring waters that was comparable, with a few notable exceptions. While the HFO material is characterized by a low organic content (<1%), it is not unreasonable that an adsorbed, nano-scale organic coating may have been present at the outermost water-HFO interface; again, the application of micro-scale mass or electromagnetic spectroscopy would have provided additional insight into the physical fate of metals at the HFO surface and shed some light on the striking similarity between organic and HFO surfaces in terms of sorbed metals. In a comparison of hydrous ferric oxides between the three springs, forward surface complexation models based on stream geochemistry, acid-base titration results, and literature HFO metal stability constants were evaluated for agreement with measured adsorbed ion loads. While there was general agreement between measured values and model predictions for many elements, it was determined that the HFO samples formed under neutral-sulfate conditions were characterized by surface chemistry that was significantly different than typical HFO, likely owing to its formation as a co-precipitate with significant amounts of SiO_2.

These results have important implications for our understanding of the role of microbial biomass in metal adsorption and mineral nucleation. First, these results confirm over a decade of independent laboratory investigations into the nature and abundance of proton-reactive functional groups at the cell surface. Not only are the diverse YNP microbial communities examined herein comparable to laboratory cultures (e.g., within an order of magnitude) in terms of the concentration of reactive surface sites, but they show acid-base buffering behaviour and a distribution of acidity constants that is broadly equivalent. This fundamental confirmation provides critical support for the applicability of laboratory microbial metal adsorption and mineral nucleation data to the natural environment. However, subtle differences in microbial surface reactivity between communities are apparently manifest in elemental partitioning, as evidenced in both chapters. This finding has bearing on whether there truly exists "universal" metal adsorption

behavior for any given element across the microbial biosphere, an idea heavily promoted by some (e.g., Yee and Fein, 2001; Borrok et al., 2004) but contradicted here. One possible reason for this discrepancy may by the high biomass-to-metal ratios that are typical of experimental studies but unrealistic of natural environments; under such conditions, available adsorption sites may be in such excess that only one functional group type (specifically, acidic carboxyl) is required to wholly account for metal adsorption. In this case, the relative importance of functional groups with metal adsorption edges at higher pH is minimized; this is in contrast to natural conditions where sorbates would be in excess and reactions involving all available sites account for metal adsorption. In the case of acid-base titration, aqueous protons are well in excess of available surface sites over most of the titration range, such that experiments are limited by the detection of a small number of discrete sites, as opposed to saturation of a single site as may be the case of metal adsorption. The fact that significant variations in adsorbed metal loads are reported here for natural biomass in both Chapters 2 and 3 indicate that there is significant progress to be made with regards to the applicability of metal adsorption experiments performed with laboratory cultures towards biomass in natural settings. Future laboratory experiments of metal adsorption to microbial biomass employing multi-element solutions that more closely mimic natural waters, and perhaps flow-through reactor experiments to eliminate limitations imposed by batch conditions, should help further close the knowledge gap between laboratory experiments and natural processes.

5.2 Surface chemical reactivity of Terebellid worm mucus

The production of mucus is feature widely expressed across the animal kingdom. Composed primarily of high molecular weight glycoproteins belonging to the mucin family, mucus appears largely conserved despite the variety of functions it performs (Bavington et al., 2004). In bioturbated sediments, mucus is frequently employed to stabilize animal burrows to the point where it effectively constitutes the outermost layer of the sediment-water interface. This interface is the site of intense chemical exchange in many natural systems. Natural bioturbated sediments

have demonstrated metal enrichments of 2-4 times over unbioturbated control samples, and despite some grain-size sorting effects on trace element contents, metal enrichment appears to largely stem from adsorption to, and degradation of, natural organic matter within the burrows (Over, 1990). Selective carbonate mineralization (e.g., Gingras et al., 2004; Zorn et al., 2007) and metal concretion formation (Zorn et al., 2007) within relict burrows further highlight the influence of bioturbating animals on chemistry at the sediment water interface. While adsorption by organic matter represents an important sedimentary sink for many trace elements (e.g., Bryan and Langston, 1992), the chemical adsorptive properties of many naturally-abundant organic materials, including animal mucus, have remained unexplored. Chapter 4 details experiments that represent the first examination of the identity, concentration, and metal affinity of proton-reactive functional groups located on animal mucus burrow linings.

Terebellid polychaete worms were collected from the British Columbia coast and incubated in a circulating salt-water tank in a variety of media chosen to promote burrow construction, including clean quartz sand, open-ended PVC tubing, and round-bottom glass test tubes; only open-ended PVC tubing stimulated the construction of mucus-lined burrows. Burrow material was physically cleaned, rinsed with deionised water, and subject to FTIR spectroscopy, compositional analysis, acid-base titration and Cd adsorption assays. FTIR spectroscopy revealed spectral features most consistent with sulfonated glycoprotein, and in particular, indicated significant chemical homology with the glycoprotein mucin, a major component of mucus deriving from animals ranging from echinoderms to mammals. Individual proton-reactive functional group concentrations were quantified by acid-base titration; the mucus material possesses a total surface site concentration of 11.26±1.79 mmol per dry gram that is proton reactive over the pH 4-10, which is nearly double that of previously-studied humic substances and microbial biomass. The presence of abundant chalcophilic thiol functional groups responsible in part for mucin's adhesive properties confer strong reactivity towards dissolved Cd in animal mucus. It is interesting to speculate that the adsorption of aqueous metals or other seawater components may reduce mucus adhesivity

through competition for sulfonated functional groups; the relative adhesivity of mucins from animals from aqueous environments of significantly different metal or ion loads (e.g., freshwater vs. marine) warrants further investigation. If such aqueous competition proved to be important in determining the adhesive properties of mucin, this may have significant implications for the compositional and functional evolution of mucin from its origins in primitive protozoa to its ubiquity in more complex animal life.

Collectively, these results firmly place animal mucus secretions on par with other well-characterized organic matter sorbents in terms of adsorptive capacity and dissolved metal reactivity. These results are particularly interesting with respect to implications for selective mineral nucleation, elemental enrichment, and diagenesis processes observed in bioturbated fabrics (e.g., Gingras et al., 2004). Not only does mucus production by bioturbating organisms locally concentrate organic carbon and promote the development of burrow-hosted microbial communities (e.g., Aller and Aller, 1986), but it would also efficiently concentrate and sequester dissolved ions from ambient waters into burrow walls. Additional studies examining whether pronounced specificity typifies ion adsorption by animal mucus, or whether relative ion affinity follows traditional ordering (such as the Irving-Williams series), may provide future insight into cryptic physiological roles. Equally interesting is the idea that evidence for metal adsorption reactions occurring onto burrow mucus material may be distinguished in contemporary and ancient bioturbated sediments by the examination of relationships between sediment partition coefficients, known organic compound stability constants, and mineral solubility products, as was employed in Chapter 2 for trace elements concentrated by natural cyanobacterial mats. The choice of carbonate-poor siliciclastic sediments would facilitate the recognition of geochemical signatures deriving from mucus and other organic matter adsorption processes by eliminating the issue of homology in coordination between carbonate and carboxyl identified in Chapter 2. Such future studies would also strongly benefit from the application of micro-scale techniques sensitive to coordination environment or subtle mass differences of metal-bearing compounds, as discussed above. While initial results

from commercially-available purified porcine gastric mucin (Petrash et al., in prep.) support the composition, proton and cadmium reactivity reported herein, further examination and comparison with additional animal mucus secretions is clearly warranted.

5.3 Natural iron oxides and implications for ocean chemistry during the deposition of Precambrian iron formations

In some cases, highly parameterized surface complexation models may not be practical for the description of natural systems; critical information such as specific surface area and site density may be difficult to determine. Instead, lumped-process distribution coefficients, based on the Freundlich isotherm approach, are often applied. The distribution coefficient approach, which employs a linear or exponential relationship to describe the distribution of a trace element between solid and solution, benefits from simplicity and ease of execution, but is limited to the particular aqueous conditions (fixed pH, ionic strength) for which it is employed (Langmuir, 1997). Nonetheless, as we shall see below, distribution coefficient models have proven effective for the description of trace element sequestration by natural iron oxides, especially in marine systems (e.g. Feely et al., 1998; Edmonds and German, 2004).

Only recently have attempts been made to apply predictive adsorption models to ancient iron oxide deposits for the purposes of exploring evolving seawater chemistry (e.g., Bjerrum and Canfield, 2002). Efforts to date have focused on iron formations (IF), ancient iron- and silica- rich (~20-40 wt% and ~40-60 wt%, respectively) chemical sedimentary deposits largely devoid of detrital input that constitute one of the most persistent records of the Precambrian marine environment (see Klein, 2005 for an excellent review). Throughout the Precambrian, anoxic conditions promoted the accumulation of dissolved Fe in seawater and the precipitation of iron oxides over large areas of the seafloor. It is often overlooked that oceans also had a significantly higher concentration of dissolved silica, at least as high as at saturation with cristobalite (0.67 mM at 40°C in seawater), and possibly even amorphous silica (2.20 mM) (Maliva et al., 2005).

Silica concentrations close to or at saturation with respect to amorphous silica likely persisted until the early Cretaceous, when the disappearance of VMS-associated hematitic jasper deposits indicate that diatoms or other silica-secreting organisms began actively scavenging silica (Grenne and Slack, 2003), eventually to reduce its concentration to a modern average that is less than 0.10 mM (Tréguer et al., 1995). Crucially, silica strongly adsorbs to iron oxides and effectively competes with phosphate for available iron oxides adsorption sites.

This is demonstrated experimentally in Appendix 1, where a revised K_D approach accounting for iron-silica co-precipitation indicates that with sufficiently high silica concentrations, the scavenging of phosphate by iron-rich hydrothermal fluid precipitates is minimal. The IF phosphorus record, interpreted in this light, indicates that phosphate was likely more abundant in Precambrian oceans than today. Appendix 1 highlights the promise held by partition coefficient models, and models based on knowledge of adsorption processes in general, for the exploration of marine paleo-proxies derived from IF and other chemical sedimentary formations where adsorption reactions were important. A similar approach is employed in Appendix 2, where the history of marine Ni is evaluated from the IF rock record and Ni partitioning experiments accounting for the role of dissolved silica. Dissolved marine Ni concentrations appear to have declined significantly around 2.7 Ga, which is attributed to cooling of the upper continental crust and a shift away from ultramafic Ni-rich sources in the chemical weathering budget. These results have strong potential implications for evolution of the microbial biosphere, especially for methanogenic Archea with unusually high Ni requirements, as well as for the timing of atmospheric oxygenation, stemming from the importance of biogenic methane in the atmospheric redox budget.

5.4 References

Aller, J.Y., Aller, R.C., 1986. Evidence for localized enhancement of biological activity associated with tube and burrow structures in deep-sea sediments at the HEBBLE site, western North Atlantic. *Deep Sea Res Part A* **33**, 755-790 (1986).

Bavington, C.D., Lever, R., Mulloy, B., Grundy, M.M., Page, C.P, Richardson, N.V., and McKenzie, J.D. Anti-adhesive glycoproteins in echinoderm mucus secretions. *Comp. Biochem. Physiol. Part B: Biochem. Mol. Biol.* **138**, 607-617 (2004).

Bjerrum, C.J. and Canfield, D.E. Ocean productivity before about 1.9 Gyr ago limited by phosphorus adsorption onto iron oxides. *Nature* **419**, 159-162 (2002).

Borrok, D., Fein, J.B., and Kulpa, C.F. Proton and Cd adsorption onto natural bacterial consortia: testing universal adsorption behavior. *Geochimica et Cosmochimica Acta* **68**, 3231-3238 (2004).

Bryan, G.W. and Langston, W.J. Bioavailability, accumulation and effects of heavy metals in sediments with special reference to United Kingdom estuaries: a review. *Environmental Pollution* **76**, 89-131 (1992).

Fattom, A. and Shilo, M. Hydrophobicity as an adhesion mechanism of benthic cyanobacteria. *Applied and Environmental Microbiology* **47**, 135-143 (1984).

Feely, R.A., Trefry, J.H., Lebon, G.T., and German, C.R. The relationship between P/Fe and V/Fe ratios in hydrothermal precipitates and dissolved phosphate in seawater. *Geophysical Research Letters* **25**, 2253-2256 (1998).

Fein, J.B., Daughney, C.J., Yee, N., and Davis, T.A. A chemical equilibrium model for metal adsorption onto bacterial surfaces. *Geochimica et Cosmochimica Acta* **61**, 3319-3328 (1997).

Grenne, T., and Slack, J.F. Paleozoic and Mesozoic silica-rich seawater: Evidence from hematitic chert (jasper) deposits. *Geology* **31**, 319-322 (2003).

Gingras, M.K. Pemberton, S.G., Muelenbachs, K., and Machel, H. Conceptual models for burrow-related, selective dolomitization with textural and isotopic evidence from the Tyndall Stone, Canada. *Geobiology* **2**, 21-30 (2004).

Jardillier, L., Zubkov, M.V., Pearman, J., and Scanlan, D.J. Significant CO2 fixation by small prymnesiophytes in the subtropical and tropical northeast Atlantic Ocean. *International Society for Microbial Ecology Journal* **4**, 1180-1192 (2010).

Klein, C. Some Precambrian banded iron-formations (BIFs) from around the world: Their age, geologic setting, mineralogy, metamorphism, geochemistry, and origin. *American Mineralogist* **90**, 1473-1499 (2005).

Lalonde, S.V., Konhauser, K.O., Reysenbach, A.-L., and Ferris, F.G. The experimental silicfication of Aquificales and their role in hot spring sinter formation. *Geobiology* **3**, 41-52 (2005).

Maliva, R.G., Knoll, A.H., and Simonson, B.M. Secular change in the Precambrian silica cycle: insights from chert petrology. *Geological Society of America Bulletin* **117**, 835-845 (2005).

Over, D. Trace metals in burrow walls and sediments, Georgia Bight, USA. *Ichnos* **1**, 31-41 (1990).

Petrash, D.A., Lalonde, S.V., Konhauser, K.O., in prep. Porcine gastric mucin as a laboratory analog for marine infaunal mucus: FTIR, proton and cadmium adsorption behaviour.

Tréguer, P., Nelson, D.M., Van Bennekom, A.J., DeMaster, D.J., Leynaert, A., and Quéguiner, B. The silica balance in the world ocean: a reestimate. *Science* **268**, 375-379 (1995).

Yee, N. and Fein, J.B. Cd adsorption onto bacterial surfaces: A universal adsorption edge? *Geochimica et Cosmochimica Acta* **65**, 2037-2042 (2001).

Zorn, M.E., Muehlenbachs, K., Gingras, M.K., Konhauser, K.O., Pemberton, S.G., Evoy, R. Stable isotopic analysis reveals evidence for groundwater-sediment-animal interactions in a marginal-marine setting. *Palaios* **22**, 546-553 (2007).

Appendix 1

Was There Really an Archean Phosphate Crisis?[1]

Brevia

During the Archean, when massive amounts of iron were being deposited in the form of banded iron formations (BIF), it has been suggested that sedimenting particles of ferric oxyhydroxide may have stripped dissolved phosphate from the ocean's photic zone (Bjerrum and Canfield, 2002). Hypothesized phosphate concentrations of only 10-25% present-day values would have led to a reduction in phytoplankton productivity, and therefore, to lower rates of oxygen production and organic carbon burial. This model is predicated on the observation that ferric oxyhydroxide particles, resulting from the oxidation of Fe(II) in some modern submarine hydrothermal systems, sorb phosphate with a K_D value of approximately 0.06 μM^{-1} (Feely et al., 1998).

However, unlike the modern ocean, the Archean ocean had significantly higher concentrations of dissolved silica, at least as high as at saturation with cristobalite (0.67 mM at 40°C in seawater), and possibly even amorphous silica (2.20 mM) (Maliva et al., 2005); modern oceans average <0.10 mM (Tréguer et al., 1995). Silica strongly sorbs to ferric oxyhydroxides, and at the proposed concentration of phosphate in the Archean ocean (ranging from 0.03 to 0.29 μM; Bjerrum and Canfield, 2002), silica would effectively compete with phosphate for available sorption sites (based on α-FeOOH relative adsorption constants; Sigg and Stumm, 1981). Furthermore, iron-silica co-precipitation diminishes the resulting particle's point of zero net charge (PZNC) (Schwertmann and Fechter, 1982), rendering it less reactive to dissolved anions.

We determined the significance of high silica concentrations on phosphate sorption in two ways: (i) using pre-formed ferrihydrite particles to demonstrate the

[1]A version of this Appendix has been published. Konhauser KO, Lalonde SV, Amskold L, and Holland HD. *Science* **315**, 1234 (2007).

competitive adsorption between silica and phosphate at different pH values, and (ii) oxidizing Fe(II) to precipitate ferrihydrite, in the presence of silica and phosphate, for the determination of K_D values. In the first instance, maximum phosphate adsorption onto pre-formed ferrihydrite particles occurs at pH<7 and in the absence of silica (Fig. 1A); silica out-competes phosphate as its concentration increases. Furthermore, ferrihydrite incorporating silica shows a consistent decrease in PZNC (Fig. 1B), and correspondingly, adsorbs even less phosphate (stippled lines in Fig. 1A).

Co-precipitation experiments with an initial Fe(II) concentration of 0.2 mM revealed that the presence of silica reduced the phosphate content of the resulting particles (Fig. 1C). In the complete absence of silica, we calculate a K_D value of $0.075 \pm 0.003\ \mu M^{-1}$, similar to the K_D value used by Bjerrum and Canfield (2002) for particles formed at modern submarine hydrothermal vents (cf. Feely et al., 1998), while K_D values decreased to $0.011 \pm 0.004\ \mu M^{-1}$ and $0.002 \pm 0.002\ \mu M^{-1}$ for solutions near cristobalite and amorphous silica saturation, respectively. Additionally, we observed silica to exert an even greater effect at lower dissolved Fe concentrations (0.02 mM Fe, Figure S6). Consequently, our calculated K_D values are conservative at 0.2 mM Fe, especially considering that previous estimates of dissolved Fe concentrations for the Archean ocean are around 0.05 mM (*8*). Only at much higher dissolved Fe concentrations (e.g., ~2 mM), such as in some hydrothermal vent fluids, does the effect of silica on phosphate sorption become negligible (Figure S6).

If we use the P:Fe ratio in BIF as a proxy for dissolved phosphate concentrations in the Archean ocean (as did Bjerrum and Canfield (1998), with whom we compare our data), we calculate that average dissolved phosphate concentrations would have ranged from $0.14 \pm 0.01\ \mu M$ (no silica) to $5.25 \pm 2.63\ \mu M$ in an amorphous silica-saturated ocean. The latter value is of the same order of magnitude as modern oceans (2.3 μM) (Bjerrum and Canfield, 1998). Importantly, there would have been diagenetic re-mobilization of phosphate during burial (probably leading to lower P:Fe ratios in BIF). Thus, the actual dissolved phosphate concentrations could have been even higher. Clearly, if the Archean

ocean contained abundant dissolved silica, as is generally believed, sedimenting ferrihydrite particles would not have been a major sink for phosphate. It is unlikely that there was a phosphate crisis, and a related reduction in phytoplankton productivity, due to BIF deposition in the Archean ocean.

Methods

For adsorption experiments, 2-line ferrihydrite (as determined by XRD) was precipitated from solutions prepared with 1.79 mM $FeCl_2{\cdot}4H_2O$, at circumneutral pH, seawater ionic strength (0.56 M NaCl), and with various concentrations of silica (from 0 – 2.20 mM, added as $Na_2SiO_3{\cdot}9H_2O$). The particles were then rinsed 3 times with 0.56 M NaCl, and re-suspended in 0.56 M 1NaCl to which various concentrations of silica (0 to 2.20 mM) and phosphate (fixed at 21 μM, from 1000 ppm commercial KH_2PO_4 standard) were added. The pH values of all experiments were monitored continuously, and the pH of interest was maintained by the addition of dilute HCl or NaOH. After an experimental duration of 30 minutes (sufficient to reach equilibrium, see supplementary data), samples were filtered (through 0.2 μm nylon in-line syringe filters), and the concentration of phosphate was determined spectrophotometrically by the ascorbic acid technique.

The PZC of freshly prepared ferrihydrite particles (formed in the presence 0 – 2.20 mM silica, as above) was determined from electrophoretic mobility data obtained with a CAD Instrumentation Zetaphoremeter III. Solid phase Si:Fe molar ratios were calculated by measuring aqueous silica loss during precipitation using the spectrophotometric heteropoly blue technique. Particles formed in 0.67 mM SiO_2 solution achieved a solid phase Si:Fe molar ratio of 0.27, while particles formed in 2.20 mM SiO_2 solution achieved a solid phase Si:Fe molar ratio of 1.05.

For the co-precipitation experiments, various concentrations of ferrous iron (0.02 to 2.00 mM) and phosphate (1.0 to 500.0 μM) were added to 0.56 M NaCl solutions prepared at pH 8 and with silica concentrations ranging from 0 to 2.20 mM; pH was maintained for 30 minutes and solutions were sampled and assayed as above. K_D values were calculated from the slope of the trendline that best represents the sorption maxima (i.e., consecutive data points from intercept yielding the highest R^2). Most experiments were conducted at atmospheric O_2, but additional experiments were continuously purged with 99.99% Ar to assess the effects of slower Fe(II) oxidation rates on phosphate sorption. Dissolved iron concentrations were measured spectrophotometrically, using the ferrozine method, to confirm complete oxidation. All experiments were performed at 25°C in acid-

washed glassware with continuous mixing. Further experiments were performed at 60°C, including some with 3.10 mM dissolved silica (the approximate solubility of amorphous silica at that temperature).

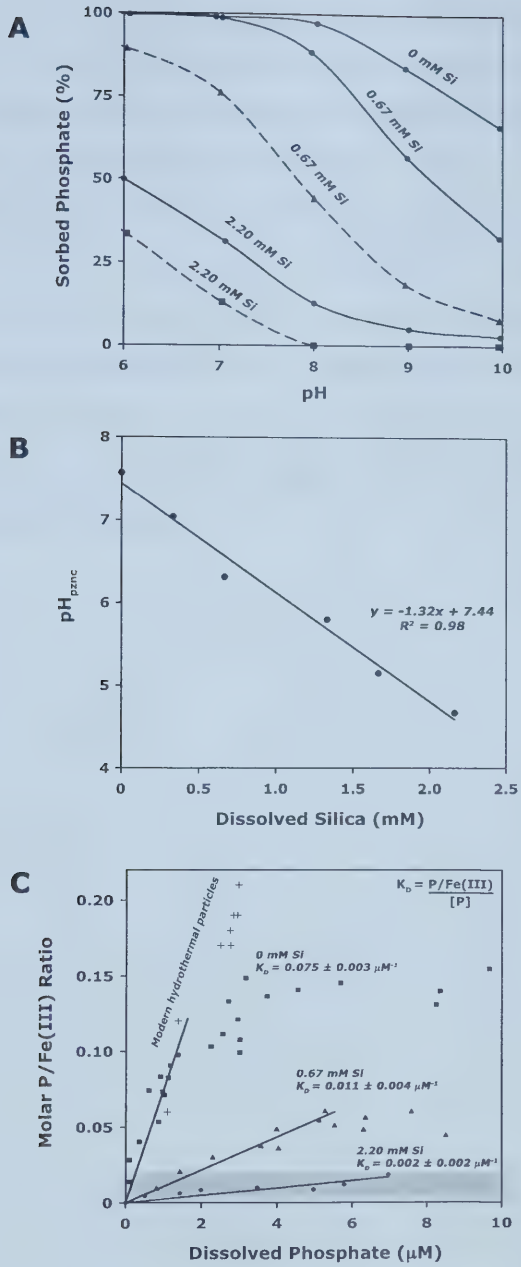

Figure 1. (A) Adsorption isotherms demonstrate, as a function of pH, the competition between silica and phosphate for the surface sites of ferrihydrite (dark lines) and silica-containing ferrihydrite particles (stippled lines); ferrihydrite (circles), particles formed in 0.67 mM SiO_2 (triangles), and particles formed in 2.20 mM SiO_2 (squares). (B) Particles precipitated at various silica concentrations

possess a lower point of zero net charge than 'pure' ferrihydrite as a result of silica incorporation. (C) Co-precipitation experiments performed at pH 8 with 0.2 mM Fe(II) yield K_D values relating solid-phase and dissolved equilibrium phosphate concentrations. As a comparison to our results, data for modern deep-sea hydrothermal plumes (from Feely et al. 1998), and previously used to estimate Archean ocean phosphate concentrations (Bjerrum and Canfield, 1998), are plotted. Also shown are the range of P/Fe(III) values in BIF (grey box; cf. Bjerrum and Canfield, 1998). It is apparent from the co-precipitation data that the particles incorporate decreasing amounts of phosphate with increasing dissolved silica concentrations, and consequently, suggest higher dissolved phosphate concentrations during BIF deposition.

References

Bjerrum, C.J. & Canfield, D.E. *Nature* **417**, 159 (2002).

Feely, R.A., Trefry, J.H., Lebon, G.T., & German, C.R. *Geophys. Res. Lett.* **25**, 2253 (1998).

Holland, H.D. The Chemical Evolution of the Atmosphere and Oceans (1984).

Maliva, R.G., Knoll, A.H, & Simonson, B.M. *Geol. Soc. Am. Bull.* **117**, 835 (2005).

Schwertmann, U. & Fechter, H. *Clay Min.* **17**, 471 (1982).

Sigg, L. & Stumm, W. *Colloids Surf.* **2**, 101 (1981).

Tréguer, P., Nelson, D.M., Van Bennekom, A.J., DeMaster, D.J., Leynaert, A., & Quéguiner, B. *Science* **268**, 375 (1995).

Appendix 2

Oceanic Nickel Depletion and a Methanogen Famine before the Great Oxidation Event[1]

Preamble

It has been suggested that a decrease in atmospheric methane levels triggered the progressive rise of atmospheric oxygen, the so-called Great Oxidation Event, about 2.4 Gyr ago (Zahnle et al., 2006). Oxidative weathering of terrestrial sulphides, increased oceanic sulphate, and the ecological success of sulphate-reducing microorganisms over methanogens has been proposed as a possible cause for the methane collapse (Zahnle et al., 2006), but this explanation is difficult to reconcile with the rock record (Papineau et al., 2007; Scott et al., 2008). Banded iron formations preserve a history of Precambrian oceanic elemental abundance and can provide insights into our understanding of early microbial life and its influence on the evolution of the Earth system (Bjerrum and Canfield, 2002; Konhauser et al., 2007). Here we report a decline in the molar nickel to iron ratio recorded in banded iron formations about 2.7 Gyr ago, which we attribute to a reduced flux of nickel to the oceans, a consequence of cooling upper-mantle temperatures and decreased eruption of nickel-rich ultramafic rocks at the time. We measured nickel partition coefficients between simulated Precambrian seawater and diverse iron hydroxides, and subsequently determined that dissolved nickel concentrations may have reached ~400 nM throughout much of the Archaean eon, but dropped below ~200 nM by 2.5 Gyr ago and to modern day values (~9 nM; Drever, 1988) by ~550 Myr ago. Nickel is a key metal cofactor in several enzymes of methanogens (Jaun and Thauer, 2007) and we propose that its decline would have stifled their activity in the ancient oceans and disrupted the supply of biogenic methane. A

---

[1]A version of this Appendix has been published. Konhauser KO, Pecoits E, Lalonde SV, Papineau D, Nisbet EG, Barley ME, Arndt NT, Zahnle K, and Kamber BS. *Nature* **458**, 750-753 (2009).

decline in biogenic methane production therefore could have occurred before increasing environmental oxygenation and not necessarily be related to it. The enzymatic reliance of methanogens on a diminishing supply of volcanic nickel links mantle evolution to the redox state of the atmosphere.

Letter

Did a nickel famine at the end of the Archaean cause catastrophic collapse of atmospheric methane and thereby facilitate the rise of atmospheric oxygen? At the heart of our hypothesis is the distinct topography in molar Ni/Fe ratios preserved in banded iron formations (BIF) over time (Figure 1; see also Supplementary Figures S1-S3, Supplementary Tables S1-S2). An expanded trace element database for BIF that includes more than 1,200 bulk and grain-by-grain (haematite, magnetite) measurements shows a trend in BIF Ni/Fe ratios that can be defined by two broad stages. Stage 1, which spans from the oldest BIF (~3.8 - 3.7 Gyr) to those as young as 2.7 Gyr, shows a uniform maximum molar Ni/Fe ratio ($\sim 4.5 \times 10^{-4}$). Stage 2, which we demarcate at around 2.5 Gyr ago (the Archaean-Proterozoic boundary), shows strikingly lower maximal Ni/Fe ratios (below 2.2×10^{-4}). The boundary between stages 1 and 2, although at present not well constrained owing to gaps in the BIF record, marks a significant and irreversible decline in oceanic Ni concentrations: stage 1 values are never reached again. Stage 2 is characterized by a further steady decline in maximum Ni/Fe ratios, a trend that persists for the remainder of the Palaeoproterozoic BIF record. It is possible that a third stage exists, post-dating a resurgence in BIF deposition between 0.75 and 0.55 Gyr ago, but the scarcity of Neoproterozoic BIF trace element data precludes any further conclusion at present.

The transition from stage 1 to stage 2 is unlikely to have been driven by changes in Ni sinks, which appear to be relatively insensitive to evolving major element and redox conditions from Archaean-Palaeoproterozoic ferrous iron seas, through Mesoproterozoic sulphidic seas, to the onset of oxygenated bottom waters in the Neoproterozoic (Saito et al., 2003; their Fig. 4). Moreover, Fe^{2+} and Ni^{2+} show similar behaviour with increasing sulphide concentrations, indicating that the

presence of sulphide will not lead to chemical fractionation between the two metals (Saito et al., 2003; their Fig. 2). In this regard, sulphide is not a major sink for Ni except for some magmatic sulphides (Öztürk, 1995 and references therein), and unlike Cu-Zn-Au, which are abundant in Precambrian volcanogenic massive sulphide deposits (Hannington et al., 2004), there are no accumulations that would indicate sequestration of Ni into the sea floor of a sulphidic ocean (Keays, 1995). The trends in our data also appear independent of oxidative mechanism or depositional environment. The prominent decline in molar Ni/Fe ratio is recorded in pre-Great Oxidation Event BIF (Figure S3) that appear to have been deposited in waters of greater than 200 m depth (Trendall, 2002). During stage 2, so-called granular iron formations of the circum-Ungava belt of North America (for example, the 1.88 Gyr Gunflint Formation) formed in shallow-water, high-energy environments (Trendall, 2002), yet they show no discernable difference in Ni/Fe ratios from deep-water stage 2 BIF (for example, the 0.55 Gyr Yerbal Formation).

In contrast, Ni supply probably changed significantly with time. First, a hotter Archaean mantle (Berry et al., 2008) produced abundant Ni-rich komatiite and olivine-rich basalt in oceanic crust, plateaus, and perhaps on land (Barley et al., 1998; Kamber et al., 2005). Second, Archaean tholeiites, which made up most of the oceanic crust, were richer in Ni than their modern counterparts (Arndt, 1991). Third, a major peak in preserved komatiite abundance occurred during the most intense period of mantle plume magmatism and continental crustal growth in Earth's history, between 2.72 and 2.66 Gyr ago (Barley et al., 1998; Barley et al., 2005), after which their abundance decreased rapidly (see Figure S4; Table S3). All of the above factors are related to the extent of mantle source melting and temperature (Nisbet, 1982), whose evolution can be reconstructed from the composition of mafic magmas (Figure 1 inset; Arndt et al., 2008). The hotter Archaean mantle produced more Ni-rich ultramafic rocks, resulting in a much greater supply of Ni than any time thereafter, a fact reflected in the similarity between the lava eruption temperature versus age curve and the molar Ni/Fe ratio of BIF. Nickel preserved in BIF was almost certainly supplied in dissolved form, as opposed to particulate material (that is, volcanic ash or clastic sediment).

Supporting this are low concentrations of lithophile elements in BIF samples selected for this study (see Methods). Furthermore, the Cr/Ni ratios in Archaean BIF are lower than in Archaean basalts, komatiites and shales (Figure S5) which implies Ni mobilization during chemical weathering and hydrothermal alteration of Ni-bearing minerals and preferential supply of Ni (over Cr) to the ocean. Correspondingly, chemical analysis of Archaean basalt-derived palaeosols show accumulation of Cr and loss of Ni in their weathering profiles (see arrow, Figure S5).

The chemical archive preserved in BIF can be exploited using the predictable nature of adsorption reactions occurring at the surface of the authigenic hydrous ferric oxides (HFO) that would have originally precipitated from, and equilibrated with, contemporaneous seawater (see Supplementary Discussion). In natural systems, where trace element sequestration by HFO results from a continuum of adsorption and co-precipitation reactions, lumped-process distribution coefficient models can be used to relate the concentration of an element in the precipitate to the dissolved concentration present at the time of precipitation. In fact, this predictive aspect of HFO sorption reactions has been used to better understand the BIF record with respect to limitations on Precambrian primary productivity that may have arisen via HFO sequestration of bio-essential nutrients (Bjerrum and Canfield, 1998; Konhauser et al., 2007).

Nickel partition coefficients were determined for HFO precipitated in the presence of dissolved silica (Figure 2). Assumptions made in our experiments and extrapolation include an ocean pH of 7–8, ionic strength ~0.5 M, seawater Si/Fe molar ratios of ~12/1 (as per Konhauser et al., 2007), and minimal remobilization of Ni during post-depositional diagenesis and/or metamorphism (see Supplementary Discussion). The experimentally determined partition coefficients allow a first-order estimation of the evolution of seawater Ni concentration from the solid-phase BIF data presented in this study. Figure 2 displays approximately linear relationships between dissolved Ni and the Ni/Fe ratio in the various HFOs examined, consistent with dissolved Ni concentrations well below those

approaching site saturation for these particles. Different amounts of dissolved silica, which was added to the experiments to simulate waters at saturation with respect to cristobalite (0.67 mM) or amorphous silica (2.20 mM), had a pronounced effect on HFO reactivity (see Methods for the rationale of these silica concentrations). As Fe(III) hydrolyses and precipitates at circum-neutral pH, dissolved silica is incorporated into the particles, altering their surface properties, and also directly out-competing other dissolved ions for adsorption sites[5]. Using the Si-rich particles as the best proxy for particle composition in the Archaean, extrapolated dissolved Ni concentrations (Figure 3) suggest that BIF record a drastic reduction in dissolved Ni, from values as high as ~400 nM to values no greater than 200 nM during the transition from stage 1 to stage 2; stage 2 shows a gradual decline to <50 nM by 0.7 Gyr ago, with modern ocean values reached some time after 0.55 Gyr ago. Although it is difficult to quantify the uncertainty in our extrapolation from HFO sorption experiments to the ancient oceans, we feel that this approach is the best currently available for estimating palaeo-ocean Ni concentration. Moreover, we have deliberately taken a conservative approach, as any Ni loss that might have occurred during post-depositional alteration of HFO would lead to an underestimate of oceanic Ni concentrations.

Our finding of nickel-rich Archaean oceans has immediate implications for microbial life that requires it as a trace element. It has been previously suggested that nickel-containing enzymes are remnants from an early period in microbial evolution when nickel was abundant (da Silva and Williams, 1991). Specifically, methanogens require Ni for the synthesis of three different [NiFe]-hydrogenases, carbon monoxide dehydrogenase, acetyl-CoA synthase/decarbonylase, and methyl-coenzyme M reductase (MCR), the latter being the catalyst of the final methane-forming step (Jaun and Thauer, 2007). These nickel enzymes are present in high concentrations, with MCR accounting for approximately 10% of methanogen cytoplasmic proteins. Crucially, although methanogens may continue to grow in the absence of Ni (although some have reported cell autolysis when Ni is absent; Jarrell et al., 1982), the synthesis of co-factor F_{430}, the numbers of methanogen cells, and methane production all depend strongly on dissolved Ni availability. For

example, co-factor F_{430} content on a per-cell basis increases with Ni concentrations over a 75–2,500 nM range (Diekert et al., 1980), whereas methanogen cell numbers are strongly Ni-limited at concentrations below 100 nM (Schönheit et al., 1979). Similarly, it has been demonstrated (Kida et al., 2001) that methane production in continuous culture decreased progressively when Ni concentrations were reduced from 8,500 nM to 250 nM, the lowest concentration examined by these authors. Not surprisingly, the addition of Ni has been shown to increase the production of methane from mineral-poor peat samples, waste-water treatment facilities, and sewage sludge (e.g., Basiliko and Yavitt, 2001). To put this into perspective, our data indicate that methanogenesis in the bulk oceans would have been Ni-stimulated throughout stage 1, and especially sensitive to plummeting Ni concentrations over the stage 1 to stage 2 transition, after which it remained in a state of strong Ni-limitation to the present day. Interestingly, methanogens do not appear to have abandoned their overall Ni dependency in the face of this famine (although some can produce nickel-free hydrogenases; see Shima and Thauer, 2007, for review), perhaps because the biochemical re-tooling of so many energy-yielding metalloenzymes that are central to their metabolism was an obstacle too great to overcome. Cyanobacteria appear to have coped with changing metal availability over time by evolving metal-specific ligands (e.g., Saito et al., 2003), but recent studies with methanogens have shown that they do not appear to produce Ni-specific ligands (Hausrath et al., 2007). This may be due to (1) the relatively high solubility of Ni under both oxic and anoxic conditions (Saito et al., 2003), (2) the potentially high cost of ligand production (Hausrath et al., 2007), and (3) a lack of strong competition for Ni with other microorganisms. The fact that nickel concentrations in modern ocean surface waters are not as depleted as other bioactive metals (Saito et al., 2004) may indicate that the microbes that need it most can no longer access it due to the presence of oxygen.

Compounding this Ni famine would be waning fluxes of H_2 (their preferred reductant) with decreasing serpentinization of the sea floor (that is, $2Mg_{1.8}Fe_{0.2}SiO_4 + 2.933H_2O \Leftrightarrow Mg_{2.7}Fe_{0.3}Si_2O_5(OH)_4 + 0.9Mg(OH)_2 + 0.033Fe_3O_4 + 0.033H_2$) accompanying the decrease in production of olivine-rich oceanic crust at the end of

the 2.7-Gyr mantle plume event and the concomitant growth and stabilization of continental cratons (Barley et al., 1998; Barley et al., 2005). It has been argued that the shift from predominantly submarine volcanism to more subaerial volcanism further decreased abiotic H_2 fluxes because the latter yield more oxidized gases (H_2O, CO_2 and SO_2)(Kump and Barley, 2007). In either case, a loss of H_2 would probably have contributed to a declining biogenic methane supply (Kharecha et al., 2005).

A drop in atmospheric methane around 2.4 Gyr ago has been invoked as the most parsimonious explanation for the onset of major Palaeoproterozoic glaciations, the ensuing demise of sulphur isotope mass-independent fractionation, and the progressive rise of atmospheric oxygen (Zahnle et al., 2006). Those authors hypothesized that the biogenic methane flux would have waned owing to increasing competition between methanogens and sulphate-reducing microorganisms before 2.4 Gyr ago. Moreover, anaerobic oxidation of methane, a nickel-dependent process involving *Archaea* that appear to possess a variant of MCR that operates in reverse (Krüger et al., 2003), would further have reduced methane escape with increasing sulphate concentrations at that time (Caitling et al., 2007). However, it is not until after the Great Oxidation Event that evidence in the rock record exists for pervasive oxidative weathering of terrestrial sulphides, a large oceanic sulphate pool, and the onset of widespread ocean euxinia (e.g., Papineau et al., 2007; Scott et al., 2008). We provide an alternative hypothesis, suggesting that the demise in large-scale methanogenesis occurred before, and was not necessarily related to, increasing environmental oxygenation. Our model provides a clear directionality in the evolution of the Earth's system, whereby a cooler mantle following the 2.7 Gyr event led to associated chemical changes in volcanism and trace element abundances in the oceans, triggering a decline in global methanogenesis, and ultimately facilitating the transition from anoxic to oxic atmospheric conditions some 2.4 Gyr ago. Thereafter, increased O_2 would have led to a larger oceanic sulphate pool, the end result being the marginalization of methanogens to anoxic and sulphate-poor niches, as is the case today.

Methods

Sample selection

High abundances of Ni have been recorded in several Archaean clastic sedimentary rocks, and have generally been explained by the presence of an ultramafic dominated crustal source (e.g., McLennan et al., 1983; Taylor and McLennan, 1985). Average compositions of post-Archaean clastic sedimentary rocks define a progressive decrease in Ni concentrations through time, which is clearly related to a compositional change in the upper continental crust (Condie, 1993). Even though this decrease parallels the trend recorded in BIF, both in time and Ni/Fe concentration, reliable authigenic trace metal contents can be compromised by contamination with siliciclastic or volcanic inputs. Therefore, our interpretation of the Ni signal in BIF as a genuine reflection of palaeoseawater required a pre-selection of BIF samples with minimal detrital influence based on chemical composition (as below).

One method commonly used to differentiate detritally sourced components versus authigenic precipitation is through measurement of incompatible, immobile elements such as Al, Ti, Zr, Th, Hf, and Sc (Chester, 2000). Thus, data presented in Tables S1-S2 were selected according to the following criteria: (1) <1 wt% Al, (2) low concentrations (<20 p.p.m.) of Ti, Zr, Th, Hf and Sc, and (3) on the basis of lack of co-variations of Zr versus Y/Ho; Y/Ho versus Ce/Ce*; and Th versus La/La* (e.g., McLennan, 1989; Kamber and Webb, 2001). Furthermore, samples noted or reported to contain sulphides were avoided, to minimize the influence of post-depositional hydrothermal activity on our data set. Through the use of these filters, we are confident that our BIF samples reflect precipitation from sea water.

Ni analyses in BIF

Data are presented in Table S1. Selected BIF samples for geochemical analyses include both drill core and hand samples from fresh exposures. Oxidized surfaces, veins and samples with pyrite were avoided to minimize the effects of weathering and post-depositional overprinting.

For bulk trace element analyses, samples were cut into slabs and broken into small chips (<5 mm) without metal contact. Subsequently, between 20 and 150 g of the material was powdered in an automated agate mill. Crushed rock powders (<100 mesh) were completely dissolved with heated $HF+HNO_3$ and analysed using a Perkin Elmer Elan6000 Quad-ICP-MS (quadrupole inductively coupled plasma mass spectrometer). Accuracy and precision of the analytical protocol were verified with the use of well-established international whole rock standards (for example, BE-N Basalt, CRPG Nancy; see http://research.eas.ualberta.ca/rif/quad_icp_ms.html).

In situ trace element analyses were performed on haematite and magnetite grains using a quadrupole ICP-MS coupled to a laser ablation system (spot size 20–60 mm in diameter). Haematite was chosen as proxy for the original precipitates as it probably formed from dehydration of hydrous ferric oxide (HFO) precursors, and it provides a means of direct comparison between BIF samples of significantly different bulk composition. As magnetite is generally regarded as a secondary iron oxide phase formed by partial reduction of HFO or haematite, we used it to assess post-depositional Ni/Fe disturbances. In this regard, no significant differences between the two iron oxide minerals were observed.

Optimization of ICP-MS instrument parameters (RF power 1,200 W, peak hopping acquisition, 50 ms dwell time) were achieved by ablating either the NIST SRM 610 (~500 p.p.m.) or NIST SRM 612 (~50 p.p.m.) international glass standards. For quantitative trace element determinations, the NIST 610 (for 20 mm spot size) and 612 (for 60 mm spot size) standards and BIF samples were ablated using identical conditions with spot sizes of either 20 mm or 60 mm, 5 Hz repetition rate and energy density of ~13 J cm^{-2}. Quantitative results were obtained via the calibration of relative element sensitivities against the NIST 610 and 612 standards, while Fe values from electron microprobe analyses (JOEL 8900, University of Alberta) were used as internal standards. Data reduction and concentration determinations were obtained using the GLITTER (XP version, New Wave Research) laser ablation software. Repeated analysis ($n = 10$) of the NIST

612 using a 60 mm spot size yielded relative standard deviations of between 5 and 15% (2*s* level) and detection limits between 0.2 (for example, Cu) and 3 p.p.m. (for example, Cr) for most elements (except for P ~13 p.p.m., Fe ~20 p.p.m. and Ca ~165 p.p.m.). All new BIF measurements reported here were performed in the Radiogenic Isotope Facility at the Department of Earth and Atmospheric Sciences, University of Alberta.

Statistical treatment of the data are outlined in Table S2, and graphically presented in Figures S1-3. Ni values were normalized on a molar ratio basis to total Fe for all bulk and laser-ablation analyses because (1) the similar Ni/Fe values observed between individual haematite and magnetite grains indicates that we cannot exclude Fe(II)-containing phases as significant sources of Ni, and (2) many of the published bulk analyses do not discriminate between Fe(II) and Fe(III).

Ni partitioning experiments

Concentrated ferrous iron stock solutions (0.1074 M) were freshly prepared at pH ~3 from ferrous ammonium sulphate hexahydrate and diluted to 0.179 mM in pH 7 receiving solutions consisting of 0.5 M $NaNO_3$ and various amounts of silica (0, 0.67 mM and 2.20 mM, added as sodium metasilicate nonahydrate) and dissolved nickel (0–4,000 nM). These dissolved silica concentrations were chosen to span conditions ranging from as high as amorphous silica saturation (2.20 mM), to cristobalite saturation (0.67 mM), and to modern oceans largely stripped of dissolved silica, in order to explore the effects of dissolved silica on Ni partitioning to iron oxides through time. The oceans were at least saturated with cristobalite, and probably amorphous silica, before 1.8 Gyr ago (Maliva et al., 2005), only to achieve modern values in the Phanerozoic (<0.10 mM; Tréguer et al., 1995) with the advent of silica-secreting eukaryotes.

Dissolved nickel was sourced from a 1,000 p.p.m. Ni commercial ICP-MS standard (in 2% HNO_3, SPEX CertiPrep). All experiments were performed at ~23 °C in acid-washed glassware with continuous mixing. The pH values of all experiments were monitored continuously and maintained at pH 7 by the addition of dilute HCl or NaOH. After an Fe(II) oxidation and equilibration period of

30 min, samples were filtered through 0.2 μm nylon in-line syringe filters, acidified with trace-metal grade HNO_3, and analysed within one week for Ni, as well as for Fe (to confirm complete oxidation and precipitation), by ICP-MS (Perkin Elmer Elan6000) at the University of Alberta.

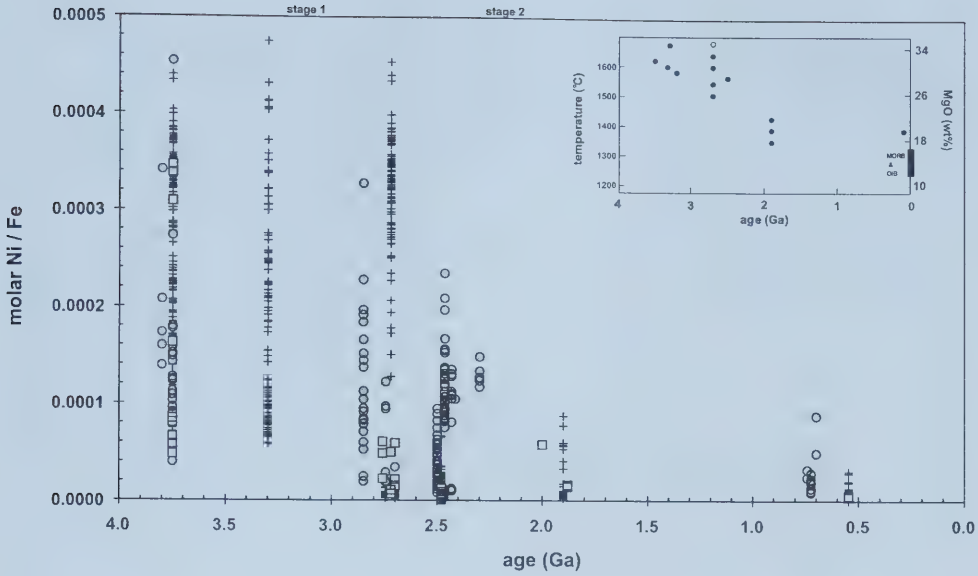

Figure 1. Ni/Fe mole ratios for BIF versus age, and properties of parental komatiite liquids. The figure contains 1,214 measurements, including literature data (circles) and our new bulk (squares) and grain-by-grain laser ablation analyses (crosses). Two stages are identified based on maximal Ni/Fe ratios, with the transition period indicated by a grey bar. Inset, maximum MgO contents inferred for the parental komatiite liquids (Arndt et al., 2008), and the probable eruption temperatures, plotted (filled circles) as a function of age. Eruption temperatures T were calculated using the relation $T = 1{,}000 + 20\text{MgO}$ (where T is in °C, and MgO in wt%; Nisbet, 1982), assuming essentially anhydrous magmas. Open circle, recent data by Berry *et al.* (2008); MORB, mid-ocean-ridge basalts; OIB, oceanic island basalt.

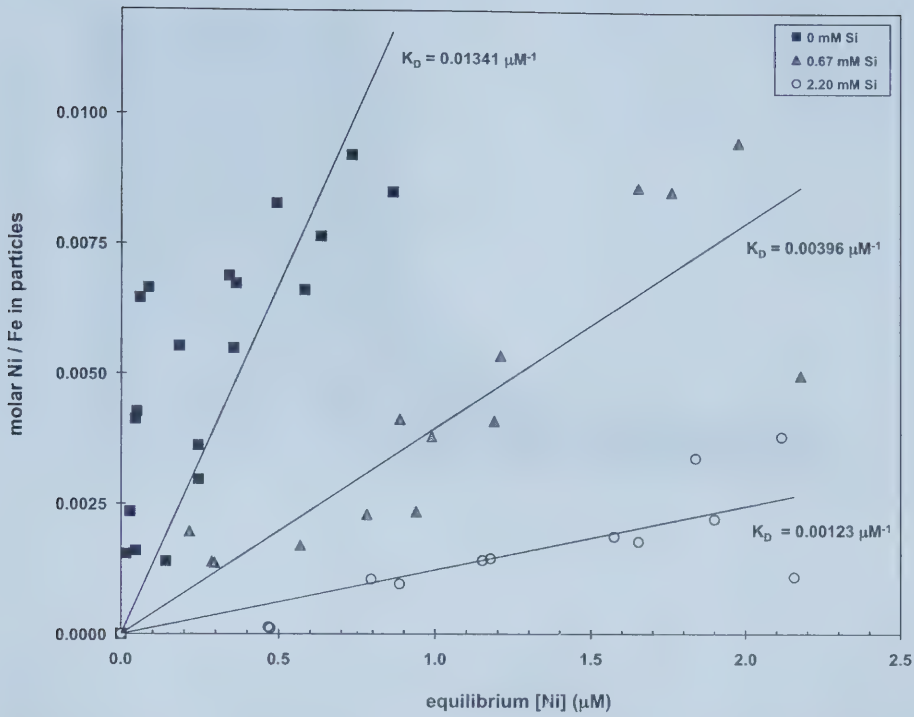

Figure 2. Experimentally determined distribution coefficients for dissolved Ni. The K_d values were obtained during Ni co-precipitation with HFO, and in the presence of various concentrations of silica, as per Konhauser et al (2007).

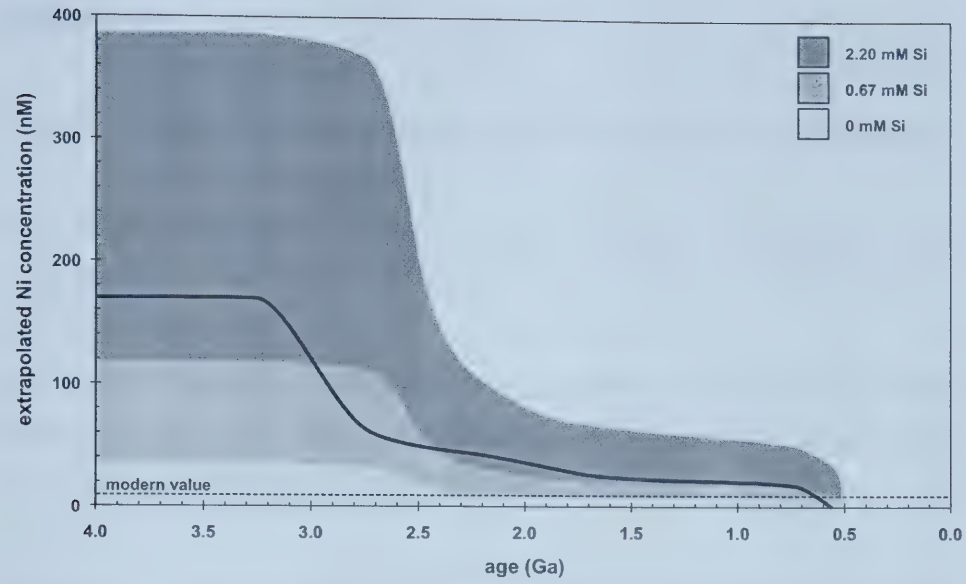

Figure 3. Maximum dissolved Ni concentrations in sea water through time. Values were extrapolated from solid-phase BIF Ni/Fe data using experimentally determined Ni distribution coefficients. The three shaded areas represent maximum aqueous Ni concentrations at dissolved silica concentrations of 2.20 mM (dark grey), 0.67 mM (medium grey) and 0 mM (light grey). The solid black line represents the average dissolved Ni value from time-averaged Ni/Fe ratios as calculated in Figure S3. The modern mean oceanic Ni concentration (9 nM; Drever, 1988) is plotted as a broken line.

References

Arndt, N. T. High Ni in Archean tholeiites. *Tectonophysics* **187,** 411–420 (1991).

Arndt, N. T., Barnes, S. J. & Lesher, C. M. *Komatiite* (Cambridge University Press, 2008).

Barley, M. E., Bekker, A. & Krapez, B. Late Archean to early Paleoproterozoic global tectonics, environmental change and the rise of atmospheric oxygen. *Earth Planet. Sci. Lett.* **238,** 156–171 (2005).

Barley, M. E., Krapez, B., Groves, D. I. & Kerrich, R. The Late Archaean bonanza: metallogenic and environmental consequences of the interaction between mantle plumes, lithospheric tectonics and global cyclicity. *Precambr. Res.* **91,** 65–90 (1998).

Basiliko, N. & Yavitt, J. B. Influence of Ni, Co, Fe, and Na additions on methane production in *Sphagnum*-dominated Northern American peatland. *Biogeochemistry* **52,** 133–153 (2001).

Berry, A. J., Danyushevsky, L. V., O'Neill, H. C., Newville, M. & Sutton, S. R. Oxidation state of iron in komatiite melt inclusions indicates hot Archaean mantle. *Nature* **455,** 960–963 (2008).

Bjerrum, C. J. & Canfield, D. E. Ocean productivity before about 1.9 Gyr limited by phosphorus adsorption onto iron oxides. *Nature* **417,** 159–162 (2002).

Catling, D. C., Claire, M. W. & Zahnle, K. J. Anaerobic methanotrophy and the rise of atmospheric oxygen. *Phil. Trans. R. Soc. A* **365,** 1867–1888 (2007).

Chester, R. *Marine Geochemistry* (Blackwell, 2000).

Condie, K. C. Chemical composition and evolution of the upper continental crust: contrasting results from surface samples and shales. *J. Chem. Geol.* **104,** 1–37 (1993).

da Silva, J. J. R. F. & Williams, R. J. P. *The Biological Chemistry of the Elements: The Inorganic Chemistry of Life* (Oxford University Press, 1991).

Diekert, G., Weber, B. & Thauer, R. K. Nickel dependence of factor F430 content in *Methanobacterium thermoautotrophicum*. *Arch. Microbiol.* **127,** 273–278 (1980).

Drever, J. I. *The Geochemistry of Natural Waters* 2nd edn (Prentice Hall, 1988).

Hannington, M. D., Santaguida, F., Kjarsgaard, I. M. & Cathles, L. M. Regional-scale hydrothermal alteration in the Central Blake River Group, western Abitibi subprovince, Canada: implications for VMS prospectivity. *Mineralium Deposita* **38,** 393– 422 (2003).

Hausrath, E. M., Liermann, L. J., House, C. H., Ferry, J. G. & Brantley, S. L. The effect of methanogen growth on mineral substrates: will Ni markers of methanogen-based communities be detectable in the rock record? *Geobiology* **5,** 49–61 (2007).

Jarrell, K. F., Colvin, J. R. & Sprott, G. D. Spontaneous protoplast formation in *Methanobacterium bryantii*. *J. Bacteriol.* **149,** 346–353 (1982).

Jaun, B. & Thauer, R. K. in *Metal Ions in Life Sciences* Vol. 2, *Nickel and its Surprising Impact in Nature* (eds Sigel, A., Sigel, H. & Sigel, R. K. O.) 323–356 (Wiley & Sons, 2007).

Kamber, B. S. & Webb, G. E. The geochemistry of late Archaean microbial

carbonate: implications for ocean chemistry and continental erosion history. *Geochim. Cosmochim. Acta* **65,** 2509–2525 (2001).

Kamber, B. S., Whitehouse, M. J., Bolhar, R. & Moorbath, S. Volcanic resurfacing and the early terrestrial crust: zircon U-Pb and REE constraints from the Isua Greenstone Belt, southern West Greenland. *Earth Planet. Sci. Lett.* **240,** 276–290 (2005).

Keays, R. R. The role of komatiitic and picritic magmatism and S-saturation in the formation of ore deposits. *Lithos* **34,** 1–18 (1995).

Kharecha, P., Kasting, J. & Siefert, J. A coupled atmosphere-ecosystem model of the early Archean Earth. *Geobiology* **3,** 53–76 (2005).

Kida, K. *et al.* Influence of Ni2+ and Co2+ on methanogenic activity and the amounts of coenzymes involved in methanogenesis. *J. Biosci. Bioeng.* **91,** 590–595 (2001).

Konhauser, K. O., Lalonde, S. V., Amskold, L. & Holland, H. D. Was there really an Archean phosphate crisis? *Science* **315,** 1234 (2007).

Krüger, M. *et al.* A conspicuous nickel protein in microbial mats that oxidize methane anaerobically. *Nature* **426,** 878–881 (2003).

Kump, L. R. & Barley, M. E. Increased subaerial volcanism and the rise of atmospheric oxygen 2.5 billion years ago. *Nature* **448,** 1033–1036 (2007).

Maliva, R. G., Knoll, A. H. & Simonson, B. M. Secular change in the Precambrian silica cycle: insights from chert petrology. *Geol. Soc. Am. Bull.* **117,** 835–845 (2005).

McLennan, S. M. in *Geochemistry and Mineralogy of Rare Earth Elements* (eds Lipin, B. R. & McKay, G. A.) 169-200 (Mineral Society of America, 1989).

McLennan, S. M., Taylor, S. R. & Eriksson, K. A. Geochemistry of Archean shales from Pilbara Supergroup, Western Australia. *Geochim. Cosmochim. Acta* **47,** 1211–1222 (1983).

Nisbet, E. G. in *Komatiites* (eds Arndt, N.T. & Nisbet, E.G.) 501–520 (George Allen and Unwin, 1982).

Öztürk, M. Trends of trace metal (Mn, Fe, Co, Ni, Cu, Zn, Cd and Pb) distributions at the oxic-anoxic interface and in sulfidic water of the Drammensfjord. *Mar. Chem.* **48,** 329– 342 (1995).

Papineau, D., Mojzsis, S. J. & Schmitt, A. K. Multiple sulfur isotopes from Paleoproterozoic Huronian interglacial sediments and the rise of atmospheric oxygen. *Earth Planet. Sci. Lett.* **255,** 188–212 (2007).

Saito, M. A., Moffett, J. W. & DiTullio, G. R. Cobalt and nickel in the Peru upwelling region: a major flux of labile cobalt utilized as a micronutrient. *Glob. Biogeochem. Cycles* **18,** GB4030 (2004).

Saito, M. A., Sigman, D. M. & Morel, F. M. M. The bioinorganic chemistry of the ancient ocean: the co-evolution of cyanobacterial metal requirements and biogeochemical cycles at the Archean-Proterozoic boundary? *Inorg. Chim. Acta* **356,** 308–318 (2003).

Schönheit, P., Moll, J. & Thauer, R. K. Nickel, cobalt, and molybdenum requirement for growth of *Methanobacterium thermoautotrophicum*. *Arch. Microbiol.* **123,** 105–107 (1979).

Scott, C. *et al.* Tracing the stepwise oxygenation of the Proterozoic ocean. *Nature* **452,** 456–459 (2008).

Shima, S. & Thauer, R. K. A third type of hydrogenase catalysing H2 activation. *Chem. Rec.* **7,** 37–46 (2007).

Taylor, S. R. & McLennan, S. M. *The Continental Crust: Its Composition and Evolution* (Blackwell, 1985).

Tréguer, P. *et al.* The silica balance in the world ocean: a reestimate. *Science* **268,** 375–379 (1995).

Trendall, A. F. in *Precambrian Sedimentary Environments: A Modern Approach to Ancient Depositional Systems* (eds Altermann, W. & Corcoran, P. L.) 33–66 (Special Publication 33, International Association of Sedimentologists, 2002).

Zahnle, K. J., Claire, M. W. & Catling, D. C. The loss of mass-independent fractionation of sulfur due to a Paleoproterozoic collapse of atmospheric methane. *Geobiology* **4,** 271– 283 (2006).

Supplemental Material

for

Oceanic Nickel Depletion and a Methanogen Famine Before the Great Oxidation Event

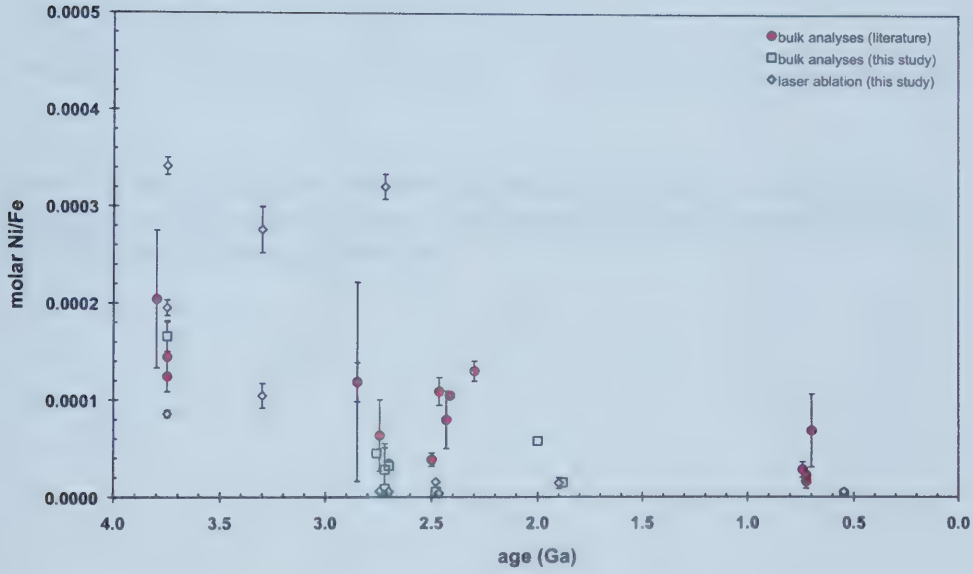

Figure S1. Comparison of new bulk and laser ablation Ni/Fe data (this study) with previously published literature bulk analyses. Error bars are 2 standard errors of the mean.

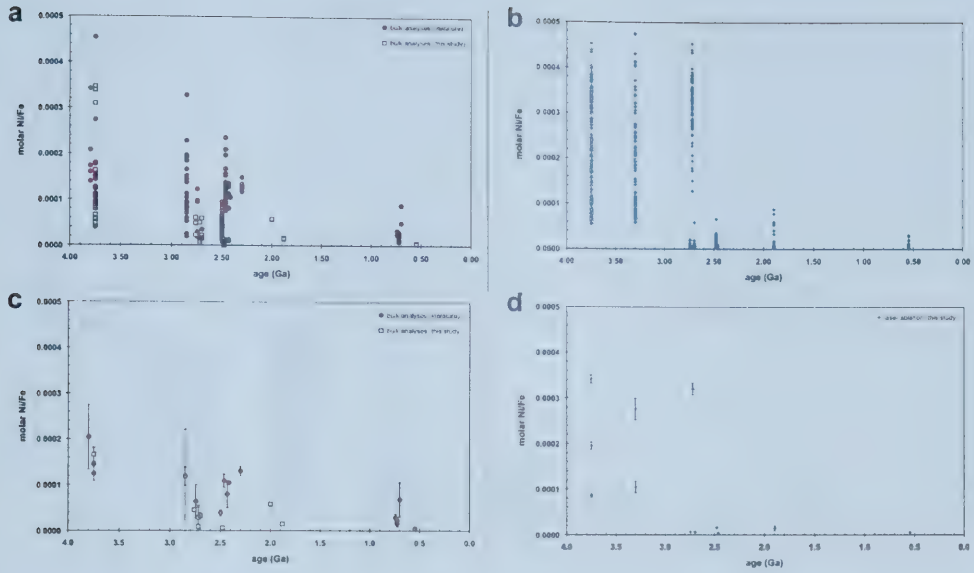

Figure S2. Individual molar Ni/Fe bulk (a) and laser-ablation analyses (b) with their corresponding average values for any given BIF (c and d, respectively). Error bars are 2 standard errors of the mean.

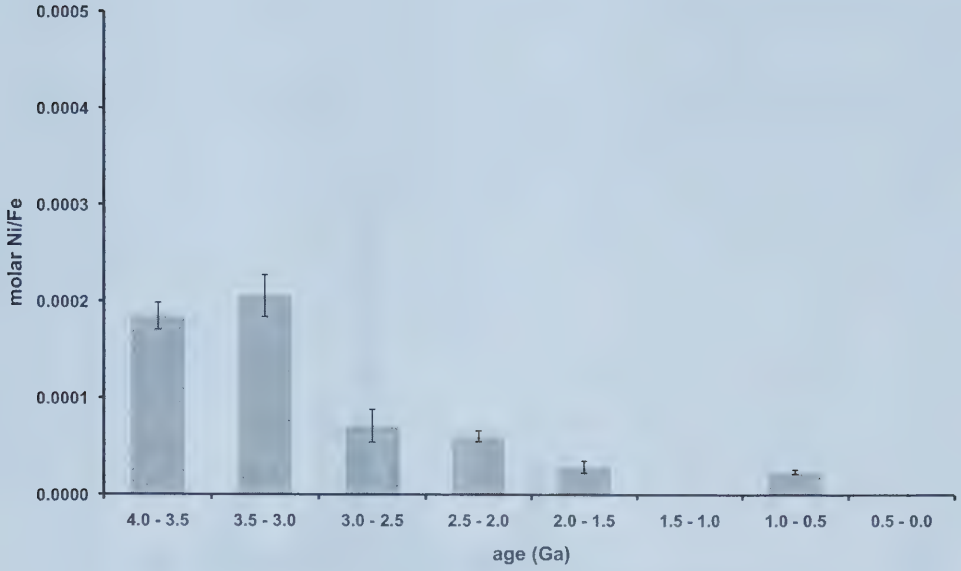

Figure S3. Summary of average molar Ni/Fe values as function of time interval. Both laser ablation and bulk values are included in the average. Error bars are 2 standard errors of the mean.

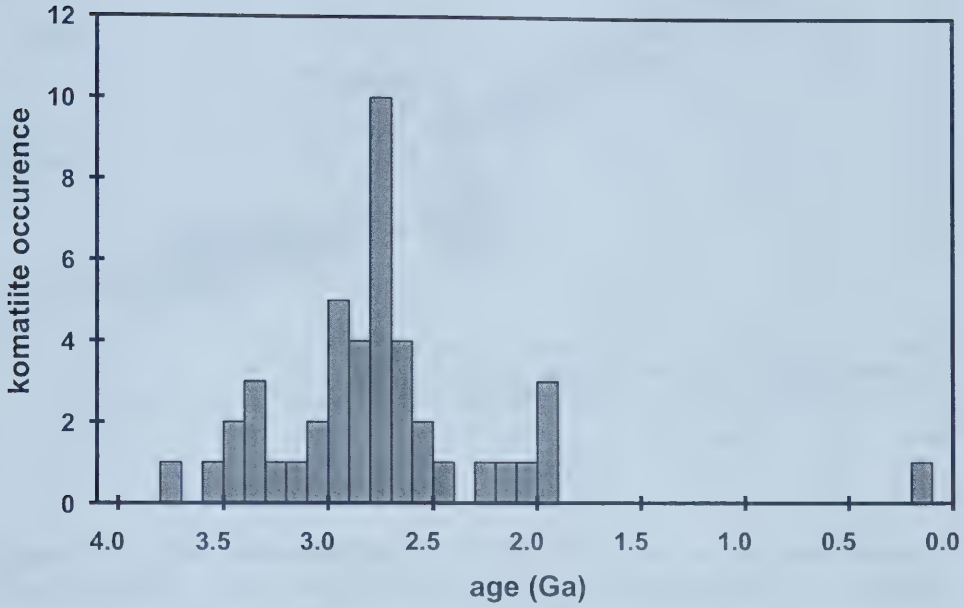

Figure S4. Distribution of preserved komatiite-bearing volcanic successions through time (data provided in Table S3).

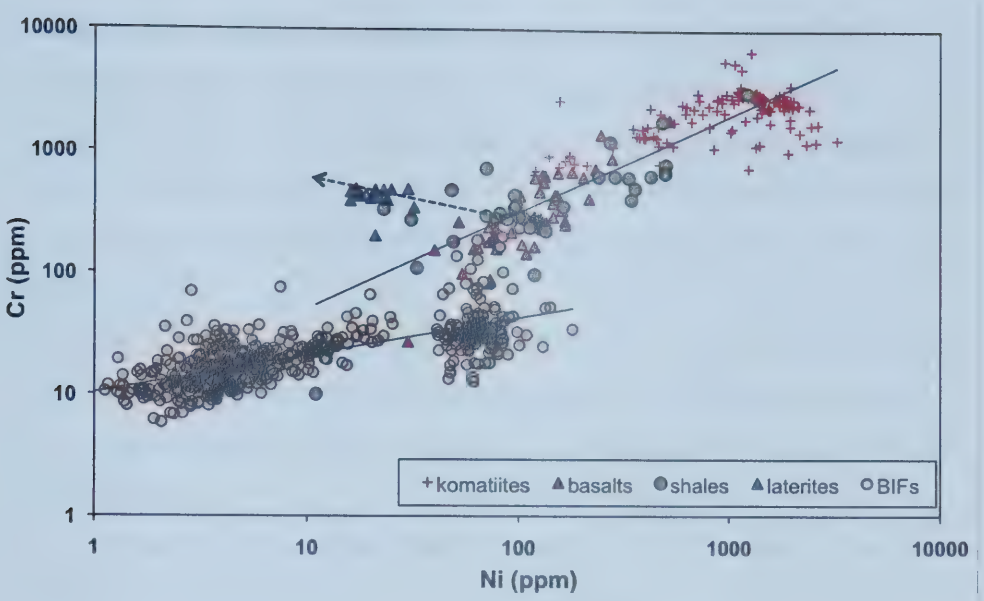

Figure S5. Log-log concentration plot of Cr vs. Ni for various Archean lithologies. Note the shallower trend line for BIF compared to (meta)volcanic rocks and shales indicating that Ni was preferentially transported to seawater (with respect to Cr). The different slopes also argue against high Ni concentrations in BIF being caused by incorporation of clastic detritus or volcanic ash. The two BIF populations are differentiated by age, with the right hand population limited to samples older than 3.3 Ga (stage one samples only). Also added is an arrow highlighting the weathering trend, from parental basalts to overlying laterites, showing an accumulation of Cr in the latter. BIF data represents new analyses or was compiled as referenced in Table S1. Literature values were employed for komatiites and basalts[1-7], shales[8-9] and laterites[2].

1. Nesbitt, R.W, Sun, S-S. & Purvist, A.C. Komatiites: Geochemistry and genesis. *Can. Mineral.* **17**, 165-186 (1979).
2. Macfarlane, W., Danielson, A. & Holland, H.D. Geology and major and trace element chemistry of late Archean weathering profiles in the Fortescue Group, Western Australia: Implications for atmospheric pO_2. *Prec. Res.* **65**, 291-317 (1994).
3. Stern, R.A., Syme, E.C. & Lucas, S.B. Geochemistry of 1.9 Ga MORB- and OIB-like basalts from the Amisk collage, Flin Flon Belt, Canada: Evidence for an intra-oceanic origin. *Geochim. Cosmochim. Acta* **59**, 3131-3154 (1995).

4. Puchtel, I.S., Haase, K.M., Hofmann, A.W., Chauvel, C., Kulikov, V.S., Garbe-Schönberg, C.D. & Nemchin, A.A. Petrology and geochemistry of crustally contaminated komatiitic basalts from the Vetreny Belt, southeastern Baltic Shield: Evidence for an Early Proterozoic mantle plume beneath rifted Archean continental lithosphere. *Geochim. Cosmochim. Acta* **61**, 1205– 1222 (1997).
5. Parman, S.W., Shimizu, N., Grove, T.L. & Dann, J.C. Constraints on the pre-metamorphic trace element composition of Barberton komatiites from ion probe analyses of preserved clinopyroxene. *Contrib. Mineral. Petrol.* **144**, 383–396 (2003).
6. Chavagnac, V.A. Geochemical and Nd isotopic study of Barberton komatiites (South Africa): Implication for the Archean mantle. *Lithos* **75**, 253–281 (2004).
7. Puchtel, I.S., Brandon, A.D. & Humayun, M. Precise Pt–Re–Os isotope systematics of the mantle from 2.7-Ga komatiites. *Earth Planet. Sci. Lett.* **224**, 157–174 (2004).
8. McLennan, S.M., Taylor, S.R. & Eriksson, K.A. Geochemistry of Archean shales from Pilbara Supergroup, Western Australia. *Geochim. Cosmochim. Acta* **47**, 1211-1222 (1983).
9. Fedo, C.M., Eriksson, K.A. & Krogstad, E. J. Geochemistry of shales from the Archean (~3.0 Ga) Buhwa Greenstone Belt, Zimbabwe: Implications for provenance and source-area weathering. *Geochim. Cosmochim. Acta* **60**, 1751-1763 (1996).

Table S1: Chemical composition of banded iron formations through time.

Age (Ga)	Unit	Sample	Bulk Values from Literature (n=306)			Sample	New Bulk Analysis* (n=38)		
			Fe (mol/kg)	Ni (mol/kg)	molar Ni/Fe		Fe (mol/kg)	Ni (mol/kg)	molar Ni/Fe
ca 3.8	Nuvvuagittuq (Canada) (1)	PC-192	5 518	9.54E-04	1.73E-04				
		PC-193	2 195	7.50E-04	3.42E-04				
		PC-197	6 399	1.33E-03	2 08E-04				
		PC-198B	8 219	1.14E-03	1.39E-04				
		PC-200	8 230	1.31E-03	1.59E-04				
ca. 3.75	Isua Greenstone Belt *(2, 3)*	629-3B	5.828	5.20E-04	8.92E-05				
	(Greenland)	29-2	4.675	8.28E-04	1.77E-04				
		623-7B	5 155	5 30E-04	1.03E-04				
		701-2C	4 650	1.84E-04	3.96E-05				
		623-7A	3.226	4.09E-04	1.27E-04				
		10-2B	2 818	4.19E-04	1 49E-04				
		623-6B	2 279	4.09E-04	1.79E-04				
		7_4	6 077	5.79E-04	9.53E-05				
		809-1J	4 851	7.34E-04	1.51E-04				
		716-13	4 422	4.96E-04	1.12E-04				
		711-4C	4 357	6.22E-04	1.43E-04				
		625-8C	4 631	5.69E-04	1.23E-04				
		625-10	4 038	4.38E-04	1.08E-04				
		10-2A	2.016	9.15E-04	4.54E-04				
		625-9B	0 430	1.33E-04	3.09E-04				
		155 781	2 508	2.27E-04	9.04E-05	155 781	2.499	1.45E-04	5.80E-05
		155 782	2 612	2.50E-04	9.59E-05	155 782	2.612	2.10E-04	8.02E-05
		155 783	4 532	3.82E-04	8.42E-05	155 783	4.532	2.96E-04	6.54E-05
		248 470	0 343	9.37E-05	2.73E-04	248 470	0.344	1.19E-04	3.46E-04
		SM-GR 96/23	3 080	3.36E-04	1.09E-04	249 470 dup	0.352	1.19E-04	3.39E-04
		SM-GR 97/26	4 474	2.44E-04	5.45E-05	SM-GR 96/23	3.030	2.56E-04	8.44E-05
		SM-GR 93/45	0.292	4.60E-05	1.58E-04	SM-GR 97/26	4.483	1.38E-03	3.09E-04
		SM-GR 93/45 dup	0 292	4.77E-05	1.64E-04	SM-GR 93/45	0.293	4.77E-05	1.63E-04
		SM-GR 93/47	3 232	2.56E-04	7.91E-05	SM-GR 93/47	3.217	1.53E-04	4.77E-05
	Ugpik (Greenland) *(3)*	SM-GR 97/20	4.855	5.79E-04	1.24E-04				
ca 2.85	Yilgarn Block (Australia) *(4)*	1	6 480	3.41E-04	5.26E-05				
		2	6 868	1.70E-04	2.48E-05				
		5	4 348	8.52E-05	1.96E-05				
		17	3 358	7.67E-04	2.28E-04				
		18	2 857	9.37E-04	3.28E-04				
		19	4 269	2.56E-04	5.99E-05				
	Mount Gibson (Australia) *(5)*	1410	5 446	9.03E-04	1.66E-04				
		530	6 200	6.47E-04	1.04E-04				
		503	5 955	9.03E-04	1.52E-04				
		1396	6 367	9.20E-04	1.45E-04				
		635	6 091	1.12E-03	1.85E-04				
		870	7 281	1.40E-03	1.92E-04				
		1240	7 566	1.04E-03	1.37E-04				
		978	8 126	1.60E-03	1.97E-04				
		632	7 297	5.79E-04	7.94E-05				
		657	7 896	7.50E-04	9.50E-05				
		659	8 286	6.99E-04	8.43E-05				
		868	9 876	7.84E-04	7.94E-05				
		865	10 617	9.71E-04	9.15E-05				
		532	9 944	7.84E-04	7.88E-05				
		867	10 435	1.18E-03	1.13E-04				
		1364	9.691	8.01E-04	8.26E-05				
		1360	7 961	6 65E-04	8.35E-05				
		1357	8 157	5.79E-04	7.10E-05				
ca 2.76	Temagami - Sherman Mine					070922-6	3.418	7.67E-05	2.24E-05
	(Canada)					070922-6b	4.859	2.95E-04	6.07E-05
						070922-7	5.757	2.79E-04	4.85E-05
						070922-7b	5.823	2 85E-04	4.89E-05
2.74-2.75	Carajas (Brazil) *(6)*	2	9 102	1.70E-04	1.87E-05				
		3	7 566	7.16E-04	9.46E-05				
		4	5 874	1.70E-04	2.90E-05				
		5	8 410	8.18E-04	9.72E-05				
		9	8 579	1.70E-04	1.99E-05				
		10	6 404	7.84E-04	1.22E-04				
ca 2.72	Temagami - Hwy 11					070922-1	3.507	3.75E-05	1.07E-05
	(Canada)					070922-1b	4.287	2.90E-05	6.76E-06
	Upper Deloro Assemblage					070923-1	3.625	1.81E-04	4.98E-05
	(Canada)					070923-1b	5.281	3.58E-05	6.78E-06
ca 2.7	Beardmore Area (Canada)					070925-4	2.137	3.24E-05	1.52E-05
						070925-4b	8 132	1.77E-04	2.18E-05
						070925-6	5.639	3.34E-04	5.92E-05
	Orissa (India) *(7)*	n=11	7.414	2.56E-04	3.45E-05				
ca 2.5	Quadrilátero Ferrífero	SP-2	6.265	3.41E-04	5.44E-05				
	(Minas Gerais, Brazil) *(8-9)*	SP-3	6.813	3.92E-04	5.75E-05				
		SP-4	7.719	3.07E-04	3.97E-05				
		SP-5	5 965	2.90E-04	4.86E-05				

Table cont.

ca 2.5	Quadrilatero Ferrifero (Minas Gerais, Brazil) *(8-9)*	Pico-1	5.722	3.58E-04	6.25E-05				
		Pico-5	6.360	3.41E-04	5.36E-05				
		AC-6	7.472	2.73E-04	3.65E-05				
		AC-8	4.323	2.73E-04	6.31E-05				
		M4	5 798	9.54E-05	1.65E-05				
		M5	5.042	5.96E-05	1.18E-05				
		M6	5.717	1.18E-04	2.06E-05				
		M7	5.818	4.77E-05	8.20E-06				
		M8	5.375	8.01E-05	1.49E-05				
		M9	6 637	1.70E-04	2 57E-05				
		M10	6.877	1.74E-04	2 53E-05				
		M11	8.529	1.70E-04	2.00E-05				
		M98	7.517	5.62E-04	7.48E-05				
		P55_27	5.637	2.23E-04	3.96E-05				
		P55_61	5.426	1.81E-04	3.33E-05				
		P3_18	4.680	1.50E-04	3.20E-05				
		P3_23	6.182	1.60E-04	2.59E-05				
		P3_36	6.827	1.28E-04	1.87E-05				
		P3_50	8.598	3.41E-04	3.96E-05				
		P54_80	9.931	8.01E-05	8.06E-06				
		P54_85	7.593	1.35E-04	1.77E-05				
		P54_120	5.117	2.13E-04	4.16E-05				
		P54_124	6.312	1.55E-04	2 46E-05				
		P3_69	8.605	2.52E-04	2 93E-05				
		P3_83	4.145	2.79E-04	6.74E-05				
		P3_103	4.684	2.16E-04	4.62E-05				
		P3_122	4 049	5.79E-05	1.43E-05				
		P3_138	2.873	2.37E-04	8.24E-05				
		M5A	10.487	1.91E-04	1.82E-05				
		M6A	10.660	2.85E-04	2.67E-05				
		M7A	10.346	2.47E-04	2.39E-05				
		M8A	8.779	2.28E-04	2.60E-05				
		M10A	8 212	4.29E-04	5.23E-05				
		M11A	10 298	1.67E-04	1.62E-05				
		M1	2 012	1.09E-04	5 42E-05				
		M16	3.130	1.86E-04	5.93E-05				
		AC-5	7.008	6.65E-04	9.48E-05				
		AC-7	4 953	4.43E-04	8.94E-05				
ca 2.48	Dales Gorge (Australia)					DG	3 249	2 90E-05	8.91E-06
						DG 36.16A	5.097	1.19E-05	2.34E-06
						DG 36 16B	5.227	1 36E-05	2.61E-06
						DG 96.11-12A	3 426	2.22E-05	6.46E-06
						DG 96.11-12B	45.924	2.90E-05	6 31E-07
						DG 96.11-12B^{duo}	4 640	2.90E-05	6.24E-06
						DG 36.075	5 419	3.75E-05	6.92E-06
						L/G 36.085	2 176	2.73E-05	1.25E-05
						DG 96.7	5 438	2.39E-05	4.39E-06
						DG 96.10.11	3 497	1.70E-05	4.87E-06
ca 2.465	Kuruman *(10-11)* (South Africa)	AD5-92.5	4 635	4.94E-04	1 07E-04				
		AD5-94.40	6.769	5.11E-04	7.55E-05				
		AD5-124.8	6 008	4.94E-04	8.22E-05				
		AD5-136.5	5.816	5.11E-04	8.79E-05				
		AD5-149.8	4 854	4.94E-04	1.02E-04				
		AD5-152.1	4.615	4.94E-04	1.07E-04				
		WB98-791.2	5.995	5.11E-04	8.53E-05				
		WB98-791.40	5.591	5.11E-04	9.14E-05				
		AD5-121.30	3.822	4.60E-04	1.20E-04				
		AD5-158.40	3 774	4.94E-04	1.31E-04				
		AD5-159.3	3.080	4.77E-04	1.55E-04				
		AD5-161.90	4 787	5.11E-04	1.07E-04				
		AD5-161.95	3.462	5.28E-04	1.53E-04				
		AD5-167.8	3.474	4.77E-04	1.37E-04				
		AD5-168.7	3.784	5.11E-04	1.35E-04				
		DI1-213 8	3.162	4.94E-04	1.56E-04				
		DI1-237	5.425	5.45E-04	1.01E-04				
		WB98-814 3	3.738	4.77E-04	1.28E-04				
		WB98-816.9	2 959	4.94E-04	1.67E-04				
		WB98-866	3.671	4.60E-04	1.25E-04				
		156.85	6 372	5.62E-04	8.82E-05				
		160.97	4.058	5.11E-04	1.26E-04				
		162.34	4 960	4.60E-04	9 27E-05				
		166.1	3.635	4.94E-04	1 36E-04				
		168.78	5.193	4.94E-04	9.52E-05				
		169.24	4.164	5 45E-04	1,31E-04				
		170 25	6.174	5.45E-04	8.83E-05				
		172 75	5.254	4.77E-04	9.08E-05				
		173.16	4.929	4.77E-04	9.68E-05				

Table cont

ca 2.465	Kuruman *(10-11)*	173.2	4.920	5.79E-04	1.18E-04				
	(South Africa)	175 94	5.129	5.28E-04	1.03E-04				
		178 99	4.711	5.28E-04	1.12E-04				
		187.2	6.048	4.94E-04	8.17E-05				
		189.6	4.967	4.77E-04	9.60E-05				
		193.87	4 630	3.92E-04	8.46E-05				
		n=12	6.383	6.82E-05	1.07E-05				
		n=21	6 038	6.82E-05	1 13E-05				
		n=26	5.224	5.11E-05	9 79E-06				
		n=10	6.215	6.82E-05	1.10E-05				
		AD5-163.2	2.391	5 62E-04	2.35E-04				
		DI1-223 8	2.677	5 28E-04	1.97E-04				
		WB96-882	2.196	4.60E-04	2.09E-04				
ca 2.432	Griqualown *(11-13)*	140 8	6.738	5.45E-04	8 09E-05				
	(South Africa)	142 83	4 692	4.94E-04	1 05E-04				
		150.25	4.801	5.28E-04	1 10E-04				
		152.03	3.905	5.28E-04	1 35E-04				
		153.23	4.552	4.94E-04	1.09E-04				
		154 1	4.394	4.94E-04	1.12E-04				
		155 7	4.439	5.79E-04	1 31E-04				
		n=6	5.528	6 82E-05	1.23E-05				
		n=14	6.037	6 82E-05	1.13E-05				
		n=16	5.549	6 82E-05	1.23E-05				
		n=3	6 909	6 82E-05	9 87E-06				
		n=5	4.652	5 96E-04	1.28E-04				
ca 2.415	Reeinekke (South Africa) *(13)*	RBIFs (n=15)	3.578	3.75E-04	1.05E-04				
ca 2.3	Hotazel (South Africa) *(14)*	7	5 735	7.67E-04	1 34E-04				
		8	5 759	7.33E-04	1 27E-04				
		9	6 387	7.50E-04	1.17E-04				
		10	5 228	6.47E-04	1.24E-04				
		11	6.196	9.20E-04	1.49E-04				
ca 2.0	Loch Maree Group (Scotland)					LMG	4.128	4.60E-04	1.11E-04
ca 1.88	Gunflint (Canada)					Gunflint-1	7.616	1.09E-04	1.43E-05
						Gunflint-2	3.665	5.96E-05	1.63E-05
						Gunflint-2b	1.643	2.39E-05	1.45E-05
						Gunflint-2c	1 651	2 39E-05	1.44E-05
0.73-.755	Rapitan (Canada) *(15)*	Y-7/142	6.362	1.53E-04	2.41E-05				
		Y-7/152.8	4.210	1.36E-04	3.24E-05				
0.7-0.75	Urucum (Brazil) *(16)*	Ur1 A	8 644	1.70E-04	1.97E-05				
		U-2-7	9 175	1.70E-04	1 86E-05				
		U-2-8	7.574	1.70E-04	2.25E-05				
		U-2-9	6 070	1.70E-04	2 81E-05				
	Braemar (Australia) (17)	BR8	8.361	8 52E-05	1.02E-05				
		BR13	7.807	1 02E-04	1.31E-05				
		BR40	9 882	8 52E-05	8.62E-06				
		BR52	6.231	1 19E-04	1 91E-05				
		BR53	8.290	2.39E-04	2.88E-05				
0.75-0.65	Chuos (Namibia) *(18)*	CD1	4.487	2.22E-04	4 94E-05				
		CD3	3.291	2.90E-04	8.80E-05				
0.545-0.55	Yerbal (Uruguay)					Y-1	3.927	1.53E-05	3.91E-06
						Y-2	5 059	2.56E-05	5.05E-06
						Y-3	4.637	2 22E-05	4 78E-06

Age (Ga)	Unit	Sample	Laser ablation analyses (n=870)			Sample	Laser ablation analyses cont.		
			Fe (mol/kg)	Ni (mol/kg)	molar Ni/Fe		Fe (mol/kg)	Ni (mol/kg)	molar Ni/Fe
ca 3.75	Isua Greenstone Belt	E-1	12.755	1.86E-03	1.46E-04	E-1	12.691	2.58E-03	2.03E-04
		E-1	12.749	2.13E-03	1.67E-04	E-1	12.691	2.84E-03	2.23E-04
		E-1	12.662	1.90E-03	1.50E-04	E-1	12.691	2.82E-03	2.23E-04
		E-1	12.662	1.98E-03	1.56E-04	E-1	12.691	3.11E-03	2.45E-04
		E-1	12.809	2.35E-03	1.83E-04	E-1	12.691	2.89E-03	2.28E-04
		E-1	12.809	2.49E-03	1.95E-04	E-1	12.691	2.13E-03	1.68E-04
		E-1	12.809	2.76E-03	2.16E-04	E-1	12.691	2.12E-03	1.67E-04
		E-1	12.809	2.90E-03	2.26E-04	E-1	12.691	2.01E-03	1.59E-04
		E-1	12.809	2.92E-03	2.28E-04	E-1	12.691	2.17E-03	1.71E-04
		E-1	12.809	2.50E-03	1.95E-04	E-1	12.691	2.32E-03	1.83E-04
		E-1	12.809	3.03E-03	2.37E-04	E-1	12.691	2.47E-03	1.95E-04
		E-1	12.809	1.87E-03	1.46E-04	E-1	12.808	2.64E-03	2.06E-04
		E-1	12.758	2.26E-03	1.77E-04	E-1	12.808	2.76E-03	2.16E-04
		E-1	12.809	2.30E-03	1.79E-04	E-1	12.808	2.80E-03	2.19E-04
		E-1	12.766	2.00E-03	1.56E-04	E-1	12.808	3.09E-03	2.42E-04
		E-1	12.766	2.35E-03	1.84E-04	E-1	12.808	2.97E-03	2.32E-04
		E-1	12.766	2.58E-03	2.02E-04	E-1	12.808	1.87E-03	1.46E-04
		E-1	12.766	2.65E-03	2.07E-04	E-1	12.808	2.02E-03	1.58E-04
		E-1	12.766	2.88E-03	2.25E-04	E-1	12.808	2.04E-03	1.59E-04
		E-1	12.766	2.87E-03	2.25E-04	E-1	12.808	2.19E-03	1.71E-04
		E-1	12.766	2.83E-03	2.22E-04	E-1	12.808	2.47E-03	1.93E-04
		E-1	12.766	3.01E-03	2.36E-04	E-1	12.808	2.61E-03	2.04E-04
		E-1	12.766	1.86E-03	1.46E-04	E-1	12.808	2.77E-03	2.17E-04
		E-1	12.766	1.77E-03	1.39E-04	E-1	12.775	2.88E-03	2.25E-04
		E-1	12.766	2.17E-03	1.70E-04	E-1	12.775	2.79E-03	2.19E-04
		E-1	12.766	2.23E-03	1.74E-04	E-1	12.775	3.09E-03	2.42E-04
		E-1	12.766	2.40E-03	1.88E-04	E-1	12.775	3.05E-03	2.39E-04
		E-1	12.691	2.59E-03	2.04E-04				
ca 3.75	Isua Greenstone Belt	97-23	12.814	1.50E-03	1.17E-04	97-23	12.814	8.10E-04	6.32E-05
		97-23	12.814	1.42E-03	1.11E-04	97-23	12.814	9.83E-04	7.67E-05
		97-23	12.814	1.08E-03	8.44E-05	97-23	12.814	1.14E-03	8.90E-05
		97-23	12.814	1.38E-03	1.08E-04	97-23	12.814	9.91E-04	7.74E-05
		97-23	12.814	8.66E-04	6.76E-05	97-23	12.814	9.03E-04	7.05E-05
		97-23	12.814	1.09E-03	8.49E-05	97-23	12.814	1.09E-03	8.54E-05
		97-23	12.814	1.01E-03	7.87E-05	97-23	12.823	1.59E-03	1.24E-04
		97-23	12.814	1.43E-03	1.12E-04	97-23	12.823	1.46E-03	1.14E-04
		97-23	12.814	1.08E-03	8.46E-05	97-23	12.823	1.31E-03	1.02E-04
		97-23	12.814	1.15E-03	9.01E-05	97-23	12.823	1.37E-03	1.07E-04
		97-23	12.814	1.04E-03	8.15E-05	97-23	12.823	1.67E-03	1.30E-04
		97-23	12.814	1.59E-03	1.24E-04	97-23	12.823	1.32E-03	1.03E-04
		97-23	12.814	1.12E-03	8.76E-05	97-23	12.823	1.10E-03	8.56E-05
		97-23	12.814	1.07E-03	8.37E-05	97-23	12.823	1.33E-03	1.04E-04
		97-23	12.814	9.65E-04	7.53E-05	97-23	12.823	1.43E-03	1.12E-04
		97-23	12.814	1.31E-03	1.02E-04	97-23	12.823	1.00E-03	7.80E-05
		97-23	12.814	1.15E-03	8.98E-05	97-23	12.659	8.70E-04	6.87E-05
		97-23	12.814	8.18E-04	6.38E-05	97-23	12.659	9.59E-04	7.57E-05
		97-23	12.814	1.12E-03	8.75E-05	97-23	12.659	1.29E-03	1.02E-04
		97-23	12.814	1.14E-03	8.93E-05	97-23	12.659	1.07E-03	8.47E-05
		97-23	12.814	7.14E-04	5.57E-05	97-23	12.659	7.64E-04	6.04E-05
		97-23	12.814	8.81E-04	6.88E-05	97-23	12.659	1.06E-03	8.40E-05
		97-23	12.814	1.03E-03	8.00E-05	97-23	12.659	1.00E-03	7.91E-05
		97-23	12.814	1.31E-03	1.02E-04	97-23	12.659	9.71E-04	7.67E-05
		97-23	12.814	1.05E-03	8.17E-05	97-23	12.659	1.26E-03	9.95E-05
		97-23	12.814	1.35E-03	1.05E-04	97-23	12.659	7.01E-04	5.54E-05
		97-23	12.814	8.00E-04	6.24E-05	97-23	12.830	1.01E-03	7.89E-05
		97-23	12.814	1.04E-03	8.15E-05	97-23	12.830	9.98E-04	7.78E-05
		97-23	12.814	1.43E-03	1.12E-04	97-23	12.830	8.52E-04	6.64E-05
		97-23	12.814	9.73E-04	7.60E-05	97-23	12.830	1.09E-03	8.52E-05
		97-23	12.814	8.15E-04	6.36E-05	97-23	12.830	1.06E-03	8.24E-05
		97-23	12.814	1.40E-03	1.09E-04	97-23	12.830	9.57E-04	7.46E-05
		97-23	12.814	1.06E-03	8.27E-05	97-23	12.830	1.43E-03	1.12E-04
		97-23	12.814	1.08E-03	8.44E-05	97-23	12.830	1.04E-03	8.10E-05
		97-23	12.814	1.27E-03	9.87E-05	97-23	12.830	1.14E-03	8.86E-05
		97-23	12.814	1.11E-03	8.67E-05	97-23	12.830	8.36E-04	6.51E-05
		97-23	12.814	1.01E-03	7.89E-05	97-23	12.830	1.03E-03	8.02E-05
		97-23	12.814	7.09E-04	5.53E-05	97-23	12.830	1.00E-03	7.83E-05
		97-23	12.814	7.74E-04	6.04E-05	97-23	12.830	1.09E-03	8.48E-05
		97-23	12.814	1.08E-03	8.43E-05	97-23	12.830	1.23E-03	9.58E-05
		97-23	12.814	8.66E-04	6.76E-05	97-23	12.830	8.97E-04	6.99E-05
		97-23	12.814	9.81E-04	7.66E-05	97-23	12.830	1.02E-03	7.92E-05
ca 3.75	Isua Greenstone Belt	97-26	12.790	3.54E-03	2.77E-04	97-26	12.735	4.23E-03	3.32E-04
		97-26	12.749	4.09E-03	3.21E-04	97-26	12.735	4.78E-03	3.76E-04
		97-26	12.749	4.16E-03	3.26E-04	97-26	12.735	4.43E-03	3.47E-04
		97-26	12.774	3.39E-03	2.65E-04	97-26	12.721	3.63E-03	2.86E-04
		97-26	12.749	4.41E-03	3.46E-04	97-26	12.721	4.26E-03	3.35E-04

Table cont

ca 3.75	Isua Greenstone Belt	97-26	12 749	3.98E-03	3.12E-04	97-26	12 735	4.89E-03	3.84E-04
		97-26	12 749	4.10E-03	3.22E-04	97-26	12 721	3.57E-03	2.80E-04
		97-26	12.749	4.73E-03	3.71E-04	97-26	12 735	3.93E-03	3.09E-04
		97-26	12.749	4.34E-03	3.40E-04	97-26	12 735	4.18E-03	3.28E-04
		97-26	12.749	3.59E-03	2.82E-04	97-26	12 721	4.72E-03	3.71E-04
		97-26	12 749	4.69E-03	3.68E-04	97-26	12 735	4.44E-03	3.48E-04
		97-26	12.749	3.95E-03	3.10E-04	97-26	12 721	4.40E-03	3.46E-04
		97-26	12 749	3.63E-03	2.85E-04	97-26	12 735	4.97E-03	3.90E-04
		97-26	12.665	4.47E-03	3.53E-04	97-26	12 721	4.20E-03	3.30E-04
		97-26	12.665	4.45E-03	3.51E-04	97-26	12 735	4.39E-03	3.45E-04
		97-26	12 760	4.74E-03	3.71E-04	97-26	12 735	4.86E-03	3.81E-04
		97-26	12 749	3.47E-03	2.72E-04	97-26	12 721	5.59E-03	4.40E-04
		97-26	12.707	3.46E-03	2.72E-04	97-26	12 749	4.77E-03	3.74E-04
		97-26	12 707	4.23E-03	3.33E-04	97-26	12 749	4.54E-03	3.56E-04
		97-26	12 707	4.17E-03	3.29E-04	97-26	12 735	5.53E-03	4.34E-04
		97-26	12.707	4.49E-03	3.54E-04	97-26	12 721	4.28E-03	3.37E-04
		97-26	12 707	3.65E-03	2.87E-04	97-26	12 749	3.20E-03	2.51E-04
		97-26	12 707	4.15E-03	3.27E-04	97-26	12 749	4.23E-03	3.32E-04
		97-26	12 707	4.47E-03	3.51E-04	97-26	12 735	4.70E-03	3.69E-04
		97-26	12 707	3.57E-03	2.81E-04	97-26	12 735	4.56E-03	3.58E-04
		97-26	12 707	3.99E-03	3.14E-04	97-26	12 721	4.69E-03	3.69E-04
		97-26	12 707	5.07E-03	3.99E-04	97-26	12 735	4.90E-03	3.85E-04
		97-26	12 707	4.20E-03	3.30E-04	97-26	12 735	4.70E-03	3.69E-04
		97-26	12 707	3.79E-03	2.98E-04	97-26	12 721	4.09E-03	3.22E-04
		97-26	12.707	4.11E-03	3.23E-04	97-26	12 735	4.45E-03	3.50E-04
		97-26	12 707	5.76E-03	4.53E-04	97-26	12 721	4.69E-03	3.69E-04
		97-26	12.707	3.90E-03	3.07E-04	97-26	12 735	5.14E-03	4.03E-04
		97-26	12.707	4.12E-03	3.24E-04	97-26	12 721	3.59E-03	2.82E-04
		97-26	12 707	4.69E-03	3.69E-04	97-26	12 735	4.44E-03	3.49E-04
		97-26	12.721	4.73E-03	3.72E-04	97-26	12 735	4.36E-03	3.42E-04
		97-26	12 721	4.34E-03	3.41E-04	97-26	12 721	4.88E-03	3.84E-04
		97-26	12 721	4.80E-03	3.78E-04	97-26	12 735	4.51E-03	3.54E-04
		97-26	12.721	3.84E-03	3.02E-04	97-26	12 721	4.72E-03	3.71E-04
		97-26	12 721	4.86E-03	3.82E-04	97-26	12 735	4.76E-03	3.74E-04
		97-26	12 735	4.04E-03	3.17E-04				
ca 3.3	Fig Tree (South Africa)	BG0316	11.361	9.59E-04	8.44E-05	BG0316	12 248	1.15E-03	9.43E-05
		BG0316	10 203	2.27E-03	2.22E-04	BG0316	12 248	9.59E-04	7.83E-05
		BG0316	12 026	1.71E-03	1.42E-04	BG0316	12 248	1.35E-03	1.10E-04
		BG0316	12 026	1.16E-03	9.66E-05	BG0316	12 248	8.42E-04	6.87E-05
		BG0316	12 026	1.18E-03	9.78E-05	BG0316	12 248	1.43E-03	1.16E-04
		BG0316	12 026	1.19E-03	9.85E-05	BG0316	12 248	9.61E-04	7.85E-05
		BG0316	12 026	9.70E-04	8.06E-05	BG0316	12 248	7.16E-04	5.84E-05
		BG0316	12 026	1.04E-03	8.64E-05	BG0316	12 248	8.57E-04	6.99E-05
		BG0316	12 026	7.84E-04	6.52E-05	BG0316	12 248	8.24E-04	6.73E-05
		BG0316	12 026	7.96E-04	6.62E-05	BG0316	12 248	1.24E-03	1.01E-04
		BG0316	12 026	1.85E-03	1.54E-04	BG0316	12 248	3.05E-03	2.49E-04
		BG0316	12 026	2.21E-03	1.84E-04	BG0316	6 959	1.71E-03	2.46E-04
		BG0316	12 026	1.15E-03	9.53E-05	BG0316	12 248	1.20E-03	9.82E-05
		BG0316	12 026	9.87E-04	8.20E-05	BG0316	12 248	1.06E-03	8.64E-05
		BG0316	12 026	8.70E-04	7.23E-05	BG0316	12 248	1.10E-03	8.98E-05
		BG0316	12 026	1.23E-03	1.02E-04	BG0316	12 248	1.17E-03	9.54E-05
		BG0316	12 026	1.35E-03	1.13E-04	BG0316	12 248	1.53E-03	1.25E-04
		BG0316	12 026	1.30E-03	1.08E-04	BG0316	12 248	7.24E-04	5.91E-05
		BG0316	12.248	9.77E-04	7.98E-05	BG0316	12 248	9.88E-04	8.07E-05
		BG0316	12 248	1.03E-03	8.38E-05	BG0316	12 248	8.12E-04	6.63E-05
		BG0316	12.248	9.45E-04	7.71E-05	BG0316	12 248	9.10E-04	7.43E-05
		BG0316	12.248	1.06E-03	8.67E-05	BG0316	12 248	2.39E-03	1.96E-04
		BG0316	12.248	1.51E-03	1.24E-04	BG0316	12 248	1.30E-03	1.06E-04
		BG0316	12.248	1.41E-03	1.15E-04	BG0316	12 248	1.25E-03	1.02E-04
		BG0316	12.248	1.06E-03	8.61E-05				
ca 3.3	Fig Tree (South Africa)	E-2	11 588	2.86E-03	2.47E-04	E-2	12 456	2.56E-03	2.05E-04
		E-2	10 407	4.94E-03	4.75E-04	E-2	12 456	2.60E-03	2.09E-04
		E-2	12 267	3.85E-03	3.14E-04	E-2	12 456	2.16E-03	1.73E-04
		E-2	12 267	2.62E-03	2.14E-04	E-2	12 456	3.04E-03	2.44E-04
		E-2	12 267	5.06E-03	4.13E-04	E-2	12 456	4.21E-03	3.38E-04
		E-2	12 267	2.67E-03	2.17E-04	E-2	12 456	3.21E-03	2.58E-04
		E-2	12 267	4.17E-03	3.40E-04	E-2	12 456	5.06E-03	4.06E-04
		E-2	12 267	4.40E-03	3.58E-04	E-2	12 493	2.30E-03	1.84E-04
		E-2	12 267	3.75E-03	3.06E-04	E-2	12 493	1.93E-03	1.54E-04
		E-2	12 267	4.31E-03	3.51E-04	E-2	12 493	1.85E-03	1.48E-04
		E-2	12 267	4.16E-03	3.39E-04	E-2	12 493	2.79E-03	2.24E-04
		E-2	12 267	4.90E-03	4.06E-04	E-2	12 468	2.71E-03	2.17E-04
		E-2	12 267	2.58E-03	2.10E-04	E-2	12 468	4.02E-03	3.22E-04
		E-2	12 267	4.57E-03	3.72E-04	E-2	12 468	2.47E-03	1.98E-04
		E-2	12 267	5.08E-03	4.14E-04	E-2	12 468	2.63E-03	2.11E-04
		E-2	12 267	2.77E-03	2.26E-04	E-2	12 468	3.44E-03	2.76E-04
		E-2	12 267	3.05E-03	2.48E-04	E-2	12 468	3.19E-03	2.56E-04

Table cont.

ca 3.3	Fig Tree (South Africa)	E-2	12 267	2 92E-03	2 38E-04	E-2	12 468	2 22E-03	1 78E-04
		E-2	12 493	5 04E-03	4 04E-04	E-2	12 493	3 75E-03	3 00E-04
		E-2	12 456	2.31E-03	1 85E-04	E-2	12 493	2.79E-03	2 24E-04
		E-2	12.456	4 00E-03	3.21E-04	E-2	12 493	5.39E-03	4 31E-04
		E-2	12 456	2 39E-03	1 92E-04	E-2	12 493	3 36E-03	2 69E-04
		E-2	12 456	3 40E-03	2 73E-04	E-2	12 493	2 81E-03	2 25E-04
		E-2	12 456	3 18E-03	2.55E-04				
2.74-2.75	Carajas Formation (Brazil)	1 sample	12.377	7.60E-05	6.14E-06		12.252	7.68E-05	6 27E-06
			12 377	6.15E-05	4.97E-06		12.257	2.64E-04	2 15E-05
			12 381	1.01E-04	8.12E-06		12 280	4.12E-05	3 36E-06
			12 381	9 35E-05	7 56E-06		12.367	6.12E-05	4 95E-06
			12.381	5.13E-05	4.14E-06		12.367	4.31E-05	3 49E-06
			12 381	5 64E-05	4 56E-06		12.331	6.44E-05	5.22E-06
			12 381	6 27E-05	5 06E-06		12 331	6.17E-05	5 00E-06
			12 277	7.17E-05	5.84E-06		12.331	1.10E-04	8.91E-06
			12 362	7.21E-05	5.83E-06		12.301	2.85E-05	2.31E-06
			12 360	6.93E-05	5.61E-06		12.301	7.79E-05	6 33E-06
			12 360	6.70E-05	5.42E-06		12.301	7.50E-05	6.09E-06
			12.360	7.65E-05	6.19E-06		12.301	4.36E-05	3.55E-06
			12.360	9 00E-05	7.28E-06		12.326	8.20E-05	6.65E-06
			12 360	4.60E-05	3.72E-06		12.326	2.34E-04	1 90E-05
			12 498	4.23E-05	3.38E-06		12 276	5.71E-05	4.65E-06
			12.498	5.83E-05	4.66E-06		12.276	6.29E-05	5.12E-06
			12 360	9 75E-05	7 88E-06		12 276	5.40E-05	4.40E-06
			12 360	6 58E-05	5.32E-06		12 276	9.10E-05	7.41E-06
			12 360	7 04E-05	5.69E-06		12 310	4.86E-05	3.94E-06
			12 360	5.66E-05	4.58E-06		12.232	8.26E-05	6 76E-06
			12 360	3.65E-05	2.95E-06		12.259	7.19E-05	5 87E-06
			12 359	5.93E-05	4 80E-06		12 260	4.28E-05	3 49E-06
			12 359	5.67E-05	4 59E-06		12 303	8.28E-05	6 73E-06
			12.365	7.41E-05	5.99E-06		12 303	8.69E-05	7 06E-06
			12 365	8.31E-05	6 72E-06		12 303	8.96E-05	7.28E-06
			12 365	6 36E-05	5 14E-06		12 303	5.26E-05	4.28E-06
			12 360	8.89E-05	7 20E-06		12.303	9.52E-05	7.74E-06
			12.360	6.29E-05	5.09E-06		12 338	5.33E-05	4.32E-06
			12 327	7.62E-05	6 18E-06		12 338	3.08E-05	2.50E-06
			12 327	6.19E-05	5 02E-06		12 338	6.30E-05	5.11E-06
			12 296	7.19E-05	5.85E-06		12.338	8.59E-05	6 96E-06
			12.296	6.70E-05	5.45E-06		12.338	5.93E-05	4.81E-06
			12 306	6.71E-05	5.46E-06		12.338	7.16E-05	5 80E-06
			12 299	1.64E-04	1.33E-05		12.338	7.05E-05	5 72E-06
			12 312	1 55E-04	1.26E-05		12.337	7.85E-05	6.37E-06
			12.289	5.21E-05	4.24E-06				
2.72	Upper Deloro Assemblage (Ontario)	1 sample	12 802	3.55E-03	2 77E-04		12 733	3 64E-03	2 86E-04
			12 760	4 10E-03	3 21E-04		12 733	4 27E-03	3 35E-04
			12 760	4.16E-03	3.26E-04		12.747	4 90E-03	3.84E-04
			12 786	3 39E-03	2 65E-04		12 733	3.57E-03	2 80E-04
			12 760	4 42E-03	3 46E-04		12 747	3.94E-03	3 09E-04
			12 760	3 98E-03	3 12E-04		12 747	4 19E-03	3.28E-04
			12 760	4 11E-03	3 22E-04		12 733	4 73E-03	3 71E-04
			12 760	4.73E-03	3.71E-04		12 747	4.44E-03	3 48E-04
			12 760	4.34E-03	3 40E-04		12 733	4 40E-03	3 46E-04
			12 760	3 59E-03	2 82E-04		12 747	4 97E-03	3 90E-04
			12 760	4 69E-03	3 68E-04		12 733	4 20E-03	3.30E-04
			12 760	3 95E-03	3.10E-04		12.747	4.39E-03	3.45E-04
			12 760	3 64E-03	2 85E-04		12 747	4 86E-03	3 81E-04
			12 677	4 48E-03	3.53E-04		12 733	5 60E-03	4 40E-04
			12 677	4 45E-03	3.51E-04		12 760	4.77E-03	3 74E-04
			12.772	4 74E-03	3.71E-04		12 760	4.54E-03	3 56E-04
			12 760	3.48E-03	2.72E-04		12.747	5.53E-03	4 34E-04
			12 719	3 47E-03	2 72E-04		12 733	4.29E-03	3 37E-04
			12 719	4 23E-03	3 33E-04		12 760	3.20E-03	2.51E-04
			12 719	4 18E-03	3 29E-04		12 760	4.24E-03	3.32E-04
			12 719	4 50E-03	3.54E-04		12.747	4 70E-03	3 69E-04
			12 719	3 65E-03	2 87E-04		12 747	4 56E-03	3 58E-04
			12 719	4.15E-03	3.27E-04		12 733	4.70E-03	3.69E-04
			12 719	4 47E-03	3.51E-04		12 747	4.91E-03	3 85E-04
			12 719	3.57E-03	2 81E-04		12 747	4 70E-03	3 69E-04
			12.719	3.99E-03	3.14E-04		12 733	4.10E-03	3 22E-04
			12.719	5.07E-03	3 99E-04		12 747	4.46E-03	3 50E-04
			12 719	4 20E-03	3.30E-04		12 733	4 70E-03	3 69E-04
			12 719	3.79E-03	2 98E-04		12 733	2 63E-03	2 07E-04
			12 719	4.11E-03	3.23E-04		12 747	2 48E-03	1 94E-04
			12 719	5.77E-03	4 53E-04		12 735	3 38E-03	2 65E-04
			12 719	3.91E-03	3 07E-04		12 736	3.22E-03	2 53E-04

Table cont.

2.72	Upper Deloro Assemblage (Ontario)	1 sample	12.719	4.13E-03	3.24E-04		12.736	2.99E-03	2.35E-04
			12.719	4.69E-03	3.69E-04		12.736	2.90E-03	2.27E-04
			12.733	4.74E-03	3.72E-04		12.736	3.39E-03	2.66E-04
			12.733	4.35E-03	3.41E-04		12.747	3.44E-03	2.70E-04
			12.733	4.81E-03	3.78E-04		12.747	3.50E-03	2.75E-04
			12.733	3.84E-03	3.02E-04		12.747	3.77E-03	2.96E-04
			12.733	4.86E-03	3.82E-04		12.747	2.27E-03	1.78E-04
			12.747	4.04E-03	3.17E-04		12.744	2.20E-03	1.73E-04
			12.747	4.23E-03	3.32E-04		12.744	1.92E-03	1.50E-04
			12.747	4.79E-03	3.76E-04		12.744	1.63E-03	1.28E-04
			12.747	4.43E-03	3.47E-04				
2.7	Temagami BIF (Hunter Mine) (Ontario)	1 sample	12.846	3.70E-05	2.88E-06		12.804	3.87E-05	3.02E-06
			12.846	7.89E-05	6.14E-06		12.804	6.17E-05	4.82E-06
			12.846	9.17E-05	7.14E-06		12.804	1.27E-04	9.90E-06
			12.869	4.80E-05	3.73E-06		12.804	3.95E-05	3.09E-06
			12.833	9.85E-05	7.67E-06		12.804	6.10E-05	4.76E-06
			12.833	5.08E-05	3.96E-06		12.804	5.96E-05	4.66E-06
			12.814	4.21E-05	3.28E-06		12.804	1.40E-04	1.09E-05
			12.907	3.46E-05	2.68E-06		12.804	4.80E-05	3.75E-06
			12.747	4.63E-05	3.64E-06		12.804	6.37E-05	4.98E-06
			12.883	4.19E-05	3.25E-06		12.804	6.32E-05	4.94E-06
			12.740	3.24E-05	2.54E-06		12.804	7.38E-05	5.76E-06
			12.804	4.07E-05	3.18E-06		12.804	4.79E-05	3.74E-06
			12.740	1.18E-04	9.25E-06		12.804	7.36E-05	5.75E-06
			12.472	6.05E-05	4.85E-06		12.804	9.70E-05	7.57E-06
			12.406	2.57E-05	2.07E-06		12.804	1.02E-04	7.96E-06
			12.833	3.87E-05	3.01E-06		12.804	5.49E-05	4.28E-06
			12.832	4.34E-05	3.39E-06		12.804	7.70E-05	6.01E-06
			12.804	5.83E-05	4.55E-06		12.804	6.34E-05	4.95E-06
			12.804	3.73E-05	2.91E-06		12.804	5.72E-05	4.47E-06
			12.804	4.41E-05	3.45E-06		12.804	5.15E-05	4.02E-06
			12.804	3.51E-05	2.74E-06		12.804	7.48E-04	5.84E-05
			12.804	6.58E-05	5.14E-06		12.804	6.65E-05	5.19E-06
			12.804	5.20E-05	4.06E-06		12.804	7.89E-05	6.16E-06
			12.804	5.78E-05	4.51E-06		12.804	3.73E-05	2.91E-06
			12.804	3.63E-05	2.83E-06		12.804	6.19E-05	4.83E-06
			12.804	2.81E-05	2.20E-06		12.804	9.30E-05	7.27E-06
			12.804	4.82E-05	3.77E-06		12.804	1.62E-04	1.26E-05
			12.804	2.40E-04	1.88E-05		10.995	7.58E-05	6.90E-06
			12.804	8.57E-05	6.69E-06		12.804	4.02E-05	3.14E-06
			12.804	1.01E-04	7.90E-06		12.804	7.16E-05	5.59E-06
			12.804	6.49E-05	5.07E-06		12.804	5.32E-05	4.15E-06
			12.804	7.16E-05	5.59E-06		12.804	7.43E-05	5.80E-06
			12.804	4.74E-05	3.70E-06		12.804	7.45E-05	5.82E-06
			12.804	5.98E-05	4.67E-06		12.804	2.90E-05	2.26E-06
			12.804	5.03E-05	3.93E-06		12.804	2.35E-05	1.84E-06
			12.804	7.21E-05	5.63E-06		12.804	7.70E-05	6.01E-06
			12.804	8.13E-05	6.35E-06		12.804	7.51E-05	5.87E-06
			12.804	4.07E-05	3.18E-06		12.804	6.24E-05	4.87E-06
			12.804	4.21E-05	3.29E-06		12.804	1.27E-04	9.91E-06
			12.804	4.12E-05	3.22E-06		12.804	8.91E-05	6.96E-06
			12.804	2.42E-05	1.89E-06		12.804	9.88E-05	7.72E-06
			12.804	5.04E-05	3.94E-06		12.804	4.02E-05	3.14E-06
			12.804	5.28E-05	4.13E-06		12.804	6.65E-05	5.19E-06
			12.804	5.28E-05	4.13E-06		12.804	1.02E-04	8.00E-06
			12.804	4.62E-05	3.61E-06		12.804	4.92E-05	3.85E-06
			12.804	1.01E-04	7.92E-06		12.804	7.55E-05	5.89E-06
			12.804	5.18E-05	4.05E-06		12.804	7.33E-05	5.72E-06
			12.804	6.20E-05	4.84E-06		12.804	6.03E-05	4.71E-06
			12.804	1.03E-04	8.05E-06		12.804	7.38E-05	5.76E-06
			12.804	6.66E-05	5.20E-06		12.804	7.63E-05	5.96E-06
			12.804	1.43E-04	1.12E-05		12.804	5.03E-05	3.93E-06
2.48	Dales Gorge (Australia)	1 sample	12.174	3.38E-04	2.78E-05		12.804	2.63E-04	2.06E-05
			12.095	2.90E-04	2.39E-05		12.192	1.23E-04	1.01E-05
			12.109	2.78E-04	2.30E-05		12.192	1.82E-04	1.50E-05
			12.109	2.36E-04	1.95E-05		12.192	8.35E-05	6.85E-06
			12.109	2.15E-04	1.78E-05		12.192	1.03E-04	8.43E-06
			12.109	9.42E-05	7.78E-06		12.192	1.74E-04	1.43E-05
			12.109	1.63E-04	1.35E-05		12.192	9.13E-05	7.49E-06
			12.109	3.45E-04	2.85E-05		12.192	9.88E-05	8.11E-06
			12.109	1.38E-04	1.14E-05		12.192	8.11E-04	6.65E-05
			12.825	1.16E-04	9.06E-06		12.192	7.55E-05	6.19E-06
			12.817	1.45E-04	1.13E-05		12.192	2.06E-04	1.69E-05
			12.804	1.25E-04	9.78E-06		12.192	1.13E-04	9.27E-06
			12.804	6.46E-05	5.04E-06		12.192	1.41E-04	1.15E-05
			12.136	2.50E-04	2.06E-05		12.818	3.70E-04	2.88E-05
			12.136	1.76E-04	1.45E-05		12.192	1.95E-04	1.60E-05

Table cont

2.48	Dales Gorge (Australia)	1 sample	12.818	2.79E-04	2.18E-05		12.192	1.45E-04	1.19E-05
			12.818	1.29E-04	1.00E-05		12.192	2.36E-04	1.93E-05
			12.818	1.72E-04	1.34E-05		12.192	4.32E-04	3.55E-05
			12.818	7.09E-05	5.53E-06		12.192	2.08E-04	1.70E-05
			12.192	1.52E-04	1.25E-05		12.192	1.81E-04	1.49E-05
			12.192	2.92E-04	2.40E-05		12.192	1.14E-04	9.34E-06
			12.192	1.89E-04	1.55E-05		12.192	1.69E-04	1.39E-05
			12.818	2.10E-04	1.64E-05		12.192	1.15E-04	9.42E-06
			12.818	1.39E-04	1.08E-05		12.818	3.14E-04	2.45E-05
			12.248	1.18E-04	9.64E-06		12.818	1.46E-04	1.14E-05
			12.818	1.26E-04	9.85E-06		12.192	1.74E-04	1.43E-05
			12.192	1.87E-04	1.54E-05		12.192	1.91E-04	1.57E-05
			12.192	1.71E-04	1.40E-05		12.192	5.16E-05	4.23E-06
			12.192	1.72E-04	1.41E-05		12.818	3.42E-04	2.67E-05
			12.192	7.99E-04	6.55E-05		12.818	2.95E-04	2.30E-05
			12.818	4.96E-05	3.87E-06		12.192	2.18E-04	1.79E-05
			12.192	1.93E-04	1.58E-05		12.192	1.10E-04	9.00E-06
			12.192	2.11E-04	1.73E-05		12.192	2.01E-04	1.65E-05
			12.192	2.71E-05	2.22E-06		12.192	1.42E-04	1.17E-05
			12.192	1.76E-04	1.45E-05		12.192	1.95E-04	1.60E-05
			12.818	9.20E-05	7.18E-06		12.192	3.18E-04	2.60E-05
			12.818	9.08E-05	7.08E-06		12.192	1.55E-04	1.27E-05
			12.818	1.50E-04	1.17E-05		12.192	1.91E-04	1.57E-05
			12.192	2.02E-04	1.65E-05		12.192	1.32E-04	1.08E-05
			12.192	1.32E-04	1.09E-05		12.192	2.13E-04	1.75E-05
			12.192	7.04E-05	5.77E-06		12.192	4.22E-04	3.46E-05
			12.192	1.27E-04	1.04E-05		12.192	1.81E-04	1.48E-05
			12.192	1.24E-04	1.01E-05		12.192	3.92E-04	3.22E-05
			12.192	1.06E-04	8.72E-06		12.192	2.38E-04	1.95E-05
			12.790	1.03E-04	8.09E-06		12.192	2.35E-04	1.93E-05
			12.790	1.03E-04	8.06E-06		12.818	3.27E-05	2.55E-06
			12.804	7.94E-05	6.20E-06		12.818	3.48E-04	2.71E-05
			12.818	6.24E-05	4.87E-06		12.192	2.50E-04	2.05E-05
			12.804	6.36E-05	4.96E-06		12.192	2.66E-04	2.19E-05
2.47	Kuruman (South Africa)	1 sample	12.754	4.21E-05	3.30E-06		12.735	2.33E-05	1.83E-06
			12.754	1.98E-05	1.55E-06		12.735	3.15E-05	2.48E-06
			12.754	4.58E-05	3.59E-06		12.763	2.32E-05	1.82E-06
			12.754	3.92E-05	3.07E-06		12.619	5.86E-05	4.64E-06
			12.754	1.52E-05	1.19E-06		12.735	1.23E-04	9.62E-06
			12.754	2.79E-05	2.19E-06		12.735	5.67E-05	4.46E-06
			12.754	3.70E-05	2.90E-06		12.693	3.73E-05	2.94E-06
			12.754	2.18E-05	1.71E-06		12.693	7.99E-05	6.30E-06
			12.754	1.91E-05	1.50E-06		12.693	4.53E-05	3.57E-06
			12.754	2.90E-05	2.27E-06		12.693	3.34E-05	2.63E-06
			12.754	2.25E-05	1.76E-06		12.693	9.17E-05	7.22E-06
			12.754	2.27E-05	1.78E-06		12.693	1.05E-04	8.26E-06
			12.754	2.98E-05	2.34E-06		12.693	6.97E-05	5.49E-06
			12.754	2.76E-05	2.16E-06		12.693	5.28E-05	4.16E-06
			12.754	2.88E-05	2.26E-06		12.693	7.63E-05	6.01E-06
			12.754	2.81E-05	2.20E-06		12.693	5.01E-05	3.95E-06
			12.754	2.83E-05	2.22E-06		12.693	2.49E-05	1.96E-06
			12.754	3.31E-05	2.59E-06		12.693	3.37E-05	2.66E-06
			12.754	1.48E-05	1.16E-06		12.693	7.00E-05	5.52E-06
			12.686	3.42E-05	2.70E-06		12.721	6.61E-05	5.20E-06
			12.686	3.03E-05	2.39E-06		12.721	2.20E-05	1.73E-06
			12.693	4.89E-05	3.85E-06		12.721	6.76E-05	5.32E-06
			12.693	3.51E-05	2.77E-06		12.721	9.61E-05	7.55E-06
			12.735	4.19E-05	3.29E-06		12.721	7.67E-05	6.03E-06
			12.735	2.83E-05	2.22E-06		12.721	7.02E-05	5.52E-06
			12.721	4.62E-05	3.63E-06		12.721	1.11E-04	8.76E-06
			12.721	3.19E-05	2.50E-06		12.735	1.03E-04	8.09E-06
			12.721	1.64E-05	1.29E-06		12.735	1.05E-04	8.23E-06
			12.721	7.24E-05	5.69E-06		12.735	7.68E-05	6.03E-06
			12.735	5.98E-05	4.70E-06				
1.9	Negaunee	1 sample	11.830	9.00E-05	7.60E-06		12.248	1.23E-04	1.01E-05
			11.830	8.64E-05	7.30E-06		12.248	4.45E-05	3.63E-06
			11.830	3.94E-05	3.33E-06		12.248	8.23E-05	6.72E-06
			11.830	3.97E-05	3.36E-06		12.248	7.31E-04	5.97E-05
			11.830	4.79E-05	4.05E-06		12.248	6.87E-05	5.61E-06
			11.830	1.04E-03	8.75E-05		12.248	6.92E-05	5.65E-06
			11.830	6.68E-05	5.65E-06		12.248	3.87E-05	3.16E-06
			12.248	6.58E-05	5.37E-06		12.248	5.13E-05	4.19E-06
			12.248	8.77E-05	7.16E-06		12.248	1.08E-04	8.82E-06
			12.248	6.87E-05	5.61E-06		12.248	9.23E-05	7.54E-06
			12.248	1.07E-04	8.71E-06		12.248	8.33E-05	6.80E-06
			12.248	2.12E-04	1.73E-05		12.248	4.58E-05	3.74E-06
			12.248	1.80E-04	1.47E-05		12.248	7.14E-05	5.83E-06

Table cont

1.9	Negaunee	1 sample	12.248	1.07E-04	8.71E-06		12.248	5.76E-05	4.70E-06
			12.248	4.02E-04	3.28E-05		12.248	2.37E-05	1.93E-06
			12.248	9.49E-04	7.75E-05		12.248	3.77E-05	3.07E-06
			12.248	8.84E-05	7.22E-06		12.248	4.99E-04	4.07E-05
			12.248	5.55E-05	4.54E-06		12.248	6.52E-04	5.32E-05
			12.248	4.57E-05	3.73E-06		12.248	7.38E-05	6.02E-06
			12.248	5.09E-05	4.16E-06		12.248	7.45E-05	6.08E-06
			12.248	1.12E-04	9.15E-06		12.248	9.66E-05	7.89E-06
			12.248	5.08E-05	4.15E-06		12.248	7.00E-05	5.72E-06
			12.248	7.03E-04	5.74E-05		12.248	1.02E-04	8.32E-06
			12.248	4.17E-05	3.41E-06		12.248	8.49E-05	6.93E-06
			12.248	8.38E-05	6.84E-06		12.248	6.29E-05	5.13E-06
			12.248	6.90E-04	5.63E-05				
0.55	Yerbal Formation (Uruguay)	1 sample	12.387	3.54E-04	2.85E-05		12.331	1.41E-04	1.14E-05
			12.359	1.18E-05	9.52E-07		12.331	1.03E-04	8.34E-06
			12.331	2.70E-05	2.19E-06		12.331	3.87E-05	3.14E-06
			12.387	1.45E-05	1.17E-06		12.331	3.52E-06	2.85E-07
			12.373	1.77E-05	1.43E-06		12.331	1.15E-04	9.36E-06
			12.317	1.44E-05	1.17E-06		12.331	5.32E-05	4.31E-06
			12.248	3.50E-05	2.85E-06		12.331	5.05E-05	4.09E-06
			12.331	8.57E-06	6.95E-07		12.331	1.51E-05	1.23E-06
			12.331	2.11E-05	1.71E-06		12.331	9.74E-05	7.90E-06
			12.331	7.39E-05	6.00E-06		12.331	7.67E-05	6.22E-06
			12.331	3.17E-05	2.57E-06		12.331	4.69E-05	3.81E-06
			12.331	1.17E-06	9.52E-08		12.331	3.52E-05	2.85E-06
			12.331	3.52E-05	2.85E-06		12.331	4.67E-06	3.79E-07
			12.331	1.31E-05	1.07E-06		12.331	6.91E-05	5.60E-06
			12.331	1.57E-04	1.28E-05		12.331	3.17E-05	2.57E-06
			12.331	3.52E-06	2.85E-07		12.331	3.52E-04	2.85E-05
			12.331	1.31E-04	1.07E-05		12.331	5.69E-06	4.62E-07
			12.331	2.32E-05	1.88E-06		12.331	5.08E-05	4.12E-06
			12.331	2.70E-05	2.19E-06		12.331	3.64E-05	2.95E-06
			12.331	1.53E-05	1.24E-06		12.331	3.52E-05	2.85E-06
			12.331	2.81E-05	2.28E-06		12.331	3.76E-04	3.05E-05
			12.331	1.53E-04	1.24E-05		12.331	1.46E-05	1.18E-06
			12.331	2.70E-05	2.19E-06		12.331	8.57E-05	6.95E-06
			12.331	3.52E-05	2.85E-06		12.331	3.52E-06	2.85E-07
			12.331	6.78E-06	5.50E-07		12.331	7.39E-05	6.00E-06
			12.331	1.16E-04	9.39E-06		12.331	5.28E-05	4.28E-06
			12.331	3.50E-06	2.84E-07		12.331	3.52E-04	2.85E-05
			12.331	1.47E-05	1.20E-06		12.331	1.16E-04	9.39E-06
			12.331	1.45E-05	1.17E-06		12.331	3.52E-05	2.85E-06
			12.331	2.35E-06	1.90E-07		12.331	3.52E-06	2.85E-07
			12.331	3.52E-04	2.85E-05		12.331	1.17E-06	9.52E-08
			12.331	1.09E-05	8.85E-07		12.331	3.52E-06	2.85E-07
			12.331	1.53E-05	1.24E-06		12.331	4.67E-06	3.79E-07
			12.331	1.09E-05	8.85E-07		12.331	5.32E-05	4.31E-06
			12.331	1.53E-05	1.24E-06		12.331	3.50E-06	2.84E-07
			12.331	9.74E-05	7.90E-06		12.331	8.09E-06	6.56E-07
			12.331	1.17E-04	9.52E-06		12.331	1.53E-06	1.24E-07
			12.331	2.35E-04	1.90E-05		12.331	2.23E-05	1.81E-06
			12.331	3.52E-04	2.85E-05		12.331	9.15E-06	7.42E-07
			12.331	3.40E-06	2.76E-07		12.331	2.46E-04	2.00E-05
			12.331	2.87E-05	2.33E-06		12.331	1.09E-05	8.85E-07
			12.331	5.61E-05	4.55E-06		12.331	5.87E-06	4.76E-07
			12.331	6.76E-05	5.48E-06		12.331	9.15E-05	7.42E-06
			12.331	6.22E-05	5.04E-06		12.331	8.57E-05	6.95E-06
			12.331	3.50E-05	2.84E-06		12.331	7.39273E-06	5.995E-07

1. O'Neil, J. *et al.* in *Earth's Oldest Rocks* (eds van Kranendonk, J., Smithies, H. & Bennett, V.C.) 219-254 (2007).
2. Dymek, R. & Klein, C. Chemistry, petrology and origin of banded iron-formation lithologies from the 3800 Ma Isua supracrustal belt, west Greenland. *Precamb. Res.* **39**, 247-302 (1988).
3. Bolhar, R., Kamber, B.S., Moorbath, S, Fedo, C.F. & Whitehouse, M.J. Characterisation of early Archaean chemical sediments by trace element signatures. *Earth Planet. Sci. Lett.* **222**, 43-60 (2004).
4. Gole, M.J. Archean banded iron-formations, Yilgarn block, Western Australia. *Econ. Geol.* **76**, 1954-1974 (1981).

5. Lascelles, D. The Mount Gibson banded iron formation-hosted magnetite deposit: Two distinct processes for the origin of high-grade iron ore. *Econ. Geol.* **101**, 651-666 (2006).
6. Klein, C. & Ladeira, A. E. Petrography and geochemistry of the least altered banded iron-formation of the Archean Carajás Formation, northern Brazil. *Econ. Geol.* **97**, 643-651 (2002).
7. Majumder, T., Chakraborty, K.L. & Bhattacharyya, A. Geochemistry of banded iron formations of Orissa, India. *Min. Dep.* **17**, 107-118 (1982).
8. Klein, C. & Ladeira, E.A. Geochemistry and petrology of some Proterozoic banded iron-formations of the Quadrilátero Ferrífero, Minas Gerais, Brazil. *Econ. Geol.* **95**, 405-428 (2000).
9. Spier, C.A., de Oliveira, S.M.B., Sial, A.N. & Rios, F.J. Geochemistry and genesis of the banded iron formations of the Cauê Formation, Quadrilátero Ferrífero, Minas Gerais, Brazil. *Precamb. Res.* **152**, 170-206 (2007).
10. Klein, C. & Beukes, N.J. Geochemistry and sedimentology of a facies transition from limestone to iron-formation deposition in the Early Proterozoic Transvaal Supergroup, South Africa. *Econ. Geol.* **84**, 1733-1774 (1989).
11. Horstmann, U.E. & Häblich, I.W. Chemical composition of banded iron-formation of the Griqualand west sequence, Northern Cape Province, South Africa, in comparison with other Precambrian iron formations. *Precamb. Res.* **72**, 109-145 (1995).
12. Beukes, N.J. & Klein, C. Geochemistry and sedimentology of a facies transition from microbanded to granular iron-formation in the early Proterozoic Transvaal Supergroup, South Africa. *Precamb. Res.* **47**, 99-139 (1990).
13. Polteau, S., Moore, J.M. & Tsikos, H. The geology and geochemistry of the Palaeoproterozoic Makganyene diamictite. *Precamb. Res.* **148**, 257-274 (2006).
14. Tsikos, H. & Moore, J. M. Petrography and geochemistry of the Paleoproterozoic Hotazel iron-formation, Kalahari Manganese field, South Africa: Implications for Precambrian manganese metallogenesis. *Econ. Geol.* **92**, 87-97 (1997).

15. Klein, C. & Beukes, N.J. Sedimentology and geochemistry of the glaciogenic late Proterozoic Rapitan iron-formation in Canada. *Econ. Geol.* **88**, 542-565 (1993).
16. Klein, C. & Ladeira, E.A. Geochemistry and mineralogy of Neoproterozoic banded iron-formations and some selected, siliceous manganese formations from the Urucum District, Mato Grosso do Sul, Brazil. *Econ. Geol.* **99**, 1233-1244 (2004).
17. Lottermoser, B.G. & Ashley, P.M. Geochemistry, petrology and origin of Neoproterozoic ironstones in the eastern part of the Adelaide Geosyncline, South Australia. *Precamb. Res.* **101**, 49-67 (2000).
18. Breitkopf, J.H. Iron formations related to mafic volcanism and ensialic rifting in the southern margin zone of the Damara Orogen, Namibia. *Precamb. Res.* **38**, 111-130 (1988).

Table S2. Statistical summary of data employed in this study. NBA – new bulk analyses, LV – literature values, LA – laser ablation.

Age (Ga)	Unit	Data Source	Count	Average	Maximum	Minimum	Standard Deviation	95% Confidence Interval
3.80	Nuvvuagittuq (Canada)	LV	5	2.04E-04	3.42E-04	1.39E-04	8.08E-05	7.09E-05
3.75	Isua (Greenland)	LA (97-23)	84	8.58E-05	1.30E-04	5.53E-05	1.70E-05	3.64E-06
3.75	Isua (Greenland)	LA (97-26)	79	3.41E-04	4.53E-04	2.51E-04	4.04E-05	8.91E-06
3.75	Isua (Greenland)	LA (E-1)	55	1.95E-04	2.45E-04	1.39E-04	3.10E-05	8.21E-06
3.75	Isua (Greenland)	LV	24	1.44E-04	4.54E-04	3.96E-05	9.00E-05	3.60E-05
3.75	Isua (Greenland)	NBA	9	1.66E-04	3.46E-04	4.77E-05	1.29E-04	8.41E-05
3.75	Ugpik (Greenland)	LV	1	1.24E-04				
3.30	Fig Tree (South Africa)	LA (BG0316)	49	1.04E-04	2.49E-04	5.84E-05	4.47E-05	1.25E-05
3.30	Fig Tree (South Africa)	LA (E-2)	47	2.76E-04	4.75E-04	1.48E-04	8.32E-05	2.38E-05
2.85	Mount Gibson (Australia)	LV	18	1.19E-04	1.97E-04	7.10E-05	4.37E-05	2.02E-05
2.85	Yilgarn Block (Australia)	LV	6	1.19E-04	3.28E-04	1.96E-05	1.28E-04	1.03E-04
2.76	Temagami - Sherman (Canada)	NBA	4	4.51E-05	6.07E-05	2.24E-05	1.61E-05	1.58E-05
2.75	Carajas Formation (Brazil)	LA	71	6.08E-06	2.15E-05	2.31E-06	3.06E-06	7.12E-07
2.75	Carajas Formation (Brazil)	LV	6	6.36E-05	1.22E-04	1.87E-05	4.62E-05	3.70E-05
2.72	Temagami Hwy 11 (Canada)	NBA	2	8.72E-06	1.07E-05	6.76E-06	2.78E-06	3.85E-06
2.72	Upper Deloro (Canada)	LA	85	3.20E-04	4.53E-04	1.28E-04	6.08E-05	1.29E-05
2.72	Upper Deloro (Canada)	NBA	2	2.83E-05	4.98E-05	6.78E-06	3.04E-05	4.22E-05
2.70	Beardmore Area (Canada)	NBA	3	3.21E-05	5.92E-05	1.52E-05	2.38E-05	2.69E-05
2.70	Hunter Mine (Canada)	LA	103	5.69E-06	5.84E-05	1.84E-06	5.80E-06	1.12E-06
2.70	Orissa (India)	LV	1	3.45E-05				
2.50	Quadrilatero Ferrifero (Brazil)	LV	42	3.85E-05	9.48E-05	8.06E-06	2.26E-05	6.82E-06
2.48	Dales Gorge (Australia)	LA	98	1.55E-05	6.65E-05	2.22E-06	1.02E-05	2.02E-06
2.48	Dales Gorge (Australia)	NBA	10	5.59E-06	1.25E-05	6.31E-07	3.47E-06	2.15E-06
2.47	Kuruman (South Africa)	LA	59	3.81E-06	9.62E-06	1.16E-06	2.18E-06	5.55E-07
2.47	Kuruman (South Africa)	LV	42	1.09E-04	2.35E-04	9.79E-06	4.76E-05	1.44E-05
2.43	Griquatown (South Africa)	LV	12	7.97E-05	1.35E-04	9.87E-06	5.23E-05	2.96E-05
2.42	Reeinekke (South Africa)	LV	1	1.05E-04				
2.30	Hotazel (South Africa)	LV	5	1.30E-04	1.49E-04	1.17E-04	1.18E-05	1.04E-05
2.00	Loch Maree (Scotland)	NBA	1	1.11E-04				
1.90	Negaunee (Canada)	LA	51	1.44E-05	8.75E-05	1.93E-06	2.04E-05	5.59E-06
1.88	Gunflint (Canada)	NBA	4	1.49E-05	1.63E-05	1.43E-05	9.25E-07	9.07E-07
0.74	Rapitan (Canada)	LV	2	2.82E-05	3.24E-05	2.41E-05	5.85E-06	8.11E-06
0.73	Braemar (Australia)	LV	5	1.60E-05	2.88E-05	8.62E-06	8.21E-06	7.20E-06
0.73	Urucum (Brazil)	LV	4	2.22E-05	2.81E-05	1.86E-05	4.24E-06	4.15E-06
0.70	Chuos (Namibia)	LV	2	6.87E-05	8.80E-05	4.94E-05	2.73E-05	3.79E-05
0.55	Yerbal (Uruguay)	LA	90	5.32E-06	3.05E-05	9.52E-08	7.45E-06	1.54E-06
0.55	Yerbal (Uruguay)	NBA	3	4.58E-06	5.05E-06	3.91E-06	5.99E-07	6.78E-07

Table S3. Data table of Precambrian komatiite bearing greenstone belts from Condie[1] and de Wit and Ashwal[2], modified to include more recent geochronological data[3-7].

Komatiite Location	Age (Ga)
Aldan Craton	
Tungurcha	3.1
Olondo	3.0
Amazonian Craton	
Carajas	2.9
Eastern Dharwar Craton	
Kolar	2.7
Gawler Craton	
Harris	2.51
Kaapvaal Craton	
Barberton	3.46
Commondale	3.33
Pietersberg	3.03
Karelian Craton	
Kuhmo	2.75
Hattu	2.79
Lapland	2.21
Outokumpu	2.4
Kostamukasha	2.74
North Atlantic Craton	
Isua	3.75
North China Craton	
Quingyuan	2.53
Phanerozoic Komatiites	
Gorgona Island	0.09
Pilbara Craton	
East Pilbara	
Coontarunah	3.51
Warrawoona	3.45
Kelly	3.35
West Pilbara	
Ruth Well	3.25
Negri	2.95

Komatiite Location *cont.*	Age (Ga) *cont.*
Sao Francisco Craton	
Quadrilatero Ferrifero	2.75
Rio Itapicuru	2.06
Slave Craton	
Hackett River	2.69
Superior Craton	
Uchi	2.85
Abitibi (multiple pulses)	2.74
Abitibi (multiple pulses)	2.72
Abitibi (multiple pulses)	2.71
Trans Hudson Orogen	
Lynn Lake	1.9
Flin Flon	1.9
Ungava Orogen	
Cape Smith	1.9
West African Craton	
Sula	2.87
Nagondi	2.15
Western Dharwar Craton	
Chitradurga	2.80
Wyoming Craton	
South Pass	2.69
Yilgarn Craton	
Youanmi Terrane	
Murchison Domain	2.95
Southern Cross Domain	2.95
Eastern Goldfields Superterrane	
Kalgoorlie Terrane (multiple pulses)	2.71
Kalgoorlie Terrane (multiple pulses)	2.7
Kalgoorlie Terrane (multiple pulses)	2.69
Laverton Domain	2.8
Zimbabwe Craton	
Belingwe	2.9
	2.69

1. Condie, K.C. in *Archean Crustal Evolution* (ed Condie, K.C.) 85-120 (Elsevier, 1994).
2. De Wit, M.J. & Ashwal, L.D. Greenstone belts: What are they? *S. Africa J. Geol.* **98**, 505-520 (1995).
3. Cassidy et al., 2006, Western Australian Geological Survey Record 2006/8.
4. Kositcin, N. *et al.* SHRIMP U-Pb zircon age constraints on the Late Archaean tectonostratigraphic architecture of the Eastern Goldfields Superterrane, Yilgarn Craton, Western Australia. *Precamb. Res.* **161,** 5-33 (2008).
5. Sproule, R.A., Lesher, C.M., Ayer, J.A., Thurston, P.C. & Herzberg, C.T. Spatial and temporal variations in the geochemistry of komatiites and komatiitic basalts in the Abitibi greenstone belt. *Precamb. Res.* **115**, 153-186 (2002).
6. Swain, G. *et al.* Provenance and tectonic development of the late Archaean Gawler Craton, Australia; U-Pb zircon, geochemical and Sm-Nd isotopic implications. *Precamb. Res.* **141**, 106-136 (2005).
7. Van Kranendonk, M.J., Smithies, R.H., Hickman, A.H. & Champion, D.C. Review: Secular tectonic evolution of Archean continental crust: Interplay between horizontal and vertical processes in the formation of the Pilbara Craton, Australia. *Terra Nova* **19**, 1-38 (2006).

Supplemental Discussion

Primary BIF components and post-depositional alteration

Banded iron formation (BIF) are iron rich (~20-40% Fe) and siliceous (~40-50% SiO_2) sedimentary deposits that precipitated from seawater over a 3 billion year span in Earth's history. The mineralogy of the least metamorphosed BIF consists of chert, magnetite, hematite, carbonates (siderite, dolomite-ankerite), greenalite, stilpnomelane and riebeckite[1]: the presence of both ferric and ferrous minerals gives BIF an average oxidation state of $Fe^{2.4+}$ (ref 2). It is generally agreed that none of the minerals in BIF are primary, but instead, the minerals reflect both diagenetic and metamorphic overprinting. The primary iron minerals were most likely ferric hydroxide [$Fe(OH)_3$] (also known as HFO), greenalite [$(Fe)_3Si_2O_5(OH)_4$], and siderite [$FeCO_3$][3,4,5,6]. Petrographic evidence in support of a primary HFO origin comes from transmission electron microscopy of BIF samples which show nanospheres of thin, curved hematite platelets surrounding a central void; this texture suggests that they formed by structural ordering and dehydration of colloidal iron hydroxide particles[7]. This interpretation also implies that the hematite formed during the diagenetic and/or metamorphic stage of burial, rather than during sediment accumulation.

Although the average oxidation state of $Fe^{2.4+}$ can be described by the simultaneous deposition of Fe(II) and Fe(III), the partial microbial reduction of Fe(III) to Fe(II) also contributed to this mixed oxidation state[8,9]. The diagenetic modification of Fe(III) after sedimentation to produce siderite ($FeCO_3$) and magnetite (Fe_3O_4) would require a reductant, the most likely being the organic

carbon associated with the remains of dead planktonic bacteria[10]. Certainly, the presence of magnetite as (1) disseminated grains within but obscuring sedimentary laminae, (2) laminated beds that clearly truncate sedimentary layering, (3) layer-discordant veins, and (4) cleavage fills, indicates a secondary origin[11,12], although what fraction of the magnetite formed through bacterial Fe(III) reduction or as a by-product of the reaction of kerogenous carbon with ferric hydroxide or hematite during metamorphism is unresolved. Certainly the capacity of extant hyperthermophilic *Bacteria* and *Archaea* (that branch deeply in the universal phylogenetic tree) to reduce Fe(III)[13], and the recent observations of highly negative δ^{56}Fe values in magnetite-rich BIF samples as old as 2.9 Ga[14,15], with comparable negative fractionations as observed in experimental culture with dissimilatory Fe(III)-reducing bacteria[16], point towards the antiquity of such an anaerobic respiratory pathway. Significantly, coupling the reduction of Fe(III) minerals to the oxidation of organic matter not only explains the low content of organic carbon in the BIFs (<0.5%)[17], but it also explains the abundance of light carbon isotopic signatures associated with the interlayered carbonate minerals[18,19].

It is important to consider that as the Fe-rich particles and planktonic biomass settled out of the water column, each new layer would isolate the biomass and sediment of earlier layers from the overlying sea water, and trace metal mobility in an iron oxide–rich sediment would have been limited[6,8]. Indeed, recent studies by Frost et al.[20], Whitehouse and Fedo[21] and Johnson et al.[22] have shown that despite the presence of intra-grain and intra-layer iron isotopic variability in both minimally metamorposed BIF (e.g., 2.5 Gyr old Kuruman and Dales Gorge) and

those more highly altered and metasomatized (3.75 Gyr old Isua), there is no evidence of iron exchange between consecutive layers in BIF or diagenetic/metamorphic resetting of Fe isotopes. Similarly, REE+Y compositions of Archean BIF appear insensitive to the influence of post-depositional processes[23,24]. In this regard there is no reason to believe that Ni would have behaved differently. Furthermore, the influence of metamorphism on molar Ni/Fe ratios in BIF, if any, would be to lower the relative Ni content because Fe from pre-metamorphic BIF is easily incorporated into prograde metamorphic minerals such as magnetite, grunerite or Fe-rich pyroxene, while any Ni lost from the system would only have reduced the molar Ni/Fe ratio further. The end result of such post-depositional effects would be to dampen the structure of the Ni/Fe topology shown in Figure 1.

1. Klein, C. Some Precambrian banded iron formations (BIFs) from around the world: Their age, geologic setting, mineralogy, metamorphism, geochemistry, and origin. *Am. Mineral.* **90**, 1473-1499 (2005).
2. Klein, C. & Beukes, N.J. in *The Proterozoic Biosphere: A Multidisciplinary Study* (eds Schopf, J.W. & Klein, C.) 139–146 (Cambridge University Press, 1992).
3. Dimroth, E. & Chauvel, J.J. Petrography of the Sokoman Iron Formation in part of the central Labrador Trough, Quebec, Canada. *Geol. Soc. Am. Bull.* **84**, 111-134 (1973).
4. Perry, E.C., Tan, F.C. & Morey, G.B. Geology and stable isotope geochemistry of the Biwabik Iron Formation, northern Minnesota. *Econ. Geol.* **68**, 1110-1125 (1973).
5. Han, T.-M. Microstructures of magnetite as guides to its origin in some Precambrian iron-formations. *Fortschr. Mineral.* **56**, 105-142 (1978).

6. McConchie, D. in *Precambrian Iron-Formations* (eds Appel, P.W.U. & LaBerge, G.L.) 541-597 (Theophrastus, 1987).
7. Ahn, J. H. & Buseck, P. R., Hematite nanospheres of possible colloidal origin from a Precambrian banded iron formation. *Science* **250**, 111-113 (1990).
8. Morris, R.C. Genetic modelling for banded iron-formation of the Hamersley Group, Pilbara Craton, Western Australia. *Precamb. Res.* **60**, 243–286 (1993).
9. Trendall, A.F. The significance of iron-formation in the Precambrian stratigraphic record. *Int. Assoc. Sedimentol. Spec. Publ.* **33**, 33-66 (2002).
10. Konhauser, K., Newman, D.K. & Kappler, A. The potential significance of microbial Fe(III) reduction during deposition of Precambrian banded iron formations. *Geobiology* **3**, 167-177 (2005).
11. Ewers, W.E. & Morris, R.C. Studies of the Dales Gorge Member of the Brockman iron formation, Western Australia. *Econ. Geol.* **76**, 1929-1953 (1981).
12. Krapež, B., Barley, M.E. & Pickard, A.L. Hydrothermal and resedimented origins of the precursor sediments to banded iron formation: Sedimentological evidence from the Early Paleoproterozoic Brockman Supersequence of Western Australia. *Sedimentology* **50**, 979-1011 (2003).
13. Vargas, M., Kashefi, K., Blunt-Harris, E.L. & Lovley, D.R. Microbiological evidence for Fe(III) reduction on early Earth. *Nature* **395**, 65–67 (1998).
14. Johnson, C.M., Beard, B.L., Beukes, N.J., Klein, C. & O´Leary, J.M. Ancient geochemical cycling in the Earth as inferred from Fe isotope studies of banded iron formations from the Transvaal craton. *Contrib. Mineral. Petrol.* **144**, 523-547 (2003).
15. Yamaguchi, K.E., Johnson, C.M., Beard, B.L. & Ohmoto, H. Biogeochemical cycling of iron in the Archean Paleoproterozoic Earth: Constraints from iron isotope variations in sedimentary rocks from the Kaapvaal and Pilbara Cratons. *Chem. Geol.* **218**, 135-169 (2005).
16. Johnson, C.M., Roden, E.E., Welch, S.A. & Beard, B.L. Experimental constraints on Fe isotope fractionation during magnetite and Fe carbonate

formation coupled to dissimilatory hydrous ferric oxide reduction. *Geochim. Cosmochim. Acta* **69**, 963-993 (2005).

17. Gole, M.J. & Klein, C. Banded Iron Formations through much of Precambrian time. *J. Geol.* **89**, 169-183 (1981).
18. Walker, J. C. G. Suboxic diagenesis in banded iron formations. *Nature* **309**, 340-342 (1984).
19. Baur, M.E., Hayes, J.M., Studley, S.A. & Walter, M.R. Millimeter-scale variations of stable isotope abundances in carbonates from banded iron formations in the Hamersley Group of Western Australia. *Econ. Geol.*, **80**, 270-282 (1985).
20. Frost, C.D., von Blankenburg, F., Schoenberg, R., Frost, B.R. & Swapp, S.M. Preservation of Fe isotope heterogeneities during diagenesis and metamorphism of banded iron formation. *Contrib. Mineral. Petrol.* **153**, 211-235 (2007).
21. Whitehouse, M.J. & Fedo, C.M. Microscale heterogeneity of Fe isotopes in >3.71 Ga banded iron formation from Isua Greenstone Belt, southwestern Greenland. *Geology* **35**, 719-722 (2007).
22. Johnson, C.M., Beard, B.L, Klein, C., Beukes, N.J. & Roden, E.E. Iron isotopes constrain biologic and abiologic processes in banded iron formation genesis. *Geochim. Cosmochim. Acta* **72**, 151-169 (2008).
23. Bau, M. Effects on syn- and post-depositional processes on rare-earth element distributions in Precambrian iron formations. *Eur. J. Miner.* **5**, 257-267 (1993).
24. Bohlar, R., Kamber, B.S, Moorbath, S., Fedo, C.M. & Whitehouse, M.J. Characterisation of early Archean chemical sediments by trace element signatures. *Earth Planet. Sci. Lett.* **222**, 43-60 (2004).

C12450